Differential Rotation and the Geodynamo

by

Richard R. Ogden

A thesis submitted to
the Faculty of Science
at the University of Glasgow
for the degree of
Doctor of Philosophy.

©Richard Ogden, October 1998

ProQuest Number: 13834231

All rights reserved

INFORMATION TO ALL USERS
The quality of this reproduction is dependent upon the quality of the copy submitted.

In the unlikely event that the author did not send a complete manuscript
and there are missing pages, these will be noted. Also, if material had to be removed,
a note will indicate the deletion.

ProQuest 13834231

Published by ProQuest LLC (2019). Copyright of the Dissertation is held by the Author.

All rights reserved.
This work is protected against unauthorized copying under Title 17, United States Code
Microform Edition © ProQuest LLC.

ProQuest LLC.
789 East Eisenhower Parkway
P.O. Box 1346
Ann Arbor, MI 48106 – 1346

GLASGOW
UNIVERSITY
LIBRARY

Abstract

This thesis investigates the effect of differential rotation on convection in a rapidly rotating, electrically conducting fluid, motivated by the problem of the generation of the Earth's magnetic field. First we consider how an imposed differential rotation affects the thermal stability of the fluid in the presence of an imposed toroidal magnetic field. We choose a magnetic field profile that is stable. The familiar role of differential rotation is a stabilising one. We wish to examine the less well known destabilising effect that it can have. In a plane layer model (for which we are restricted to Roberts number $q = 0$ to allow separation of variables) with differential rotation, $\mathbf{U} = s\Omega(z)\mathbf{1}_\phi$, no choice of $\Omega(z)$ led to a destabilising effect. However, in a cylindrical geometry (for which our model permits all values of q) we found that differential rotations $\mathbf{U} = s\Omega(s)\mathbf{1}_\phi$ which include a substantial proportion of negative gradient ($d\Omega/ds < 0$) give a destabilising effect which is largest when the magnetic Reynolds number $R_m = \mathrm{O}(10)$; the critical Rayleigh number, Ra_c, is about 7% smaller at minimum than at $R_m = 0$ for $q = 10^6$. We also found that as q is reduced, the destabilising effect is diminished and at $q = 10^{-6}$, which may be more appropriate to the Earth's core, the effect causes a dip in the critical Rayleigh number of only about 0.001%. In the above results, the Elsasser number $\Lambda = 1$ but the effect of differential rotation is also dependent on Λ. Earlier work has shown a smooth transition from thermal to differential rotation driven instability at high Λ [$\Lambda = \mathrm{O}(100)$]. We find, at intermediate Λ [$\Lambda = \mathrm{O}(10)$], a dip in the Ra_c vs. R_m curve similar to the $\Lambda = 1$ case. However, it has $Ra_c < 0$ at its minimum and unlike the results for high Λ, larger values of R_m result in a restabilisation.

We move on to take a brief look at how the above effect may influence magnetic instability. Working in the cylindrical geometry we again find that certain differential rotations have a destabilising effect, this time with a minimum in the critical value of the Elsasser number, Λ_c, at $R_m = \mathrm{O}(100)$ about 30% of its value at $R_m = 0$. Further, the forms of $\Omega(s)$ which cause this stability dip are the same ones as in the thermal stability investigation.

The above forms a preliminary to pursuing some nonlinear calculations. In the magnetostrophic approximation, which we employ, the most important nonlinear effect is the geostrophic flow, $U_G(s)\mathbf{1}_\phi$ which is dependent on the magnetic field through a modified Taylor's condition. Proceeding in the cylindrical geometry we study the nonlinear influence of this dynamically determined differential rotation on convection. The expected effect is for the geostrophic flow to equilibrate a growing solution in what is known as an Ekman state. This breaks down at greater forcing of the system and a Taylor state is reached. We approach this problem from the standpoint of trying to find Ekman states for various parameters and conditions. This we do successfully. However, we discover that our numerical solution sometimes breaks down when Ra is increased beyond a certain point ($Ra = Ra_T$). Here, we find good evidence to indicate that we are approaching a Taylor state. We also discover that $\omega \to 0$ as $Ra \to Ra_T$. We find that the most important factor affecting the numerical breakdown is the orientation of gravity. No numerical breakdown occurs (i.e. we can reach very high values of Ra) with radially directed gravity. However, this is not the case for axially directed gravity. The range of Ra over which an Ekman state can be found is of O(1) or less. Interestingly, there is also a correspondence between the gravity direction and the shape of the geostrophic flow. Radial gravity seems to promote a form of Ω which wouldn't have a stability dip (see above) whereas

axial gravity favours a form which would.

Preface

This thesis has been submitted in accordance with the rules of the Faculty of Science at the University of Glasgow for the degree of Doctor of Philosophy.

For the financial support of the Engineering and Physical Sciences Research Council I am grateful.

Many thanks are due to Professor David Fearn, my supervisor, for his guidance, patience and insight.

Contents

List of Figures

List of Tables

Chapter 1

Introduction

The existence of Earth's magnetic field has been known to human beings for over two thousand years. At the surface we can measure the poloidal part of the field and find that it must originate from within the planet. The field is not a static feature. The Geomagnetic Secular Variation (GSV) is a well documented (over the last couple of centuries) small timescale change and there are the more striking North-South pole reversals which, in recent geological times, have happened every few hundred-thousand years. Additionally, the magnetic field has existed for billions of years but the magnetic diffusion timescale is of the order of tens of thousands of years. There must therefore be some mechanism which creates and sustains the magnetic field. It is now widely accepted that this mechanism is the geodynamo, a complicated interaction between electric currents and convectively driven fluid flow acting in the Earth's molten iron outer-core. In particular, the large scale ω-effect acts to generate toroidal magnetic field (the azimuthal field contained within the core) by stretching poloidal field in the rotation direction. At the same time, the α-effect creates toroidal from poloidal field and poloidal from toroidal field via small scale twisting motions. The theory of electrically conducting fluids in rotating reference frames has therefore been the focus of much attention in recent years. It forms the basis for constructing a full mathematical description of the geodynamo. See Soward (1991), Roberts (1994) and Fearn (1996) for general reviews of this subject.

Such a system is governed by the Navier-Stokes equation, the magnetic induc-

tion equation and a temperature equation along with conditions for incompressibility (a suitable approximation for molten iron) and solenoidal magnetic fields. It may be appropriate to include the effects of compositional convection (Fearn, 1989b) but as this is not sufficiently well understood, current geodynamo work typically includes only thermal convection.

Ideally we would solve the governing equations as a fully 3-dimensional problem in a sphere of fluid incorporating an inner core. However, this is an extremely computationally intensive problem and is therefore limited in the depth of parameter space coverage (Glatzmaier and Roberts, 1995a,b). To make progress, with more modest computational requirements, simpler sub-problems are studied. Kinematic dynamos are one class (where the flow is prescribed and the induction equation is solved for the magnetic field). The other major class is magnetoconvection where convectively driven flows in the presence of a prescribed field are investigated. Using simpler geometries such as a plane layer, duct, cylinder or cylindrical annulus can also make the problem less demanding.

The outer core does not rotate as a solid body. Recent work from Song and Richards (1996) provides seismological evidence that the inner core rotates relative to the mantle (or outer boundary of the fluid) which would certainly cause differential (i.e. a radially dependent) rotation. Differential rotation will be the primary concern of this thesis. We shall investigate two alternative ways of incorporating it into the magnetohydrodynamic model. The first results in a linear problem which forms a preliminary to the second nonlinear one.

We shall take the governing equations and examine the stability of some typical basic state which is representative of conditions within the Earth's outer core. This is described by $\mathbf{B}_0$, $\mathbf{U}_0$ and T_0 (respectively the magnetic, velocity and temperature fields) and is one of the accepted ways of providing insights into

dynamo behaviour and has therefore been the subject of a substantial amount of work (for example Roberts and Stewartson, 1974; Fearn, 1979). For thermal stability we are interested in finding the critical value, Ra_c, of the Rayleigh number, Ra, see Equations (2.8). For $Ra > Ra_c$ convection sets in. We wish to investigate the effect of a prescribed differential rotation $\Omega(s)$ where $\mathbf{U}_0 = s\Omega(s)\mathbf{1}_\phi$ ($\mathbf{1}_\phi$ is the unit vector in the ϕ direction). It is known, generally, to have a stabilising effect, i.e. increasing the value of Ra_c and inhibiting convection (Fearn & Proctor 1983a,b; Fearn 1989a), at high flow strengths. We shall expand upon this linear work further in Chapters 3 and 4 by investigating the effect of a prescribed differential rotation in more detail, focussing in particular on the less well known destabilising effect of $\Omega(s)$.

Taylor (1963) derived a very important result (Taylor's constraint) applicable to systems of rapidly rotating, electrically conducting fluids with negligible viscosity i.e. ideally suited to the parameter regime of planetary dynamos. In Chapter 5 we proceed to consider the nonlinear problem where $\Omega(s)$ is not prescribed but dynamically determined through a modified version of Taylor's constraint. The starting point for his result is to make the magnetostrophic approximation (see Chapter 2) in the momentum equation,

$$\mathbf{1}_z \times \mathbf{U} = -\nabla P + (\nabla \times \mathbf{B}) \times \mathbf{B} - qRaT\mathbf{g} \ , \tag{1.1}$$

where the nondimensional parameters q and Ra are defined in (2.8) and $\mathbf{g}$ is the gravitational acceleration. Then, in sphere of fluid, permeated by magnetic field $\mathbf{B}$, the ϕ-component of (1.1)

$$U_s = -\frac{\partial P}{\partial \phi} + ((\nabla \times \mathbf{B}) \times \mathbf{B})_\phi \ , \tag{1.2}$$

is integrated over the curved surface of a cylinder $C(s)$, known as a Taylor cylinder, coaxial with the sphere and intersecting it at $z = z_T$ and $z = z_B$ (see

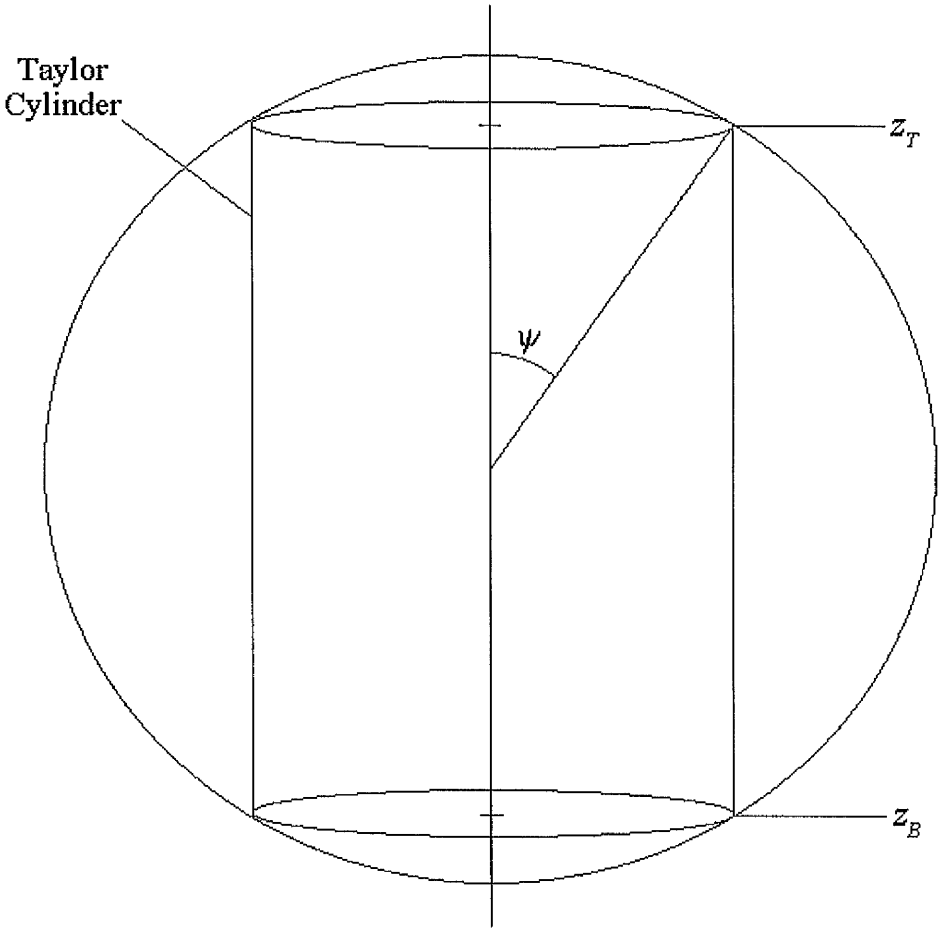

Figure 1 - Taylor Cylinder in a Spherical Geometry.

Figure 1), to give

$$\int_{C(s)} U_s dS = \int_{C(s)} \left((\nabla \times \mathbf{B}) \times \mathbf{B} \right)_\phi dS \, . \tag{1.3}$$

Fluid incompressibility tells us that there can be no net flow into the cylinder so the left hand side of (1.3) must be zero. Hence we obtain

$$\int_{z_B}^{z_T} \langle (\nabla \times \mathbf{B}) \times \mathbf{B} \rangle_\phi \, dz = 0 \, , \tag{1.4}$$

which is Taylor's constraint, where

$$\langle f \rangle = \overline{f} \equiv \frac{1}{2\pi} \int_0^{2\pi} f d\phi \, , \tag{1.5}$$

is the azimuthal average of f.

In the bulk of the fluid, neglecting viscosity is a suitable approximation but there are narrow boundary layers of thickness $O(E^{1/2})$ in which viscosity is important. The Ekman number, E [defined in (2.8)], is proportional to viscosity. Equation (1.2) is therefore only valid in the main body of the fluid, outwith the Ekman layer. The Taylor cylinder excludes the layer so the left hand side of (1.3) must be modified to take account of the boundary layer flow which feeds into the top and bottom of the cylinder. According to Batchelor (1967) a flow U along a viscous, planar boundary produces a flow (known as Ekman suction or Ekman pumping) of dimensional magnitude

$$(U/2)(\nu/\Omega_n)^{1/2} \tag{1.6}$$

which is perpendicular to the directions of U and Ω_n, where Ω_n is the component of angular velocity normal to the boundary. For the sphere (with dimensionless velocity field U) this means there is a flow of magnitude

$$2\pi s\left(\frac{2E}{\cos\psi}\right)^{1/2}\overline{U}_\phi|_{z_T}\ , \tag{1.7}$$

into the polar caps at the top and bottom of the Taylor cylinder. Then, because of incompressibility, these flows must be balanced by a net flow out of the cylinder sidewalls. We can then write

$$\int_{C(s)} U_s dS = 2\pi s\left(\frac{2E}{\cos\psi}\right)^{1/2}\overline{U}_\phi|_{z_T}\ . \tag{1.8}$$

Taking the curl of (1.1) gives

$$-\frac{\partial \mathbf{U}}{\partial z} = \nabla\times\left((\nabla\times\mathbf{B})\times\mathbf{B}\right) + qRa\nabla T\times\mathbf{g}\ . \tag{1.9}$$

Then taking the azimuthal average and integrating with respect to z, we find that the azimuthal component of the axisymmetric part of U is composed of three parts

$$\overline{U}_\phi = U_M + U_T + U_G \,, \tag{1.10}$$

where U_M is the magnetic wind

$$\int_z^{z_T} \left\langle \nabla \times \left((\nabla \times \mathbf{B}) \times \mathbf{B} \right) \right\rangle_\phi dz \tag{1.11}$$

and U_T is the thermal wind

$$qRa \int_z^{z_T} \langle \nabla T \times \mathbf{g} \rangle_\phi \, dz \tag{1.12}$$

The geostrophic velocity $U_G(s)$ is an undetermined function of integration. For the chosen definitions of U_M and U_T we have that

$$U_G = \overline{U}_\phi|_{z_T} \,. \tag{1.13}$$

which allows us to write [substituting (1.8) into (1.3)]

$$U_G(s) = \left(\frac{\cos\psi}{2E}\right)^{1/2} \int_{z_B}^{z_T} \langle (\nabla \times \mathbf{B}) \times \mathbf{B} \rangle_\phi \, dz. \tag{1.14}$$

which is the modified Taylor's condition. The two constraints (1.4) and (1.14) correspond to two different states of the system. If viscosity is important then (1.14) holds and the geostrophic flow is explicitly determined. It acts, over time, to equilibrate a solution in an Ekman state where $|U_G| = \mathrm{O}(1)$ and $|\mathbf{B}| = \mathrm{O}(E^{1/4})$. Associated with an Ekman state is the Taylor state in which viscosity is not important and (1.4) holds. The geostrophic flow is then determined implicitly through (1.4) and the magnetic induction equation (1.15). For $|\mathbf{B}| = \mathrm{O}(1)$, (1.4) can be satisfied by cancellation of large positive and negative

regions of $\langle(\nabla \times \mathbf{B}) \times \mathbf{B}\rangle_\phi$ (see for example Fearn and Proctor, 1987). It may be that an Ekman state evolves into a Taylor state with increased forcing of the system. This is the Malkus and Proctor (1975) scenario. It is the possible existence of Taylor states (and hence Ekman states as a route to finding them) that has interested numerous authors over the last couple of decades. There are two main classes of dynamo sub-problems where this type of investigation has been conducted: the kinematic dynamo problem and the rapidly rotating magnetoconvection problem. The former is less complicated (at least in formulation) so we shall review the findings in this area first.

The kinematic dynamo consists of solving only the magnetic induction equation (for more details on this equation see Chapter 2)

$$\frac{\partial \mathbf{B}}{\partial t} = \nabla \times (\mathbf{U} \times \mathbf{B}) + \nabla^2 \mathbf{B} \,. \tag{1.15}$$

This equation may be solved by prescribing $\mathbf{U}$ (see for example Bullard and Gellman, 1954; Hutcheson and Gubbins, 1994). An alternative approach is to consider only the mean, or axisymmetric part of (1.15), parameterising the effect of the non-axisymmetric part of the flow [required by Cowling's (1934) theorem] by an α-effect. We split $\mathbf{B}$ and $\mathbf{U}$ into axisymmetric (overbar) and non-axisymmetric (dashed) parts

$$\mathbf{B} = \overline{\mathbf{B}} + \mathbf{B}' \,, \mathbf{U} = \overline{\mathbf{U}} + \mathbf{U}' \,, \tag{1.16}$$

where $\langle \mathbf{B}' \rangle = \langle \mathbf{U}' \rangle = 0$, and the axisymmetric parts into azimuthal and meridional parts

$$\begin{aligned} \overline{\mathbf{B}} &= B\mathbf{1}_\phi + \mathbf{B}_M \,, \mathbf{B}_M = \nabla \times A\mathbf{1}_\phi \,, \\ \overline{\mathbf{U}} &= U\mathbf{1}_\phi + \mathbf{U}_M \,, \mathbf{U}_M = \nabla \times w\mathbf{1}_\phi \,, \end{aligned} \tag{1.17}$$

We take the ϕ-average of (1.15), giving the mean induction equation which has

an azimuthal part

$$\frac{\partial B}{\partial t} + s\mathbf{U}_M.\nabla(B/s) - (\nabla^2 - 1/s^2)B = s\mathbf{B}_M.\nabla(U/s) + (\nabla \times \overline{\mathbf{F}}_\epsilon)_\phi \,, \quad (1.18)$$

and a meridional part

$$\frac{\partial A}{\partial t} + \frac{1}{s}\mathbf{U}_M.\nabla(sA) - (\nabla^2 - 1/s^2)A = (\overline{\mathbf{F}}_\epsilon)_\phi \,. \quad (1.19)$$

The electromotive force $\mathbf{F}_\epsilon$ is defined by

$$\mathbf{F}_\epsilon = \mathbf{U}' \times \mathbf{B}' \,. \quad (1.20)$$

Braginsky's (1994) nearly axisymmetric approximation and Krause and Rädler's (1980) mean-field electrodynamics both lead to a simplification

$$\overline{\mathbf{F}}_\epsilon = \alpha\overline{\mathbf{B}} \,, \quad (1.21)$$

where α is determined by the non-axisymmetric velocity. In kinematic dynamos based on this approach, α is simply prescribed as is the differential rotation $\omega = U/s$. The ω-effect and α-effect are clearly seen in equations (1.18) and (1.19). The rightmost term of each equation describes the field-generating α-effect and the remaining term on the right hand side of equation (1.18) is the ω-effect, generating azimuthal field B from the meridional field $\mathbf{B}_M$. This kind of formulation is thus called an $\alpha^2\omega$-dynamo. Generally, the ω- or α-effect term in (1.18) is neglected to give an α^2- or $\alpha\omega$-dynamo (respectively) which have been intensively studied (for example Roberts, 1972). To solve these equations, U, $\mathbf{U}_M$ and α are prescribed in a sensible way in an attempt to create dynamo action. The "post-kinematic dynamo" extends this approach by adding some dynamics. Rather than prescribe the whole velocity field, U_G replaces, or is added to, U and is determined through equation (1.14).

In some cases the post-kinematic dynamo exhibits the expected connection between Ekman and Taylor states (for example Abdel-Aziz and Jones, 1988). However, it also has produced alternative pictures. Soward and Jones (1983) find subcritical Taylor states as well as unconnected Taylor and Ekman branches. In the spherical geometry an α^2-dynamo is more likely to exhibit a smooth transition to a Taylor state than an $\alpha\omega$-dynamo (see for example Hollerbach and Ierley, 1991; Barenghi, 1993). See Jones (1991) and Fearn (1994) for a review.

We shall now review Taylor state investigations in the rapidly rotating magnetoconvection problem where $Ra = Ra_T$ is the transition point between an Ekman state and a Taylor state.

Roberts & Stewartson (1974) examined a plane layer of fluid rotating about the z-axis, infinite in the x and y directions with perfect thermal/electrical conductors as boundaries at $z = \pm\pi/2$. The basic state magnetic field was aligned horizontally along the y-axis. Driving the system was a z-direction temperature gradient with gravity acting parallel to it (note that the rotation axis is also in this direction, so their model corresponds to the polar regions of the Earth's core). They found solutions consisting of single convection rolls when the Elsasser number [defined in (2.8)] $\Lambda < 3^{1/2}/2$ and the Roberts number $q < 2$. These solutions exactly satisfied (1.4). At higher Λ the solution consisted of paired convection rolls with amplitudes A_1 and A_2 which did not satisfy Taylor's constraint. In a later paper (Roberts and Stewartson, 1975) they focused on the case $\Lambda > 3^{1/2}/2$ and added the geostrophic flow (which they called the Taylor shear) to the problem. This involved incorporating a form of (1.14) appropriate to the plane layer geometry. They supposed that initially, one convection roll was weaker than the other with $A_2 \ll A_1$ so that roll 2 acts as a perturbation

to roll 1. Investigating thermal instability, at Ra just above Ra_c, they found behaviour dependent on Λ and m (the y-direction wavenumber). Two significant values of Λ appear:

$$\Lambda_0 = \frac{3^{1/2}(q^2+3)}{2q^2}, \quad \Lambda_1 = 2\frac{3^{1/2}}{3^{1/2}+2}. \tag{1.22}$$

For $\Lambda > \Lambda_0$ the solution is stable i.e. one roll decays with respect to the other which, on its own, satisfies (1.4). For $\Lambda_1 < \Lambda < \Lambda_0$ the same happens only when $m > 0$ (we take roll 1 to have $+m$ in its expansion and roll 2 to have $-m$). If $m < 0$ the solution is unstable and the second roll grows until $A_2 \ll A_1$ no longer holds. No further conclusions were made as the mathematical analysis used by Roberts & Stewartson breaks down at this point. In the case $3^{1/2}/2 < \Lambda < \Lambda_1$ both $m > 0$ and $m < 0$ result in an unstable solution with the second roll growing as before. We can therefore conclude that it is possible, for certain parameter ranges, to evolve to a pure Taylor state from a solution which does not satisfy (1.4).

The plane layer model is useful but inherently unrealistic due to its unbounded nature. The duct model improves on the situation by adding electrically insulating sidewall boundaries $x = \pm\Delta$ (non-dimensionalised). In the context of the Taylor problem this was first examined by Soward (1986). Instead of taking solutions which satisfied the linear problem at Ra_c and increasing Ra until reaching Ra_T (the Rayleigh number above which a Taylor state can be found) he adopted a different but equivalent method. For this problem he was able to derive an expression for the geostrophic flow of the following form

$$(CE^{1/2} + q|\mathbf{b}|^2)U_G = g(|\mathbf{b}|^2, \theta)\,, \tag{1.23}$$

where C is constant which we will not define and g is a function of the magnetic field and temperature perturbations. This meant that $E \to \infty$ was equivalent

to the linear problem and $E = 0$ was equivalent to $Ra = Ra_T$. The Ekman number, E, was progressively decreased from a finite value to zero at which point a Taylor state would exist. The key feature of this analysis was that, at $E = 0$, the expression for U_G was still valid. For his results he fixed $\Delta = 1.6$ and $\lambda = 3^{1/2}$ where $\lambda = \beta^2\Lambda$ and β is the wavenumber along the y-axis. Initially setting $q = 1$ and varying β between 0 and 1.6 he found the difference between Ra_T and Ra_c was minimal (less than 10% of Ra_c for most of the region). He discovered instances of $Ra_T > Ra_c$ and $Ra_T < Ra_c$. However, the main focus of his paper was to explore the range $q << 1$. At progressively smaller values of q the geostrophic flow gained a more and more complicated structure. Two distinct regions appeared, one with $|U| = \mathrm{O}(1)$ and the other with $|U| = \mathrm{O}(q^{-1})$ suggesting that we may encounter numerical problems upon investigating the small q limit.

The duct model was also investigated by Jones & Roberts (1990) but with gravity aligned perpendicular to the rotation vector (simulating the equatorial region). They initially looked at a model with no sidewalls and showed that single rolls could not satisfy (1.4) and proved that double roll solutions only satisfied (1.4) when $\Lambda < \Lambda_T$ (where $\Lambda_T \approx 4.080$ for electrically insulating top and bottom boundaries). Their general conclusion was that Taylor states would only exist when $\Lambda < \Lambda_T$ for the duct model. In their following numerical work the only Taylor states they found were, indeed, in this region.

A natural progression from the work described so far was to move to a more realistic curved geometry. Skinner and Soward (1988, 1990) extend Soward's duct model to a cylinder of fluid with gravity anti-parallel to the rotation vector which was aligned along the axis of the cylinder. Top and bottom boundaries at $z = 0, 1$ were isothermal and perfect electrical conductors while the cylindrical

sidewall boundary was isothermal and electrically insulating. They again found Ra_T close to Ra_c over a range of $0 < \Lambda < 10$ for both $m = 1$ and $m = 2$ azimuthal modes. As with the duct they focussed on small values of q and found numerical problems below approximately $q = 0.02$, again seeing distinct inner and outer regions of differing behaviour.

It is from this point that our study begins. We wish to investigate the cylindrical geometry more thoroughly by allowing the following variations: axially or radially directed gravity, an inner cylindrical boundary (core) and insulating or perfectly conducting sidewall boundaries. However, before tackling the non-linear problem where the azimuthal (geostrophic) flow is determined dynamically (Chapter 5) we shall first see how the system behaves with a prescribed azimuthal flow (Chapters 3 and 4). In the next chapter we introduce the magnetohydrodynamic equations necessary to model these situations. A discussion of the work presented in this thesis can be found in Chapter 6.

Chapter 2

The Magnetohydrodynamic Model

In this chapter we introduce the equations which govern an electrically conducting fluid in a rotating reference frame. Firstly we have the momentum equation (incompressible Navier-Stokes)

$$\frac{\partial \mathbf{U}^*}{\partial t^*} + (\mathbf{U}^*.\nabla)\mathbf{U}^* + 2\boldsymbol{\Omega}_0 \times \mathbf{U}^* = \\ -\frac{1}{\rho_0}\nabla P^* + \nu\nabla^2\mathbf{U}^* + \frac{1}{\rho_0}\mathbf{J}^* \times \mathbf{B}^* + \frac{\rho^*}{\rho_0}\mathbf{g}\,, \tag{2.1}$$

where $\mathbf{U}^*$ is fluid velocity, $\mathbf{B}^*$ is magnetic field, $\mathbf{J}^* = \mu^{-1}\nabla \times \mathbf{B}^*$ is the current density, ρ^* is density, P^* is pressure and t^* is time. The parameters ν, μ and ρ_0 (which are all taken to be constant) represent the kinematic viscosity, magnetic permeability and average density of the fluid. The angular frequency of the reference frame is $\boldsymbol{\Omega}_0 = \Omega_0\mathbf{1}_z$ and $\mathbf{g} = g_0 g(\mathbf{r})\mathbf{1}_g$ is the gravitational acceleration, where g_0 is the maximum value, $g(\mathbf{r})$ is a known function of position and has a maximum value of 1 and $\mathbf{1}_g$ is the unit vector in the direction of gravity. In this thesis we shall be using $g(\mathbf{r}) = -1$ in the plane layer geometry and both $g(\mathbf{r}) = -s$ and $g(\mathbf{r}) = -1$ in the cylindrical geometry where s is nondimensional radius. The first two terms of (2.1) make up the inertial part of the equation. Following that is the Coriolis acceleration, the pressure term (modified to include the centrifugal force which could have alternatively been incorporated in a modified $\mathbf{g}$), viscous diffusion, the Lorentz acceleration (through this term the magnetic field influences the fluid flow) and the buoyancy term. The Boussinesq

approximation has been applied to this equation; that is, the density is regarded as a constant except in the buoyancy term.

Secondly we have the magnetic induction equation

$$\frac{\partial \mathbf{B}^*}{\partial t^*} = \nabla \times (\mathbf{U}^* \times \mathbf{B}^*) + \eta \nabla^2 \mathbf{B}^* \,, \tag{2.2}$$

where η is the magnetic diffusivity of the fluid which is taken to be constant. The terms from left to right are the magnetic field time derivative, the induction term (where the fluid flow influences the magnetic field) and the magnetic diffusion term.

Thirdly we have the temperature equation

$$\frac{\partial T^*}{\partial t^*} + (\mathbf{U}^*.\nabla)T^* = \kappa \nabla^2 T^* + \epsilon \,, \tag{2.3}$$

where T^* is temperature and κ is the thermal diffusivity (taken to be constant) of the fluid. From left to right we have the temperature time derivative, advection of heat, diffusion of heat and a constant heat source. We require the following condition for fluid incompressibility

$$\nabla.\mathbf{U}^* = 0 \,. \tag{2.4}$$

We also have a condition for sourceless magnetic fields

$$\nabla.\mathbf{B}^* = 0 \,, \tag{2.5}$$

which is in fact not independent of (2.2) so doesn't contribute to the system of equations. It is, however, a useful relationship. To complete the system we use an equation of state which expresses the density as

$$\rho^* = \rho_0(1 - \gamma(T^* - T_0^*)) \,. \tag{2.6}$$

Putting (2.1) – (2.6) together we obtain a non-linear system in which dimensional versions of the variables have been starred to distinguish them from the dimensionless versions which we shall introduce below

$$\begin{aligned}
\frac{\partial \mathbf{U}^*}{\partial t^*} + (\mathbf{U}^*.\nabla)\mathbf{U}^* + 2\mathbf{\Omega}_0 \times \mathbf{U}^* = \\
-\frac{1}{\rho_0}\nabla P^* + \nu\nabla^2\mathbf{U}^* + \frac{1}{\mu\rho_0}(\nabla \times \mathbf{B}^*) \times \mathbf{B}^* - \gamma \mathbf{g} T^* \,, \\
\frac{\partial \mathbf{B}^*}{\partial t^*} = \nabla \times (\mathbf{U}^* \times \mathbf{B}^*) + \eta\nabla^2\mathbf{B}^* \,, \\
\frac{\partial T^*}{\partial t^*} + (\mathbf{U}^*.\nabla)T^* = \kappa\nabla^2 T^* \,, \\
\nabla.\mathbf{U}^* = 0 \,.
\end{aligned} \tag{2.7}$$

Note that the addditional terms from (2.6) have been absorbed into P^* and the heat source, ϵ, has been dropped. It is not necessary because our system will be driven by an applied temperature difference.

We may non-dimensionalise these equations. This introduces the parameters Λ, the Elsasser number, Ra, a modified Rayleigh number (the normal Rayleigh number used in non-magnetic calculations is Ra/E), E, the Ekman number, E_η, the magnetic Ekman number, R_m, the magnetic Reynolds number and q, the Roberts number, defined (respectively) by

$$\begin{aligned}
\Lambda = \frac{B_M^2}{2\Omega_0\rho_0\mu\eta} \,, \quad Ra = \frac{g_0\gamma\beta L^2}{2\Omega_0\kappa} \,, \\
E = \frac{\nu}{2\Omega_0 L^2} \,, \quad E_\eta = \frac{\eta}{2\Omega_0 L^2} \,, \\
R_m = \frac{U_M L}{\eta} \,, \quad q = \frac{\kappa}{\eta} \,.
\end{aligned} \tag{2.8}$$

where β is some measure of temperature gradient, L is our lengthscale (e.g. the outer radius in a cylindrical annulus of fluid), B_M is indicative of the maximum field strength and U_M of the maximum flow speed. Typical geophysical values for the Earth are $\Lambda = \mathrm{O}(1-100)$, $E = \mathrm{O}(10^{-15})$, $E_\eta = \mathrm{O}(10^{-10})$, $R_m > \mathrm{O}(1)$

and $q = \mathrm{O}(10^{-5})$. Here we will non-dimensionalise using the magnetic diffusion timescale $\tau_\eta = L^2/\eta$, $\mathrm{O}(10^5)$ years, making the following transformations

$$\mathbf{U}^* = (\eta/L)\mathbf{U}\,, \quad \mathbf{B}^* = B_M\mathbf{B}\,, \quad T^* = \beta LT\,, \quad t^* = (L^2/\eta)t\,. \tag{2.9}$$

Equations (2.7) then become

$$\begin{aligned} E_\eta\left[\frac{\partial \mathbf{U}}{\partial t} + (\mathbf{U}.\nabla)\mathbf{U}\right] + \mathbf{1}_z \times \mathbf{U} = \\ -\nabla P + E\nabla^2\mathbf{U} + \Lambda(\nabla\times\mathbf{B})\times\mathbf{B} - qRaTg(\mathbf{r})\mathbf{1}_g\,, \\ \frac{\partial \mathbf{B}}{\partial t} = \nabla\times(\mathbf{U}\times\mathbf{B}) + \nabla^2\mathbf{B}\,, \\ \frac{\partial T}{\partial t} + (\mathbf{U}.\nabla)T = q\nabla^2 T\,, \\ \nabla.\mathbf{U} = 0\,, \end{aligned} \tag{2.10}$$

Note that R_m does not appear; in Chapters 3 and 4, non-dimensionalisations are done with alternative scalings which result in this parameter appearing.

We shall employ the magnetostrophic approximation ($E = E_\eta = 0$) throughout this thesis. With the timescale we have chosen this means the inertial and viscous terms in the momentum equation are neglected which is consistent with the high rotation rate of the Earth and negligible viscosity of the core fluid. Applying the magnetostrophic approximation to (2.10) gives

$$\begin{aligned} \mathbf{1}_z \times \mathbf{U} = -\nabla P + \Lambda(\nabla\times\mathbf{B})\times\mathbf{B} - qRaTg(\mathbf{r})\mathbf{1}_g\,, \\ \frac{\partial \mathbf{B}}{\partial t} = \nabla\times(\mathbf{U}\times\mathbf{B}) + \nabla^2\mathbf{B}\,, \\ \frac{\partial T}{\partial t} + (\mathbf{U}.\nabla)T = q\nabla^2 T\,, \\ \nabla.\mathbf{U} = 0\,, \end{aligned} \tag{2.11}$$

Further, we shall be interested in the stability of a basic state $\mathbf{U}_0$, $\mathbf{B}_0$, T_0 and P_0, so $\mathbf{U}$, $\mathbf{B}$, T and P are written as

$$\mathbf{U} = \mathbf{U}_0 + \mathbf{u}\,, \quad \mathbf{B} = \mathbf{B}_0 + \mathbf{b} \quad \text{and} \quad T = T_0 + \theta\,, \quad P = P_0 + p\,, \tag{2.12}$$

where $\mathbf{u}$, $\mathbf{b}$, θ and p are perturbations to the basic state. The linearised, perturbation equations in the magnetostrophic limit are thus

$$\begin{aligned}
\mathbf{1}_z \times \mathbf{u} = &- \nabla p + \Lambda[(\nabla \times \mathbf{B}_0) \times \mathbf{b} + (\nabla \times \mathbf{b}) \times \mathbf{B}_0] - qRa\theta g(\mathbf{r})\mathbf{1}_g \ , \\
\frac{\partial \mathbf{b}}{\partial t} = &\nabla \times (\mathbf{u} \times \mathbf{B}_0) + \nabla \times (\mathbf{U}_0 \times \mathbf{b}) + \nabla^2 \mathbf{b} \ , \\
\frac{\partial \theta}{\partial t} + &(\mathbf{U}_0 . \nabla)\theta + (\mathbf{u} . \nabla) T_0 = q\nabla^2 \theta \ , \\
&\nabla . \mathbf{u} = 0 \ .
\end{aligned} \tag{2.13}$$

Any boundaries of the system will be considered to be rigid and perfect thermal conductors. This means that $\mathbf{u}.\hat{\mathbf{n}} = 0$ and $\theta = 0$ on the boundary. As an approximation, a boundary will either be a perfect conductor or a perfect insulator. Each of these gives two conditions based on the continuity of $\mathbf{b}$ at the boundary (see Sections 3.1, 3.3, 4.1 and 5.1 for more details). For the plane layer geometry this gives eight boundary conditions to match the eighth order system which the equations are reduced to (Section 3.1). However, in the cylindrical geometry we have to discard one of the boundary conditions since we end up with a sixth order system (Section 3.3). The method of choosing the boundary condition to be dropped is detailed in Fearn (1983a).

Chapter 3

The Effect of Imposed Differential Rotation on Thermal Stability

As we have already stated, differential rotation has a known stabilising effect on thermally driven convection. Fearn & Proctor (1983a) describe the occurence of this in a spherical geometry. They investigated the problem for Elsasser number $\Lambda = \mathrm{O}(1)$ i.e. when the Lorentz and Coriolis forces are approximately balanced. The critical Rayleigh number Ra_c, above which convection sets in, was found to be an increasing function of differential rotation strength, measured by R_m. In other words differential rotation has a stabilising effect. For $R_m \gg q$ they suggest that $Ra_c \propto R_m$. A further paper, Fearn and Proctor (1983b), explored the relationship between differential rotation strength (measured by $R_t = R_m/q$) and Ra_c in a plane layer geometry. This simpler geometry permitted a more detailed investigation of the phenomenon. They found that Ra_c was an increasing function of R_t; Ra_c was essentially constant between $R_t = 0$ and $R_t = \mathrm{O}(10)$ and at higher values of R_t there were two different relationships, depending on whether the differential rotation (a) had a turning point or (b) had no turning point. In case (a), $Ra_c \propto R_t^{3/4}$ and in case (b), $Ra_c \propto R_t$. Physically we can explain the stabilising effect by noting that shearing in the fluid causes motions in adjacent convective cells to be in opposition. Convection becomes concentrated on a scale where diffusion can counteract the effect of the shear. Hence convective motions are suppressed.

Another feature of differential rotation is that it may itself be a source of instability. Fearn (1989a) showed that this could occur when $R_m \geq \mathrm{O}(\Lambda)$. In a cylindrical geometry, a smooth evolution from buoyancy driven to differential rotation driven instability was observed when $q \geq \mathrm{O}(1)$. A similar smooth transition from thermal to magnetically driven instability has recently been demonstrated by Zhang (1995) for $q = 1$.

Acheson (1972, 1973), in a local stability analysis of the basic (non-dimensionalised) state

$$\mathbf{B}_0 = sF(s)\mathbf{1}_\phi \ , \quad \mathbf{U}_0 = s\Omega(s)\mathbf{1}_\phi \ , \quad T_0 = T_0(s) \ , \tag{3.1}$$

(respectively magnetic, velocity and temperature fields) in cylindrical polars (s, ϕ, z), found that the condition for instability is

$$\Delta \equiv \frac{s}{F^2}\frac{d}{ds}\left[F^2 - \frac{R_m}{\Lambda}\Omega\right] > m^2 \ , \tag{3.2}$$

where m is the azimuthal wavenumber and diffusion and buoyancy are absent. For the simple case of $F = 1$ (which eliminates the possibility of magnetically driven instabilities) this condition can only be satisfied if $d\Omega/ds < 0$. In a spherical geometry, with magnetic diffusion, Fearn and Weiglhofer (1992) found that instability is present for $R_m > \mathrm{O}(\Lambda)$ when $\Lambda \geq \mathrm{O}(100)$ but that as Λ is reduced, the critical value of R_m reaches a minimum then increases rapidly, with no instability found when $\Lambda < \mathrm{O}(50)$.

The results discussed above describe some of the roles of differential rotation. Recent work has shown that it may also have an important effect that had not been observed previously. Drew (1991) found that as differential rotation is increased it can have an initial destabilising influence around $R_m = \mathrm{O}(1)$, before the expected stabilising effect is apparent.

We wish to understand under what circumstances this stability dip occurs, how prominent it can be and what physical mechanism causes it. The full spherical problem is complicated and computationally intensive so with a view to gaining some insights we look at two simple models: (i) a plane layer and (ii) a cylindrical annulus, both consisting of a conducting fluid in a rotating reference frame. The system is differentially heated and has an azimuthal magnetic field, $\mathbf{B}_0$, imposed. The stability of this system is investigated when there is a shear in the basic azimuthal flow $\mathbf{U}_0$. Specifically, we look at the functional form of $\mathbf{U}_0$ with the aim of finding which features affect stability. The real flow in the Earth's core is unknown so we choose a small but diverse range of forms of $\mathbf{U}_0$.

The following sections describe how the magnetohydrodynamic equations are rendered in a form suitable for numerical computation and what results are obtained (this is done for both geometries). Some conclusions are also noted. The work of this chapter has been published in Ogden & Fearn (1995).

3.1 Plane Layer Equations & Solution

We use the model described in Fearn and Proctor (1983b) to obtain our plane layer results. The following is a summary of that model. We employ a non-dimensionalisation on the thermal diffusion time-scale $\tau_\kappa = L^2/\kappa$, O(10^{10}) years, with lengthscale L, the distance between top and bottom boundaries. Instead of (2.9) the magnetic, velocity and temperature fields are scaled as follows (the basic state and perturbation variables are scaled differently in this problem)

$$\begin{aligned} \mathbf{U}_0^* &= U_M \mathbf{U}_0 \,, \quad \mathbf{B}_0^* = B_M \mathbf{B}_0 \,, \quad T_0^* = \beta L T_0 \,, \\ \mathbf{u}^* &= (\kappa/L)\mathbf{u} \,, \quad \mathbf{b}^* = q B_M \mathbf{b} \,, \quad \theta^* = \beta L \theta \,, \end{aligned} \tag{3.3}$$

and in this case $\mathbf{g} = -g_0 \mathbf{1}_z$ where g_0 is a constant. Equations (2.13) are thus

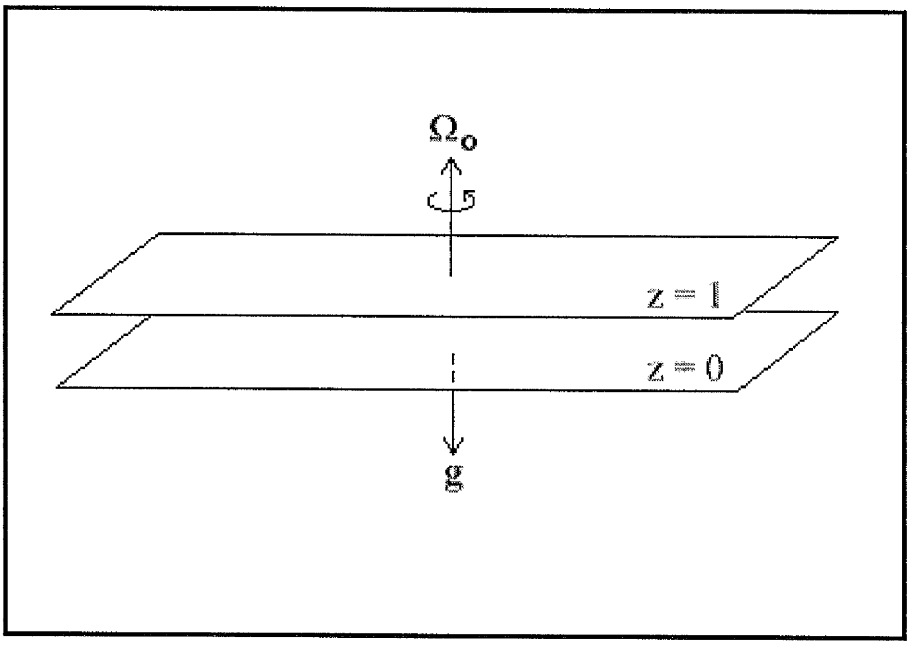

Figure 2 - Plane Layer Geometry.

replaced by

$$\begin{aligned} \mathbf{1}_z \times \mathbf{u} &= -\nabla p + \Lambda\Big((\nabla \times \mathbf{b}) \times \mathbf{B}_0 + (\nabla \times \mathbf{B}_0) \times \mathbf{b}\Big) + Ra\theta \mathbf{1}_z \ , \\ q\frac{\partial \mathbf{b}}{\partial t} &= qR_t \nabla \times (\mathbf{U}_0 \times \mathbf{b}) + \nabla \times (\mathbf{u} \times \mathbf{B}_0) + \nabla^2 \mathbf{b} \ , \\ \frac{\partial \theta}{\partial t} &+ R_t(\mathbf{U}_0.\nabla)\theta + (\mathbf{u}.\nabla)T_0 = \nabla^2 T \ , \\ \nabla.\mathbf{u} &= 0 \ , \end{aligned} \tag{3.4}$$

where we have defined $R_t = R_m/q$ and p has been scaled appropriately.

The fluid is confined to the region $0 < z < 1$ and the basic fields are of the form

$$\mathbf{B}_0(s) = s\mathbf{1}_\phi \ , \quad \mathbf{U}_0(s,z) = s\Omega(z)\mathbf{1}_\phi \ , \quad \nabla T_0(z) = -\mathbf{1}_z \ . \tag{3.5}$$

The presence of the term $qR_t \nabla \times (\mathbf{U}_0 \times \mathbf{b})$ in the magnetic induction equation means that the problem is not separable in s, so as a further simplification we set $q = 0$ ($q \to 0$, $R_m \to 0$ with R_t remaining finite) to remove it. This is

reasonable because the molecular value of the diffusivity ratio is $q \approx 10^{-5}$ in the Earth. Note that this also eliminates the time derivative from the induction equation. We employ a standard expansion of $\mathbf{u}$ and $\mathbf{b}$ into poloidal and toroidal parts. Thus

$$k^2\mathbf{u} = \nabla \times \omega \mathbf{1}_z + \nabla \times \nabla \times w\mathbf{1}_z \ , \quad k^2\mathbf{b} = \nabla \times j\mathbf{1}_z + \nabla \times \nabla \times b\mathbf{1}_z \ , \tag{3.6}$$

which automatically satisfy (2.4) and $\nabla.\mathbf{b} = 0$. All of p, ω, w, j, b and θ are expressed in the form

$$v(s, \phi, z, t) = v(z)J_m(ks)e^{i(m\phi - \omega t)} \ . \tag{3.7}$$

where J_m is the Bessel function of order m. Then system (3.4) reduces to

$$\begin{aligned} &(D^2 - k^2 + 2im\Lambda)Db + \Lambda m^2 j = 0 \ , \\ &(D^2 - k^2 + 2im\Lambda)Dj - \Lambda m^2(D^2 - k^2)b - imk^2 Ra\theta = 0 \ , \\ &(D^2 - k^2 - imR_t\Omega(z))\theta + \frac{i}{m}(D^2 - k^2)b + i\omega\theta = 0 \ , \end{aligned} \tag{3.8}$$

where $D \equiv d/dz$. The boundaries are taken to be rigid, perfect electrical and thermal conductors giving

$$w = \theta = b = Dj = 0 \quad \text{on} \quad z = 0, 1 \ , \tag{3.9}$$

as our boundary conditions. At this point the problem is solved numerically, using standard techniques for linear eigenvalue problems, see for example Fearn and Proctor (1983b).

3.2 Plane Layer Results

Motivated by the hope of finding, in this simple geometry, the destabilizing effect of differential rotation [found by Drew (1991) in the spherical geometry] we build

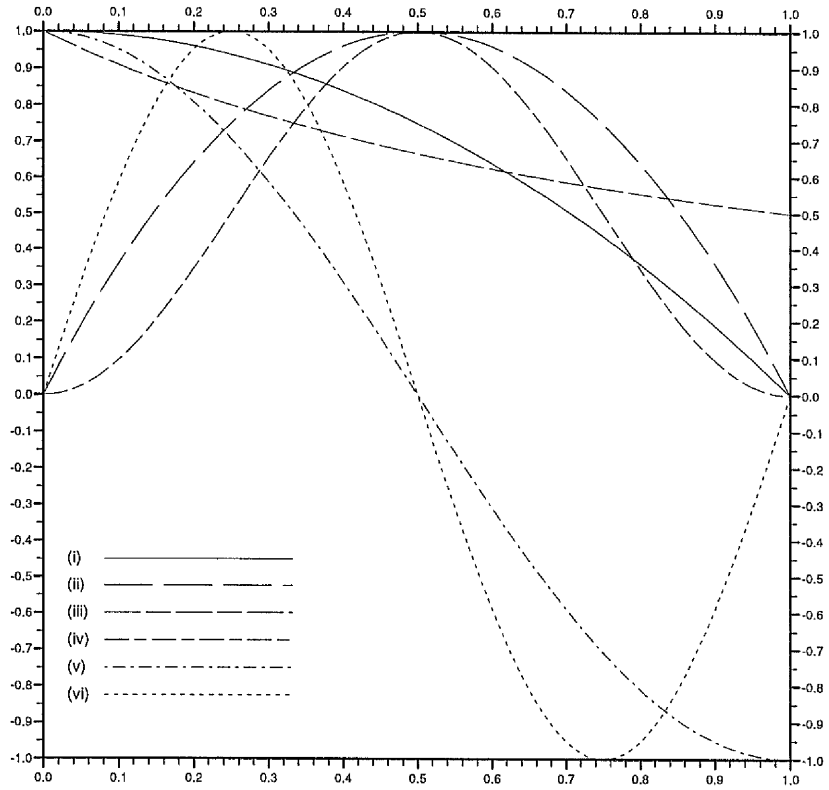

Figure 3 - Forms of $\Omega(z)$, see (3.10).

upon the work of Fearn and Proctor (1983b) by investigating further forms of $\Omega(z)$. We have chosen the following range of functions (shown graphically in Figure 3):

$$\begin{aligned}
&\text{(i)} \quad \Omega(z) = 1 - z^2, \\
&\text{(ii)} \quad \Omega(z) = 4z(1-z), \\
&\text{(iii)} \quad \Omega(z) = 1/(1+z), \\
&\text{(iv)} \quad \Omega(z) = \sin^2 \pi z, \\
&\text{(v)} \quad \Omega(z) = \cos \pi z, \\
&\text{(vi)} \quad \Omega(z) = \sin 2\pi z.
\end{aligned} \tag{3.10}$$

Figure 4 shows plots of Ra_c against R_t, on logarithmic scales, for each $\Omega(z)$. For this figure we have chosen parameter values of $m = 2$ (suggested by the

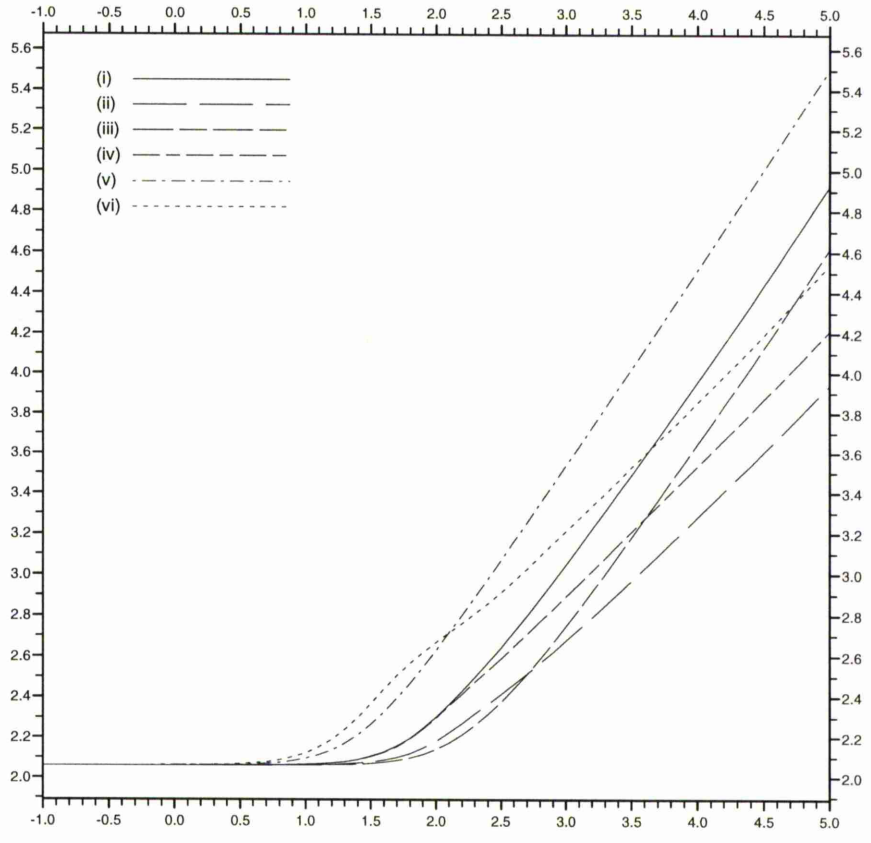

Figure 4 - Graphs of $\log_{10} Ra_c$ against $\log_{10} R_t$ for each form of $\Omega(z)$.

measurement of poloidal field at the Earth's crust) and $\Lambda = 1$, to be consistent with Fearn & Proctor (1983b), but other values give similar results. For large R_t we see an $Ra_c \propto R_t$ relationship for the graphs (i), (iii) and (v) and $Ra_c \propto R_t^{3/4}$ for (ii),(iv) and (vi). The flows with turning points are distinguished by having the smaller gradient in Figure 4. Figure 5 focuses on the region $0 < R_t < 10$ showing that in each case there is no destabilisation. We note two points which may account for the absence of the stability dip:

(a) It could be that $q = 0$ is too harsh a restriction on the problem.

(b) The differential rotation is not radially dependent as it is in the cylindrical

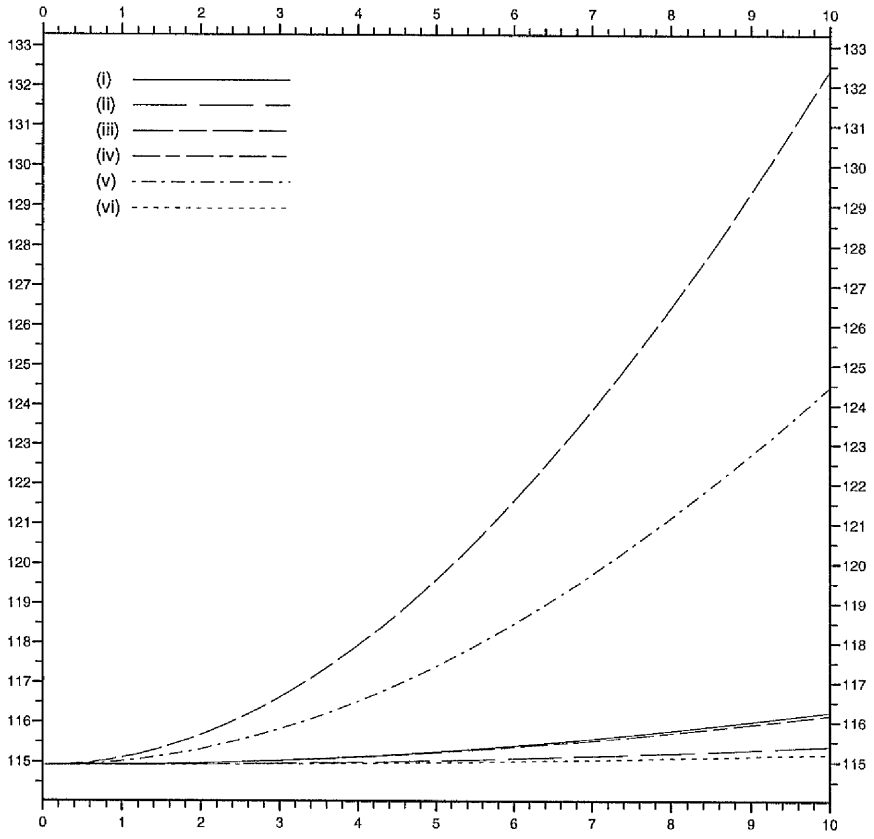

Figure 5 - Graphs of Ra_c against R_t for each form of $\Omega(z)$.

and spherical models.

To investigate the problem further we proceed to the next simplest problem, and one that allows more flexibility; the cylindrical annulus.

3.3 Cylindrical Annulus Equations & Solution

In the cylindrical geometry (Figure 6) we use the model described in Fearn (1983b), an infinite cylindrical annulus, inner radius s_i and outer radius $s_o = L$. For all of our calculations in this chapter we choose $s_{ib} = s_i/s_o = 0.35$ which is appropriate to the Earth's geometry. In this case we non-dimensionalise on the

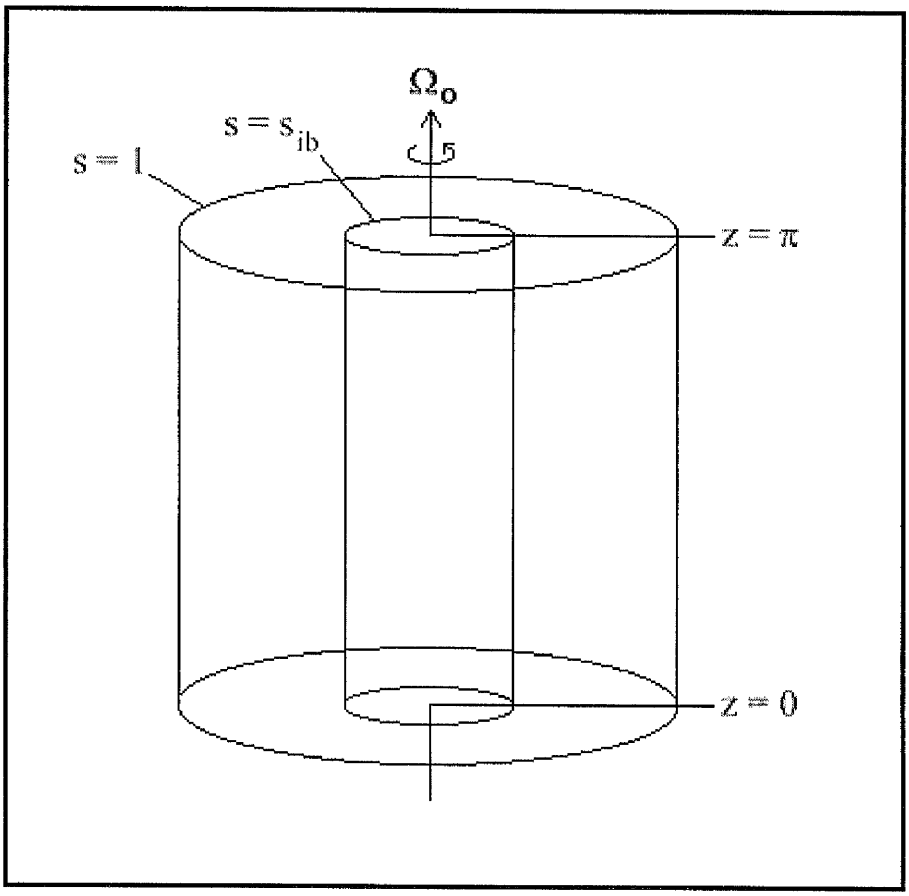

Figure 6 - Cylindrical Geometry.

slow timescale (a non-diffusive timescale which is slow in comparison with the inertial timescale) $\tau_s = q\Lambda^{-1}\tau_\kappa$, O($10^4$) years, as follows

$$\begin{aligned} &\mathbf{U}_0^* = U_M \mathbf{U}_0 \,, \quad \mathbf{B}_0^* = B_M \mathbf{B}_0 \,, \quad T_0^* = \beta L T_0 \,, \\ &\mathbf{u}^* = (L/\tau_s)\mathbf{u} \,, \quad \mathbf{b}^* = B_M \mathbf{b} \,, \quad \theta^* = \beta L \theta \,, \end{aligned} \tag{3.11}$$

and with gravity directed radially outward ($\mathbf{g} = g_0 s \mathbf{1}_s$). Gravity directed inward would be more natural but in experiments the outward centrifugal force simulates gravity. The two situations are equivalent as far as our calculations

are concerned. Equations $(2.13_{1,2,3})$ become

$$\begin{aligned}
\mathbf{1}_z \times \mathbf{u} = &- \nabla p + (\nabla \times \mathbf{B}_0) \times \mathbf{b} + (\nabla \times \mathbf{b}) \times \mathbf{B}_0 - qRa\Lambda^{-1} s\theta \mathbf{1}_s \ , \\
\frac{\partial \mathbf{b}}{\partial t} = &\nabla \times (\mathbf{u} \times \mathbf{B}_0) + R_m \Lambda^{-1} \nabla \times (\mathbf{U}_0 \times \mathbf{b}) + \Lambda^{-1} \nabla^2 \mathbf{b} \ , \\
\frac{\partial \theta}{\partial t} + &R_m \Lambda^{-1} (\mathbf{U}_0 . \nabla)\theta + (\mathbf{u} . \nabla) T_0 = q\Lambda^{-1} \nabla^2 \theta \ .
\end{aligned} \tag{3.12}$$

We use basic fields of the form

$$\mathbf{B}_0(s) = s\mathbf{1}_\phi \ , \quad \mathbf{U}_0(s) = s\Omega(s)\mathbf{1}_\phi \ , \quad \nabla T_0(s) = s^{-1}\mathbf{1}_s \ . \tag{3.13}$$

for which we shall investigate the effect on thermal instability of a variety of forms of $\Omega(s)$. The problem is separable in ϕ, z and t and we expand each of p, θ and the components u_s, u_ϕ, u_z, b_s, b_ϕ, b_z of $\mathbf{u}$ and $\mathbf{b}$ in the form

$$v(s, \phi, z, t) = v(s) e^{i(m\phi + nz - \omega t)} \ . \tag{3.14}$$

Applying boundary conditions (from Fearn 1983a)

$$\theta = 0 \ , \quad b_s = 0 \ , \quad im\Lambda u_s = (in \pm m/s) D b_s \ , \tag{3.15}$$

which describe perfectly conducting inner/outer boundaries, where the $+/-$ corresponds to the inner/outer boundary and $D \equiv d/ds$, the system can be reduced to

$$\begin{aligned}
&[imR_m\Lambda^{-1}\Omega - \Lambda^{-1}(D^2 + 3s^{-1}D + s^{-2} - m^2 s^{-2} - n^2) + im(sD - 1)]b_s \\
&\qquad - s^{-1}[2i\Lambda^{-1}n + mn^{-1}(m^2 + n^2 s^2)]b_z = i\omega b_s \ , \\
&[imR_m\Lambda^{-1}\Omega - \Lambda^{-1}(D^2 + s^{-1}D - m^2 s^{-2} - n^2) - im(sD + 4)]b_z \\
&\qquad - (m/ns)[s^2 D^2 + 3sD + 1 - m^2]b_s + im^2 n^{-1} qRa\Lambda^{-1}\theta = i\omega b_z \ , \\
&[imR_m\Lambda^{-1}\Omega - q\Lambda^{-1}(D^2 + s^{-1}D - m^2 s^{-2} - n^2)]\theta \\
&\qquad + s^{-1}[1 - sD]b_s - [in^{-1}s^{-2}(m^2 + n^2 s^2)]b_z = i\omega\theta \ ,
\end{aligned} \tag{3.16}$$

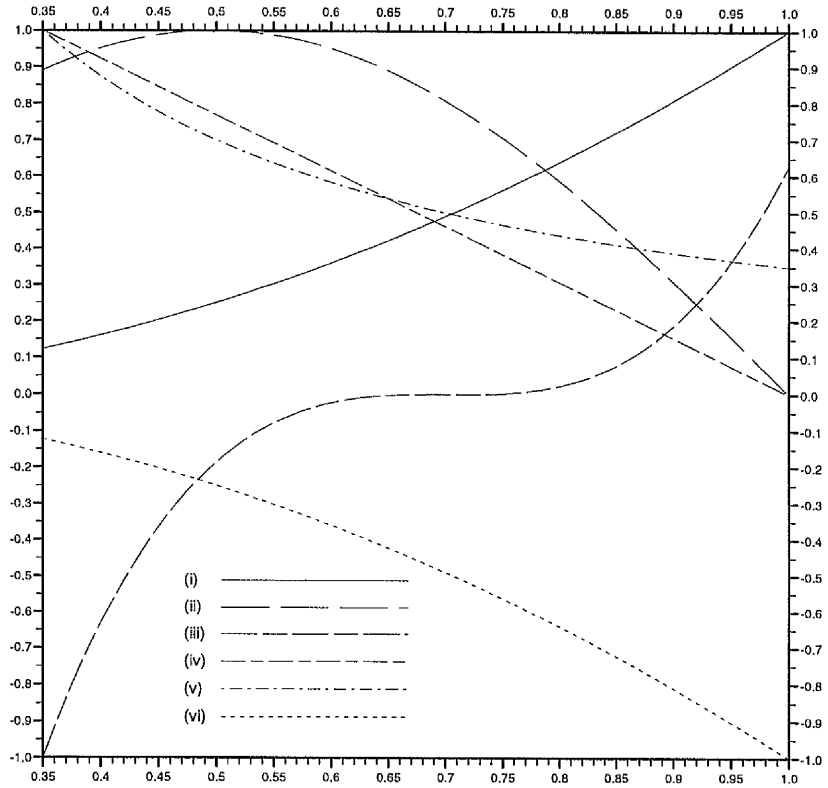

Figure 7 - Forms of $\Omega(s)$, see (3.17).

which is solved numerically as an eigenvalue problem for the frequency ω (see for example Fearn 1983b).

3.4 Cylindrical Annulus Results

3.4.1 Effect of Different Forms of Differential Rotation.

Initially we approach the cylinder in a similar way to the plane layer problem. We choose a selection of functions to represent $\Omega(s)$. These are as follows (also

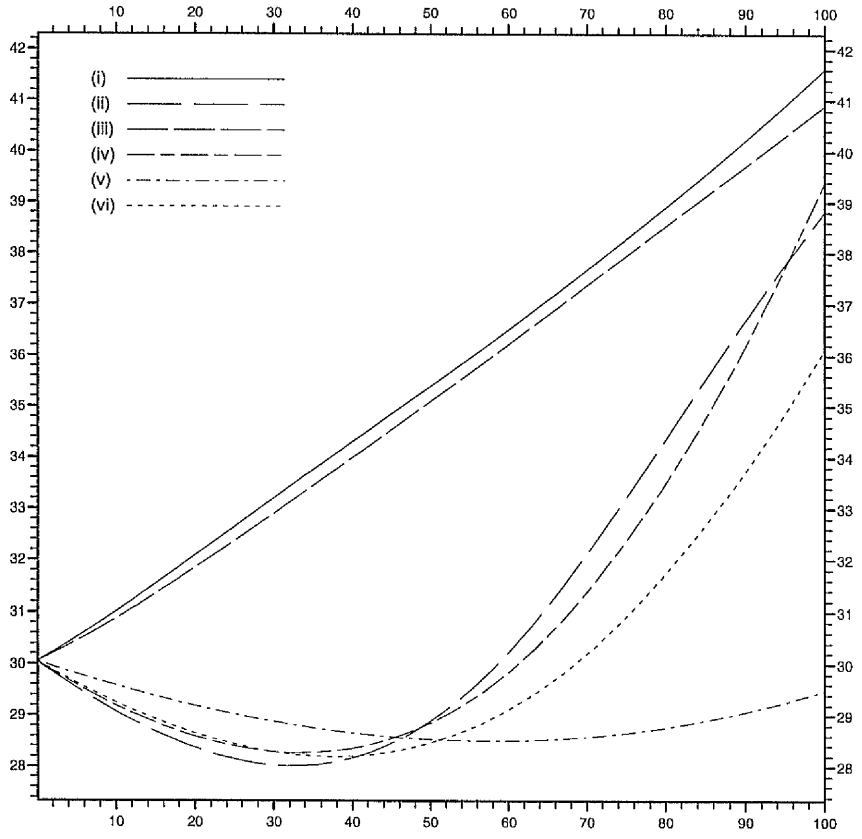

Figure 8 - Graphs of Ra_c against R_m for each form of $\Omega(s)$ with $q = 10^6$, $m = 2$ and $\Lambda = 1$.

shown graphically in Figure 7):

$$\begin{aligned}
&\text{(i)} \quad \Omega(s) = s^2, \\
&\text{(ii)} \quad \Omega(s) = \sin \pi s, \\
&\text{(iii)} \quad \Omega(s) = (s/s_{ib} \ - \ 2)^3, \\
&\text{(iv)} \quad \Omega(s) = (1-s)/(1-s_{ib}), \\
&\text{(v)} \quad \Omega(s) = s_{ib}/s, \\
&\text{(vi)} \quad \Omega(s) = -s^2.
\end{aligned} \tag{3.17}$$

We are interested in the effect of differential rotation on thermal instabilities. This will depend on the field strength as measured by the Elsasser number Λ,

the azimuthal wavenumber m, the axial wavenumber n and the Roberts number q as well as Ω. It is clearly not possible to comprehensively cover this parameter space. In this subsection, to explore the effect of varying Ω, we shall fix all of the above parameters and investigate their individual effects later. Over most of the geophysically interesting range of Λ ($1 < \Lambda < 100$) $m = 2$ is the most unstable thermal mode so we will choose this value. To ensure that we are far enough away from the instability driven purely by differential rotation (Fearn, 1989a; Fearn and Weiglhofer, 1992) we choose $\Lambda = 1$. For the boundary conditions chosen $Ra_c \to 0$ as $n \to 0$. Clearly this is not interesting for geophysical applications so we arbitrarily pick $n = 1$. We focus on $q = 10^6$ since we have found the destabilising effect of Ω to be a maximum when q is large. Finally we take the inner core radius $s_{ib} = 0.35$ (n and s_{ib} are unchanged throughout Chapter 3).

Figure 8 shows graphs of Ra_c against R_m for each form of $\Omega(s)$ and we can readily see that forms (ii), (iv), (v) and (vi) produce a dip; as the rotation strength is increased there is an initial destabilizing action before the well known stabilizing effect takes hold. In all the cases, the minimum value of Ra_c is about 6% less than its value at $R_m = 0$ with $\Omega(s) = \sin \pi s$ giving the largest dip.

We note that the forms of $\Omega(s)$ that give a dip are those that have a negative gradient for at least part of the interval. This is immediately apparent when we see that $\Omega(s) = -s^2$ gives a dip, but $\Omega(s) = s^2$ does not. This is indicative of the fact that the reference frame rotation enforces a preferred direction on the system. Here we can bear in mind the local analysis by Acheson (1983) where $d\Omega/ds < 0$ is the required condition for the generation of instability driven purely by the shear. Note that our results here are for $\Lambda = 1$, significantly below the minimum Elsasser number that Fearn and Weiglhofer (1992) found was required for instability driven purely by differential rotation. The effect of

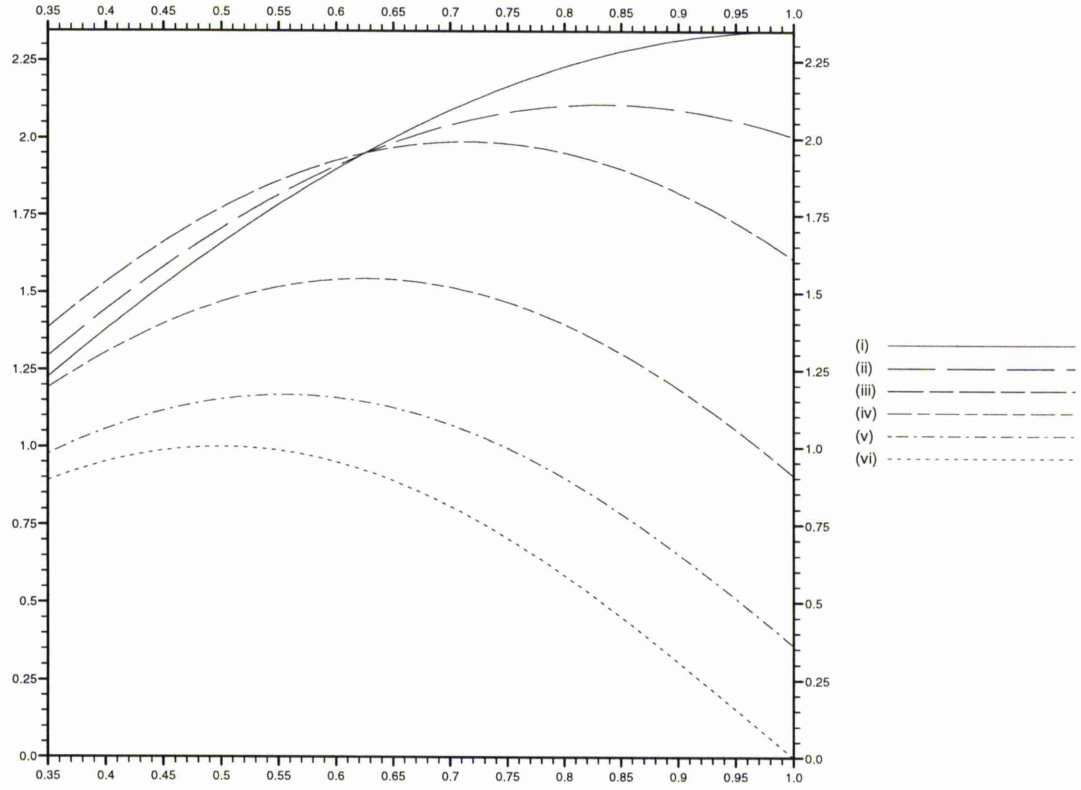

Figure 9 - Graphs of normalised $\Omega(s) = \sin B\pi s$. B takes values (i)0.5, (ii)0.6, (iii)0.7, (iv)0.8, (v)0.9 and (vi)1.0.

Λ is investigated in more detail in Section 3.4.3.

To examine the dependence on gradient further we chose to look at a differential rotation $\Omega(s) = A^{-1} \sin B\pi s$. When B takes the values 0.5, 0.6, 0.7, $A = B \cos B\pi s_{ib}$ and when B takes the values 0.8, 0.9, 1.0, $A = -B \cos B\pi$, (A is chosen to normalise the function such that the modulus of the maximum gradient of each function is the same). These are shown in Figure 9. The corresponding stability graphs are given in Figure 10. We see that cases (i)-(iii) give no dip but cases (iv)-(vi) do, and they have a greater proportion of negative than positive gradient. We can actually find a rough critical value of about $B_c = 0.72$ where $\Omega(s)$ with $B > B_c$ gives a dip but $B < B_c$ does not. This

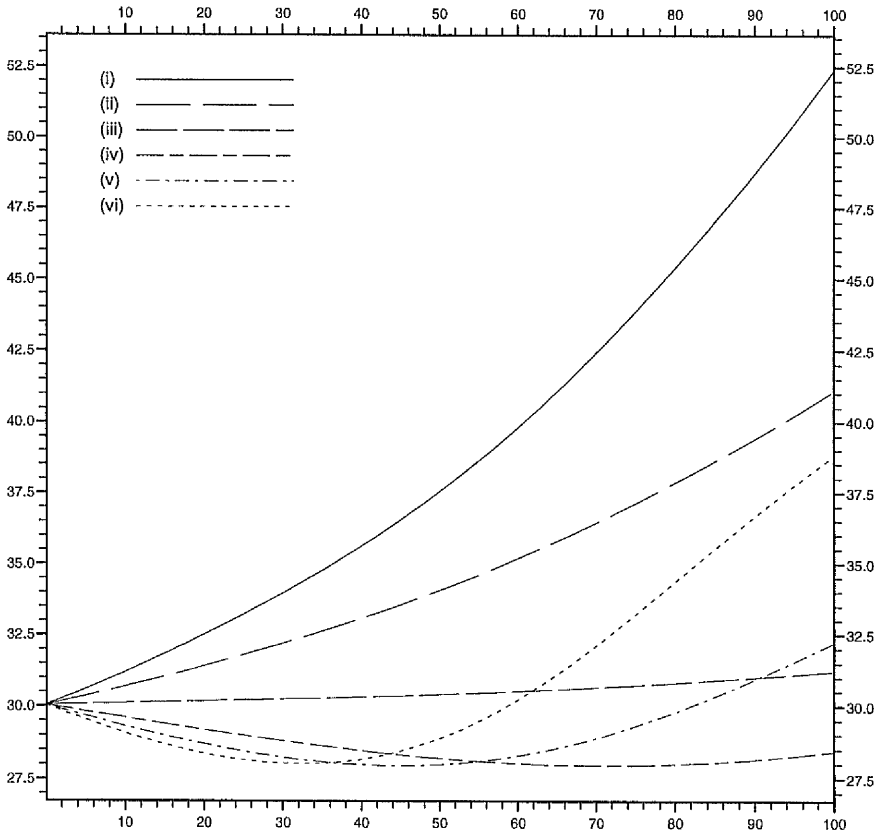

Figure 10 - Graphs of Ra_c against R_m for each form of $\Omega(s)$ given in Figure 9 with $q = 10^6$, $m = 2$ and $\Lambda = 1$.

critical value occurs almost, but not exactly, at the point where the ratio of positive to negative gradient is 1:1.

3.4.2 Effect of the Roberts Number.

We will now look at differential rotation form (ii) in (3.17), since it gives the largest dip, for different values of q. This may help to determine if $q = 0$ is a significant factor in the plane layer results. Figure 11 shows that for smaller q, the destabilising effect is diminished - compare these graphs with graph (ii) in Figure 8. For $q = 10^6$, Ra_c is about 7% smaller at minimum than at $R_m = 0$

whereas for $q = 1$, Ra_c is about 2% smaller. The case $q = 10^{-6}$ does actually have a dip even though it cannot be seen on the graph. However, Ra_c is only approximately 0.001% smaller at the minimum than at $R_m = 0$. Table 1 shows how Ra_c at $R_m = 0$, Ra_c^{min} (minimum value of Ra_c) and R_m^{min} (R_m at $Ra = Ra_c$) vary with q. As q decreases we see that R_m^{min}/q (which is equivalent to R_t in the plane layer model) tends to a finite value of around 0.5. Note that $Ra_c \approx Ra_c^{min}$ over a small range of values of R_m so the exact value of R_m^{min} is not easily determined. Hence the values for R_m^{min} in the table are approximate, though they do still serve to indicate the general trend. Table 1 also illustrates the diminishing size of the dip as q is decreased though, significantly, it does not approach zero as $q \to 0$. This indicates that in the limit $q \to 0$ there will still be a dip. We also investigated the variation of q at $\Lambda = 10$ (see Section 3.4.3).

q	$Ra_c(R_m = 0)$	Ra_c^{min}	R_m^{min}	R_m^{min}/q
10^{-1}	29.4916	29.4693	0.4	4
10^{-2}	29.4613	29.4603	9×10^{-3}	0.9
10^{-3}	29.4581	29.4577	5×10^{-4}	0.5
10^{-4}	29.4578	29.4574	5×10^{-5}	0.5
10^{-5}	29.4577	29.4574	5×10^{-6}	0.5
10^{-6}	29.4577	29.4574	5×10^{-7}	0.5

Table 1 - Variation of key values of Ra_c and R_m with q for $m = 2$ and $\Lambda = 1$.

3.4.3 Effect of the Elsasser Number.

The above results are all for $\Lambda = 1$, and show, whether a small dip in the Ra_c versus R_m curve is observed or not, a strong stabilising effect of the differential rotation for large R_m. We stated at the beginning of this chapter that earlier work has shown instability driven by differential rotation (with $Ra = 0$) when $\Lambda \geq O(50)$. This suggests that intermediate values of Λ may yield interesting results. Indeed they do. For example, Figure 12 shows the behaviour of Ra_c

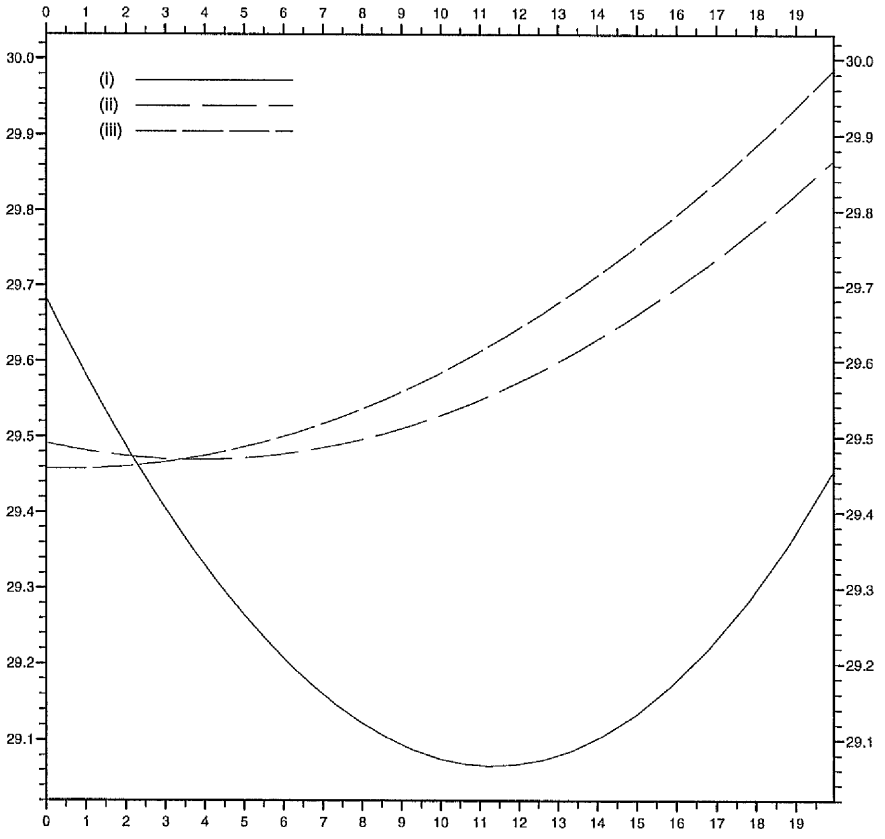

Figure 11 - Graphs of Ra_c against R_m/q for $\Omega = \sin \pi s$ with $m = 2$, $\Lambda = 1$ and (i)$q = 1$ (ii)$q = 10^{-1}$ and (iii)$q = 10^{-6}$.

versus R_m for $\Lambda = 10$. As R_m is increased, a small reduction in Ra_c is observed, as for $\Lambda = 1$. Ra_c then begins to increase, but then there is a much larger dip in the curve, followed by another, smaller one before finally, the stabilising role of differential rotation is established. Of particular note is the extent of the large dip, with Ra_c taking negative values; for a small range of R_m, the instability is driven purely by differential rotation.

We have also investigated the effect of varying q at $\Lambda = 10$ since $q \leq \mathrm{O}(1)$ is geophysically more realistic. For $q > 10$ we find the behaviour of the R_m/Ra_c graph to be almost identical to that of the $q = 10^6$ case (Figure 12). In Figure

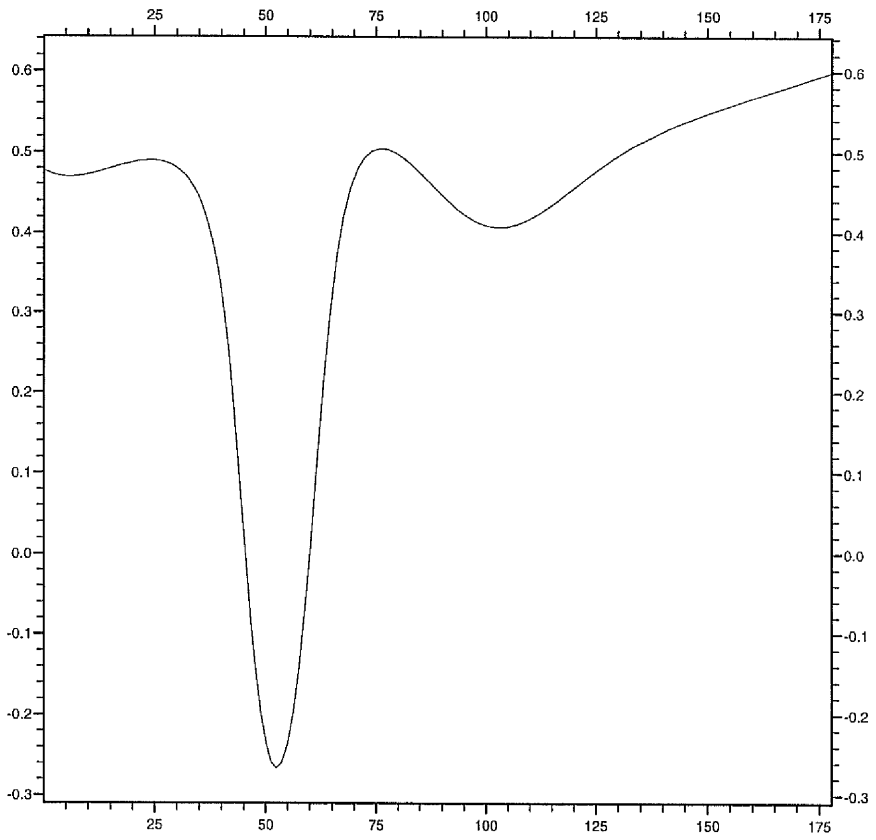

Figure 12 - Graphs of Ra_c against R_m for $\Omega = \sin \pi s$ with $m = 2$, $\Lambda = 10$ and $q = 10^6$.

13 we have plotted graphs for $q = 10$ and $q = 1$. At $q = 10$ the structure seen in Figure 12 is essentially still there but the initial dip is suppressed. At $q = 1$ the initial dip is completely gone. The next two dips are much more pronounced. For both cases the larger dip has $Ra_c < 0$.

3.4.4 Effect of the Azimuthal Wavenumber.

So far we have presented results for $m = 2$. As we have said, $m = 2$ is not necessarily the most unstable mode at $\Lambda = 1$ so we will now look at other values of m. Increasing (decreasing) the value of the azimuthal wavenumber has the

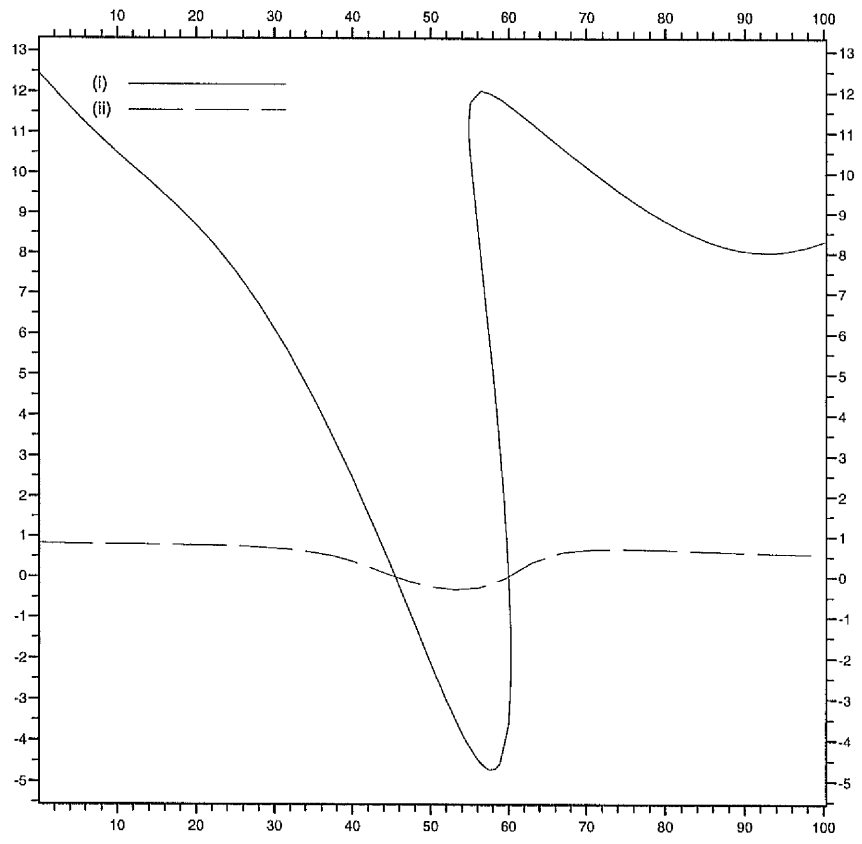

Figure 13 - Graphs of Ra_c against R_m for $\Omega = \sin \pi s$ with $m = 2$, $\Lambda = 10$ and (i) $q = 1$ and (ii) $q = 10$.

effect of increasing (decreasing) the value of R_m at which the dip occurs. Also, above $m = 3$, a secondary dip appears. Table 2 shows results for $m = 1$ to $m = 5$ and as a graphic example, Figure 14 shows a plot of Ra_c against R_m for the $m = 5$ case.

m	1	2	3	4	5
$Ra_c(R_m = 0)$	67.58	30.05	18.01	11.71	9.01
Ra_c^{min}	66.77	28.01	17.94, 17.12	11.66, 12.58	8.92, 10.68
R_m^{min}	5.96	31.62	9.44, 89.13	8.91, 133.35	13.34, 177.83

Table 2 - Variation of key values of Ra_c and R_m with m for $q = 1$ and $\Lambda = 1$.

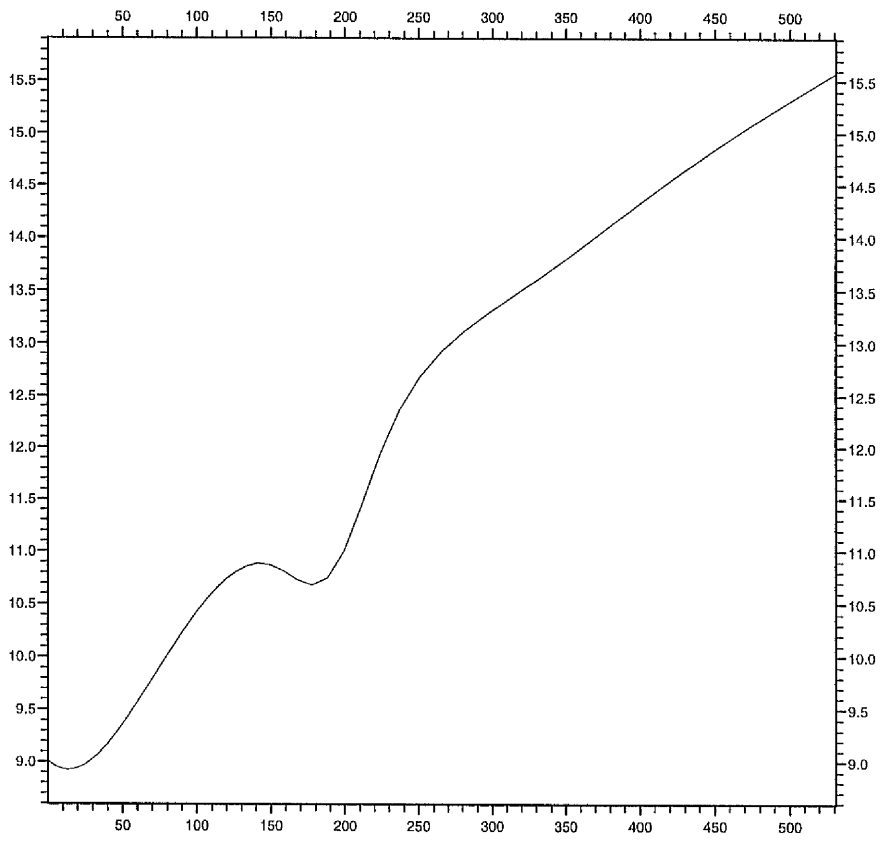

Figure 14 - Graph of Ra_c against R_m for $\Omega = \sin \pi s$ with $m = 5$, $\Lambda = 1$ and $q = 10^6$.

3.4.5 Effect on Frequency.

We are not primarily concerned with the effect of differential rotation on instability frequency but we find that, in all cases examined, it is generally non-zero (an overstable mode) and ω_c (the frequency at onset of instability) is proportional to R_m for large R_m. This is consistent with previous work (Fearn and Proctor, 1983b and Fearn, 1989a). In Figure 15 we give an example of our results. We have plotted the variation of ω_c with R_m for our six chosen forms of differential rotation. It is evident that in all cases the differential rotation only affects the constant of proportionality.

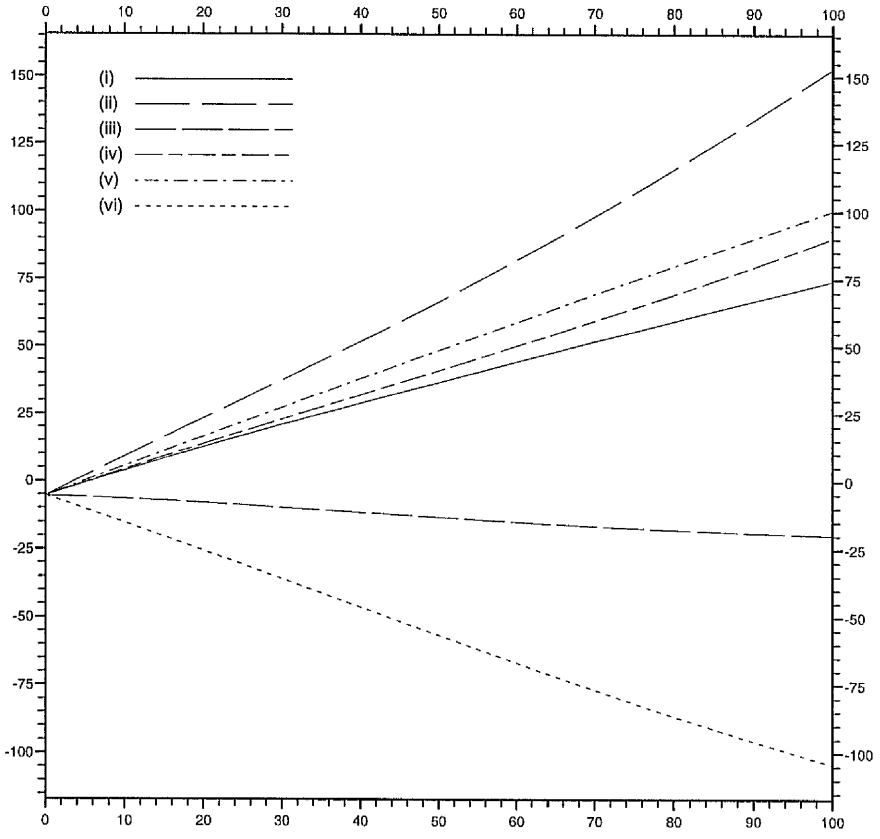

Figure 15 - Graphs of ω_c against R_m for each form of $\Omega(s)$.
with $q = 10^6$, $\Lambda = 1$, $m = 2$ and $n = 1$.

3.5 Conclusions.

We have investigated the effect of differential rotation $\mathbf{U} = s\Omega\mathbf{1}_\phi$, focusing on thermal instabilities, in a rapidly rotating system with an imposed magnetic field. We have studied two models: a plane layer with $\Omega = \Omega(z)$ and a cylindrical annulus with $\Omega = \Omega(s)$. In the plane layer we looked at the effect of different choices of Ω and found results consistent with Fearn and Proctor (1983b). In the cylindrical geometry we have additionally investigated the effect of varying q and Λ. In all cases we have focused on the shape of the Ra_c/R_m graph.

In the cylindrical geometry we found a dip in the Ra_c/R_m curve at $R_m = O(10)$ showing that differential rotation can have a destabilising effect. This occurs when $d\Omega/ds < 0$ for most of the interval $[s_{ib}, 1]$. We can quantify this by defining

$$G_\Omega = \Omega(1) - \Omega(s_{ib}) \,, \tag{3.18}$$

so that flows with $G_\Omega < 0$ have a destabilising effect and those with $G_\Omega > 0$ do not. This should probably be regarded as an approximate rule but it is valid for the flows we have looked at. The destabilising effect also seems to be associated with flows that are themselves unstable at larger Λ. At intermediate values of Λ [$\Lambda = O(10)$] islands of instability driven purely by differential rotation were found, with differential rotation resuming its traditional stabilising role at high R_m.

The value of q has a significant effect. For $q = 10^6$, Ra_c is about 7% smaller at the minimum than at $R_m = 0$. At $q = 1$ the size of the dip is still significant but as $q \to 0$ it approaches a finite but small limit. This suggests that in the plane layer we observed no dip because of the lack of s-dependence of Ω and not because $q = 0$. The fact that R_m/q tends to a finite value as q decreases enables us to make this conclusion. The comparison between the plane layer and the cylindrical annulus is valid because $R_t = R_m/q$. For $\Lambda = 10$, at the point where the instability is driven purely by differential rotation we find the opposite effect; decreasing q increases the size of the dip.

One practical importance of the work presented here is to nonlinear convection in rapidly rotating systems. It is well known that in the magnetostrophic approximation the most important nonlinear effect is the geostrophic flow $U_G(s)$ associated with Taylor's constraint (see Chapter 1, and for example Soward, 1991). If this flow has the property that it produces a dip in the Ra_c versus R_m

curve then, in the nonlinear problem, subcritical instability will result. We shall be investigating the nonlinear problem in Chapter 5.

Chapter 4

The Effect of Imposed Differential Rotation on Magnetic Stability

In this thesis we concentrate mainly on convective instability. However, a magnetic field may also provide enough energy to drive fluid motions. It can be instructive to eliminate temperature effects to focus on this aspect of the problem. Then, in the linear problem, instability exists for $\Lambda > \Lambda_c$ where Λ_c is some critical value. This magnetic instability may be responsible for the geomagnetic field reversals and the secular variation (McFadden & Merrill, 1993) and has been of interest to many authors. See Fearn (1993) for a review. We note the work of Acheson (1972, 1973, 1983) whose parameter Δ from equation (3.2) may be important. We know that $\Delta > m^2$ is a condition for instability for ideal (diffusionless) systems. Critical levels $\mathbf{k}.\mathbf{B}_0 = 0$ (where $\mathbf{k}$ is the wave-vector) are associated with resistive instability. From (3.2) we expect that a differential rotation which decreases with radius could promote ideal instability. It may also promote resistive instabilities.

In this chapter we shall approach this subset of the dynamo problem in the context of a prescribed differential rotation. We wish to see if the form $\Omega(s)$ affects magnetic stability in a similar way to thermal stability. The work of section 3.4.1 is repeated with appropriate changes (see next section) to basic state, governing equations and boundary conditions. In the same way that linear work in Chapter 3 forms the basis for the nonlinear problem in Chapter 5, the work

in this chapter is a precursor to incorporating the geostrophic nonlinearity into the magnetic stability problem (see Fearn, Lamb, McLean and Ogden, 1997).

4.1 Equations and Solution

We follow the procedure of Section 3.3 but disregard the thermal part of the problem i.e. we set $Ra = 0$ and disregard equation (3.12_3). Note that this also means that q is now absent from the equations. The basic state magnetic field

$$\mathbf{B}_0 = sF\mathbf{1}_\phi, \quad \text{where} \quad F = 4(1-s)(s-s_{ib})/(1-s_{ib})^2 \,, \tag{4.1}$$

is chosen since it is known to be unstable and has been extensively studied (see Fearn 1983b, 1984). For these calculations we use electrically insulating boundaries (from Fearn, 1988)

$$s^2 Db_s + sb_s + i(m^2 + n^2 s^2)b_z/n = 0 \tag{4.2}$$

and

$$b_s = \zeta b_z \tag{4.3}$$

where

$$\zeta = \begin{cases} -iI_{m+1}(ns_{ib})/I_m(ns_{ib}) - im/(ns_{ib}), & s = s_{ib} \\ iK_{m+1}(n)/K_m(n) - im/n, & s = 1 \end{cases} \tag{4.4}$$

We choose insulating rather than perfectly conducting boundaries so that we may use results from Fearn (1988) to provide our starting parameters. The final form of the equations is then

$$\begin{aligned} &[imR_m\Lambda^{-1}\Omega - \Lambda^{-1}(D^2 + 3s^{-1}D + s^{-2} - m^2s^{-2} - n^2) \\ &+ imF(FsD - F - sF')]b_s \\ &- s^{-1}[2i\Lambda^{-1}n + mn^{-1}F^2(m^2 + n^2s^2)]b_z = i\omega b_s \,, \\ &[imR_m\Lambda^{-1}\Omega - \Lambda^{-1}(D^2 + s^{-1}D - m^2s^{-2} - n^2) \\ &- imF(FsD + 4F + sF')]b_z \\ &- (mF/ns)[Fs^2D^2 + 3FsD + F(1-m^2) - 3sF' - s^2F'']b_s = i\omega b_z \,. \end{aligned} \tag{4.5}$$

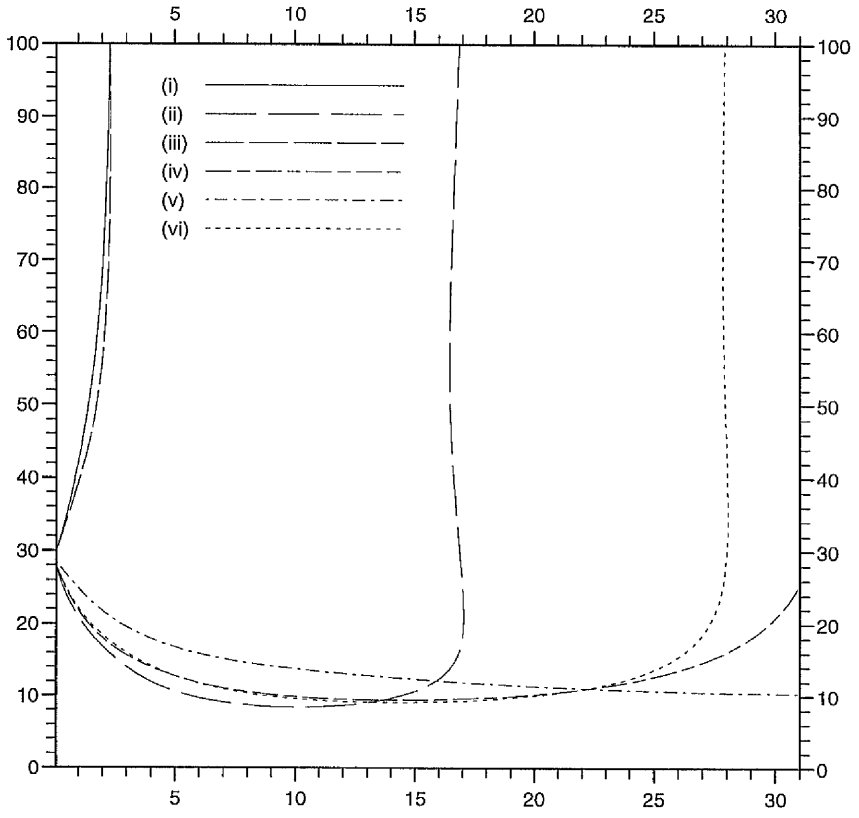

Figure 16 - Graphs of Λ_c against R_m/Λ_c for each form of $\Omega(s)$, see (3.17).

Again, these are solved numerically.

4.2 Results

The effect of differential rotation on magnetic instability is briefly looked at here. We repeat only the work of Section 3.4.1, i.e. we investigate the effect of the different forms of $\Omega(s)$ in the cylindrical annulus. For magnetic instability we are concerned with how the critical value of Λ, Λ_c, varies with R_m. In Figures 16 and 17 we can clearly see the stability dips and the restabilisation effect at higher values of R_m. We present the results in two different forms because both

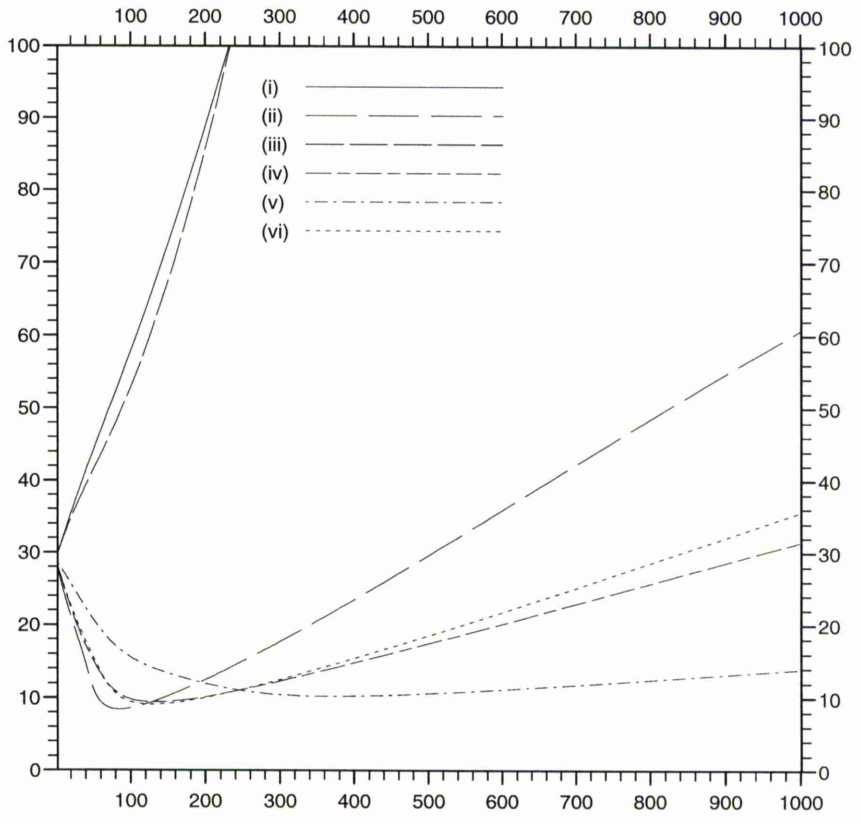

Figure 17 - Graphs of Λ_c against R_m for each form of $\Omega(s)$, see (3.17).

R_m and R_m/Λ_c are convenient parameters for examining this behaviour. These graphs show results for $m = 2$, $n = 3$ and $s_{ib} = 0.35$. We can see that the dips occur at around $R_m = \mathrm{O}(100)$ and at the lowest point Λ_c is about 30% of it's value at $R_m = 0$.

4.3 Conclusions

In the case of magnetic instabilities we have only investigated the effect of the shape of $\Omega(s)$. We find similar results to the thermal case. In fact the forms of $\Omega(s)$ which cause a stability dip in the thermal case are the same ones which

cause a stability dip in the magnetic case. This ties in with Acheson's work and reinforces our conjecture that the proportions of negative gradient are the significant factor. Further exploration of the effect of differential rotation on magnetic instability can be found in Fearn, Lamb, McLean and Ogden (1997). They follow up the work described here with a look a higher values of R_m and ask why a restabilisation occurs when, at first glance, (3.2) suggests that differential rotation should continue to destabilise as R_m is increased. In fact, in a system which is bounded along the rotation axis, there will be large radial derivatives which balance the differential rotation. So it is the closed nature of the geometry which causes the restabilisation. They continue with a nonlinear study by including the geostrophic flow. They find that the form of Ω may contain enough negative gradient to cause a dip in the Λ_c-R_m curve i.e. evidence of subcritical instability. This complements similar work done at finite Ekman number (around $E = 10^{-4}$) by Hutcheson & Fearn (1995). For magnetic instability they only found evidence of supercriticality. It seems, therefore, that there must be some value of E above which the geostrophic flow is not the dominant nonlinear effect. This has implications for finite E calculations where numerical resolution currently restricts attention to $E \geq \mathrm{O}(10^{-4})$.

Chapter 5

Taylor's Constraint in a Cylindrical Annulus

In this chapter we shall extend the cylindrical problem of Chapter 3 into the nonlinear regime. Instead of prescribing the differential rotation, as in Chapter 3, we make it dependent on the magnetic field by identifying $s\Omega(s)$ with the geostrophic velocity $U_G(s)$ described in Chapter 1 [see equation (1.14)]. This introduces a viscous coupling between the core and the mantle which is the dominant nonlinear effect when $|\mathbf{B}|$ is small. This is because, when $|\mathbf{B}| = \mathrm{O}(E^{1/4})$, $|\mathbf{U}_G| = \mathrm{O}(1)$ while all other nonlinear terms are $\mathrm{O}(E^{1/2})$. It is only when Taylor's constraint is satisfied and $|\mathbf{B}|$ can grow to O(1) that the other nonlinear effects become important. In this work, we focus on Ekman states and can therefore neglect all nonlinear effects other than that associated with the geostrophic flow. We can expect the geostrophic flow to provide an equilibration mechanism. We know that $Ra_c = Ra_c(R_m)$ (refer back to, for example, Figure 9 in Chapter 3). If we choose $Ra > Ra_c(0)$, linear theory says that the solution will grow. As this growth occurs, the magnitude of the geostrophic flow also increases because of its dependence on $\mathbf{b}$. Since R_m is representative of this magnitude we see change in the value of Ra_c. Eventually a point will be reached where $Ra = Ra_c(R_m)$ and the solution can no longer grow. See Figure 18 for an illustration of this mechanism.

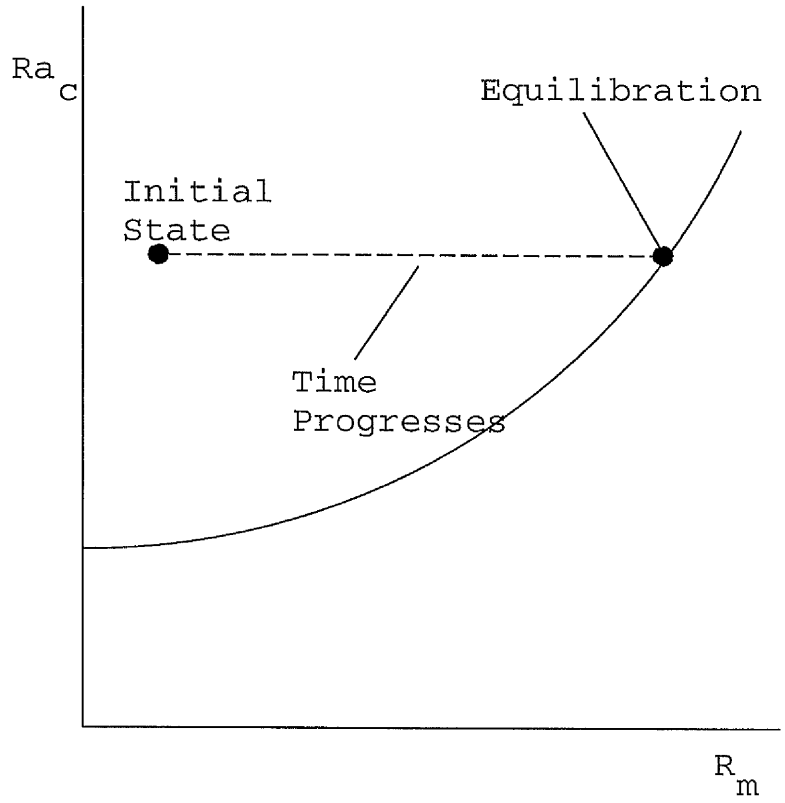

Figure 18 - Equilibration mechanism.

5.1 Equations & Solution

In this problem we use equations (2.13) with $\mathbf{g} = -g_0 s \mathbf{1}_s$.

$$
\begin{aligned}
\mathbf{1}_z \times \mathbf{u} = & -\nabla p + \Lambda[(\nabla \times \mathbf{B}_0) \times \mathbf{b} + (\nabla \times \mathbf{b}) \times \mathbf{B}_0] - qRa\theta s \mathbf{1}_s \,, \\
\frac{\partial \mathbf{b}}{\partial t} = & \nabla \times (\mathbf{u} \times \mathbf{B}_0) + \nabla \times (\mathbf{U}_0 \times \mathbf{b}) + \nabla^2 \mathbf{b} \,, \\
\frac{\partial \theta}{\partial t} + & (\mathbf{U}_0 . \nabla)\theta + (\mathbf{u} . \nabla) T_0 = q \nabla^2 \theta \,, \\
& \nabla . \mathbf{b} = 0 \,, \\
& \nabla . \mathbf{u} = 0 \,.
\end{aligned}
\tag{5.1}
$$

The following expressions describe the basic state. They are chosen so that equations (5.1) are separable in ϕ and z. The temperature gradient is such that

the system is differentially heated between the inner and outer radial boundaries.

$$\mathbf{B}_0 = sF(s)\mathbf{1}_\phi \qquad \mathbf{U}_0 = s\Omega(s)\mathbf{1}_\phi \qquad \nabla T_0 = -\mathbf{1}_s/s \tag{5.2}$$

We shall choose $F(s) = 1$ (a stable field) throughout this chapter but retain it in our equations for future use. We now use a finite cylindrical annulus with top and bottom boundaries at $z = 0, 1$ rather than the infinite cylinder of Chapter 3. We choose these boundaries to be perfectly electrically and thermally conducting and to allow no normal flow through them. This allows us to have equations which are separable in z. So, the expansions for b_z and u_z are

$$[u_z, b_z](s, \phi, z, t) = [\tilde{u}_z, \tilde{b}_z](s, t) \sin nz e^{im\phi} + \text{c.c.} \tag{5.3}$$

and θ, p, u_s, u_ϕ, b_s and b_ϕ are expanded in the form

$$[\theta, p, u_s, u_\phi, b_s, b_\phi](s, \phi, z, t) = [\tilde{\theta}, \tilde{p}, \tilde{u}_s, \tilde{u}_\phi, \tilde{b}_s, \tilde{b}_\phi](s, t) \cos nz e^{im\phi} + \text{c.c.} \tag{5.4}$$

The equations can then be reduced to

$$\begin{aligned}
\frac{\partial \theta}{\partial t} =& [-im\Omega + q(D^2 + s^{-1}D - m^2 s^{-2} - n^2)]\theta \\
&+ s^{-1}\Lambda[(F - FsD + sF')b_s - Fn^{-1}s^{-1}(m^2 + n^2 s^2)b_z] \,, \\
\frac{\partial b_s}{\partial t} =& [-im\Omega + (D^2 + 3s^{-1}D + s^{-2} - m^2 s^{-2} - n^2) \\
&+ imF\Lambda(F + sF' - sFD)]b_s \\
&+ s^{-1}[2n + imn^{-1}F^2\Lambda(m^2 + n^2 s^2)]b_z \,, \\
\frac{\partial b_z}{\partial t} =& [-im\Omega + (D^2 + s^{-1}D - m^2 s^{-2} - n^2) \\
&+ imF\Lambda(sFD + 4F + sF')]b_z \\
&+ imF\Lambda n^{-1}s^{-1}[s^2 FD^2 + 3sFD + (1 - m^2)F - 3sF' - s^2 F'']b_s \\
&- m^2 n^{-1} FqRa\theta \,.
\end{aligned} \tag{5.5}$$

where the tilde above θ, b_s and b_z has been supressed. Note that equations (3.16) can be recovered from (5.5) by replacing b_z with $-ib_z$, b_s with $-b_s$, $\frac{\partial}{\partial t}$ with $-i\omega\Lambda$, Ω with $R_m^{-1}\Omega$ and setting $F = 1$.

In the above model we have heated the boundary at $s = s_{ib}$ and directed gravity radially inwards. We shall also examine the problem when the boundary at $z = 0$ is heated and gravity is directed down the axis of rotation. This results in replacing the term $qRa\theta s\mathbf{1}_s$ in (5.1_1) with $qRa\theta\mathbf{1}_z$ and changing the direction of the temperature gradient (we choose the form $\nabla T_0 = -\mathbf{1}_z$). In order that the problem is still separable in z (i.e. for mathematical convenience) the top and bottom boundaries are taken to be perfect thermal insulators. We then have $\theta = \tilde{\theta}\sin nze^{im\phi} + \text{c.c.}$. The final equations then reduce to

$$\begin{aligned}
\frac{\partial\theta}{\partial t} =&[-im\Omega + q(D^2 + s^{-1}D - m^2s^{-2} - n^2)]\theta \\
&+ \Lambda(sF' + 4F + FsD)b_z \\
&+ \Lambda n^{-1}s^{-1}\big(Fs^2D^2 + 3FsD - 3sF' - s^2F'' - (m^2-1)F\big)b_s\ , \\
\frac{\partial b_s}{\partial t} =&[-im\Omega + (D^2 + 3s^{-1}D + s^{-2} - m^2s^{-2} - n^2) \\
&+ imF\Lambda(F + sF' - sFD)]b_s \\
&+ s^{-1}[2n + imn^{-1}F^2\Lambda(m^2 + n^2s^2)]b_z \\
&- m^2n^{-1}s^{-1}FqRa\theta\ , \\
\frac{\partial b_z}{\partial t} =&[-im\Omega + (D^2 + s^{-1}D - m^2s^{-2} - n^2) \\
&+ imF\Lambda(sFD + 4F + sF')]b_z \\
&+ imF\Lambda n^{-1}s^{-1}[s^2FD^2 + 3sFD \\
&+ (1-m^2)F - 3sF' - s^2F'']b_s\ .
\end{aligned} \tag{5.6}$$

Equations (5.5) and (5.6) will be solved numerically with a timestepping

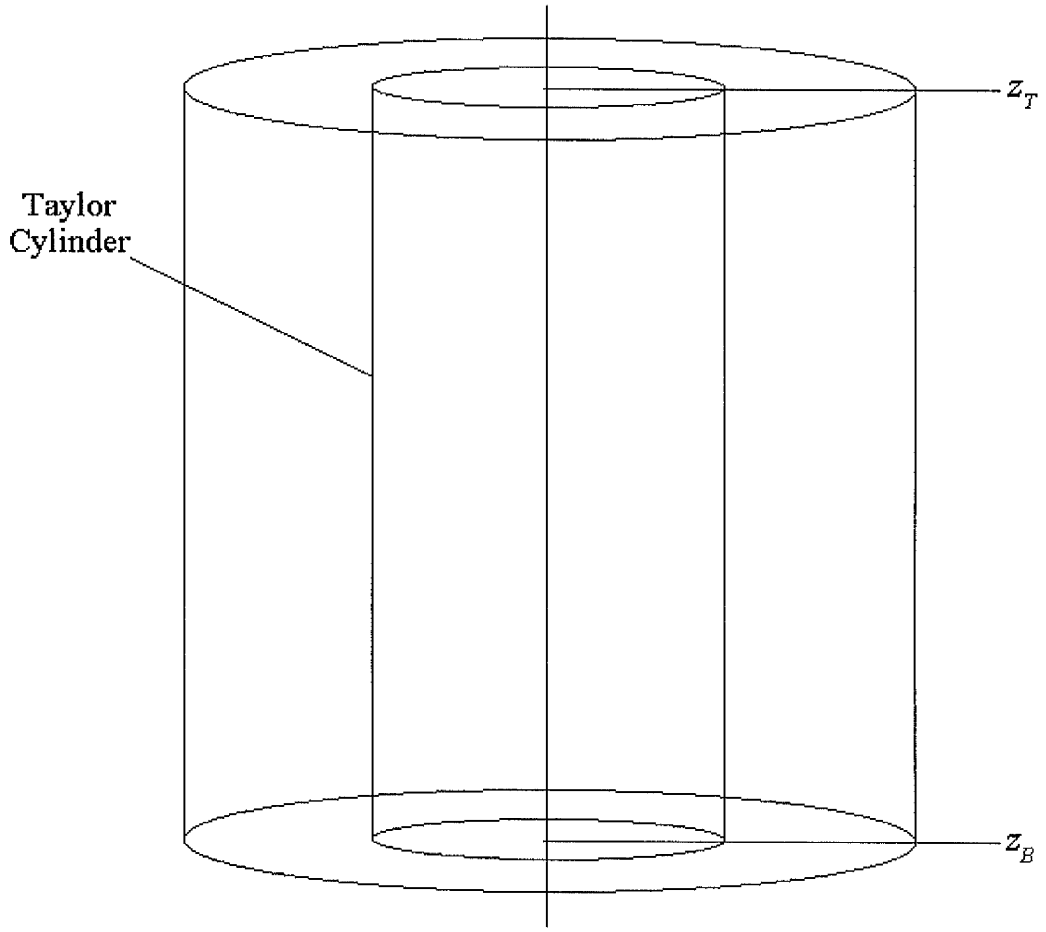

Figure 19 - Taylor Cylinder in a Cylindrical Geometry ($s_{ib} = 0$).

Chebyshev collocation method (see Appendix). Of course, we shall require sidewall boundary conditions and we wish to allow various options here. We may have electrically insulating sidewalls so the magnetic field is matched to an external potential in a similar way to Skinner & Soward (1988, 1990) and we get

$$s(1 + sD)b_s + (m^2 + n^2 s^2)b_z/n = 0 \quad \text{at} \quad s = s_{ib}\ , 1 \tag{5.7}$$

and

$$b_s = \zeta b_z \tag{5.8}$$

where

$$\zeta = \begin{cases} -I_{m+1}(ns_{ib})/I_m(ns_{ib}) - m/(ns_{ib}), & s = s_{ib} \\ K_{m+1}(n)/K_m(n) - m/n, & s = 1 \end{cases} \tag{5.9}$$

and I and K are modified Bessel functions. These equations are modified versions of (4.2)-(4.4) with b_z replaced with $-ib_z$. We may alternatively have perfectly electrically conducting sidewalls for which

$$\frac{im}{s}\left(F^2\Lambda(m^2+n^2s^2)/n \pm D\right)b_z + nDb_z = 0 \tag{5.10}$$

where the $+/-$ corresponds to the inner/outer boundary (this condition has been adapted from Fearn, 1983a, again by replacing b_z with $-ib_z$) and

$$b_s = 0\,. \tag{5.11}$$

We will also allow $s_{ib} = 0$ (i.e. no inner boundary) for which the conditions on the inner boundary from the above will be replaced by

$$b_s = b_z = 0 \quad \text{at} \quad s = 0\,. \tag{5.12}$$

This condition only holds if $m \geq 2$. For the case $m = 1$ we apply the following instead of (5.12)

$$db_s/ds = b_z = 0 \quad \text{at} \quad s = 0\,. \tag{5.13}$$

In all cases the boundaries are isothermal so

$$\theta = 0 \quad \text{at} \quad s = s_{ib}\,, 1\,. \tag{5.14}$$

The final requirement is an appropriate form of $\Omega(s)$. Applying Taylor's constraint (see Chapter 1) to the cylindrical geometry is a simple matter. We note that viscous suction can only occur in Ekman layers at the top and bottom boundaries (see Figure 19) and hence $\psi = 0$ in (1.14) leaving us with

$$U_G(s) = \int_{z_B}^{z_T} \langle(\nabla \times \mathbf{B}) \times \mathbf{B}\rangle_\phi \, dz. \tag{5.15}$$

where we have introduced a further scaling $\mathbf{B} \to (2E)^{-1/4}\mathbf{B}$ to eliminate the need to fix the Ekman number. This is possible because E is an unnecessary parameter when the only nonlinear term is the geostrophic flow and we have made the magnetostrophic approximation. Note that, although formally the contributions to the right-hand side of (5.15) from the axisymmetric and non-axisymmetric parts of $\mathbf{B}$ are comparable in magnitude, the simplicity of our chosen basic state (independent of z) along with the chosen top and bottom magnetic boundary conditions, means that the contribution from the axisymmetric field is negligible (see Fearn 1994 for details). We use (5.15) and the expansions (5.3, 5.4) giving

$$\begin{aligned}\Omega(s) =& \frac{1}{s}\left(\Re(b_s)\Re(\frac{\partial b_\phi}{\partial s}) + \Im(b_s)\Im(\frac{\partial b_\phi}{\partial s})\right) \\ & \frac{1}{s^2}\left(\Re(b_s)\Re(b_\phi) + \Im(b_s)\Im(b_\phi)\right) \\ & - \frac{n}{s}\left(\Re(b_z)\Re(b_\phi) + \Im(b_z)\Im(b_\phi)\right)\end{aligned} \tag{5.16}$$

where b_ϕ can be found in terms of b_s and b_z using (5.1_4). $\Re$ and $\Im$ denote real and imaginary parts respectively. Our nonlinear problem consists of integrating the equations (5.5) or (5.6) forward in time, updating Ω at each timestep, using (5.16). For details see Appendix.

5.2 Results

5.2.1 Reproduction of Linear Results

Before proceeding with nonlinear timestepping calculations we check that our method is sound by reproducing some eigenvalue results of Chapter 3. We prescribe the azimuthal flow rather than using expression (5.16) and find good correspondence. For example, for the parameters $m = 2$, $\Lambda = 1$, $q = 1$, $n = 1$, $s_{ib} = 0$ and $\Omega(s) = \sin \pi s$ with perfectly conducting sidewall boundaries and

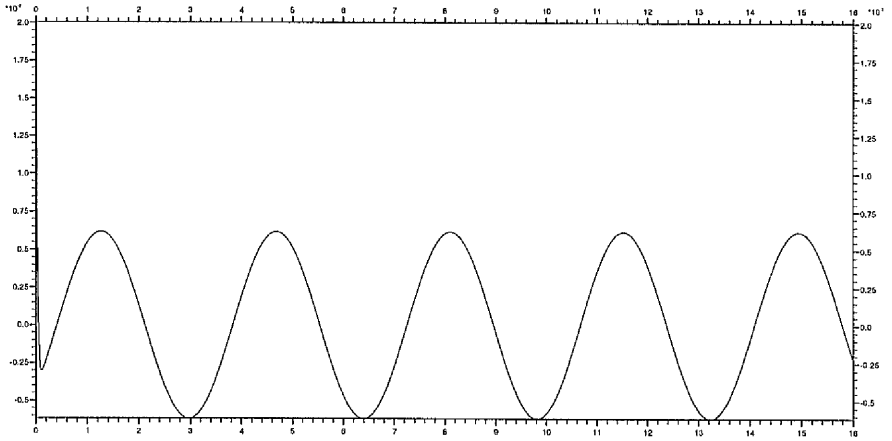

Figure 20 - Amplitude of solution (proportional to θ) against time (τ_η) for $Ra = 29.683$, $m = 2$, $\Lambda = 1$, $q = 1$, $n = 1$, $s_{ib} = 0$ with perfectly conducting sidewall boundaries and radial gravity.

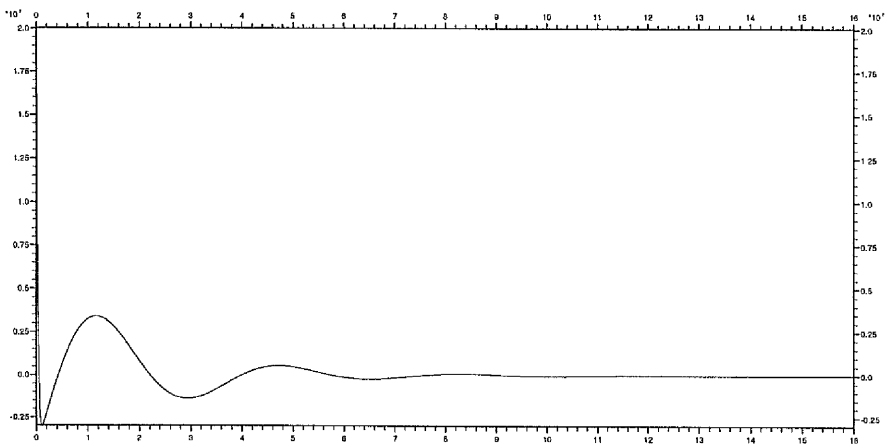

Figure 21 - As Figure 20 but for $Ra = 29.0$.

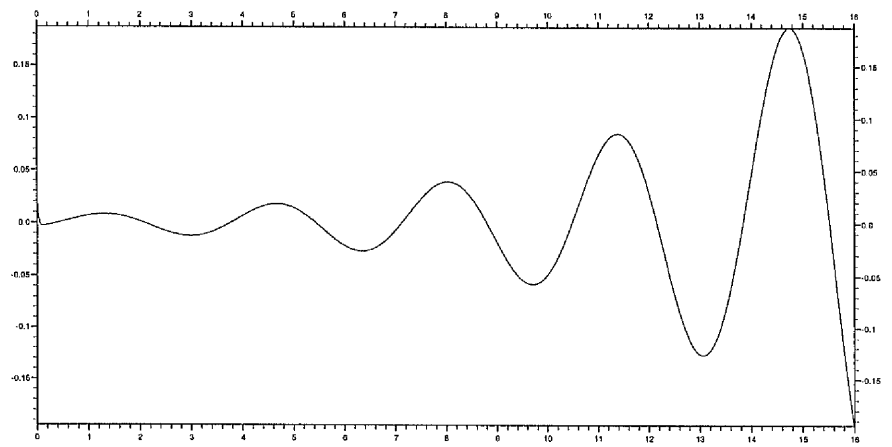

Figure 22 - As Figure 20 but for $Ra = 30.0$.

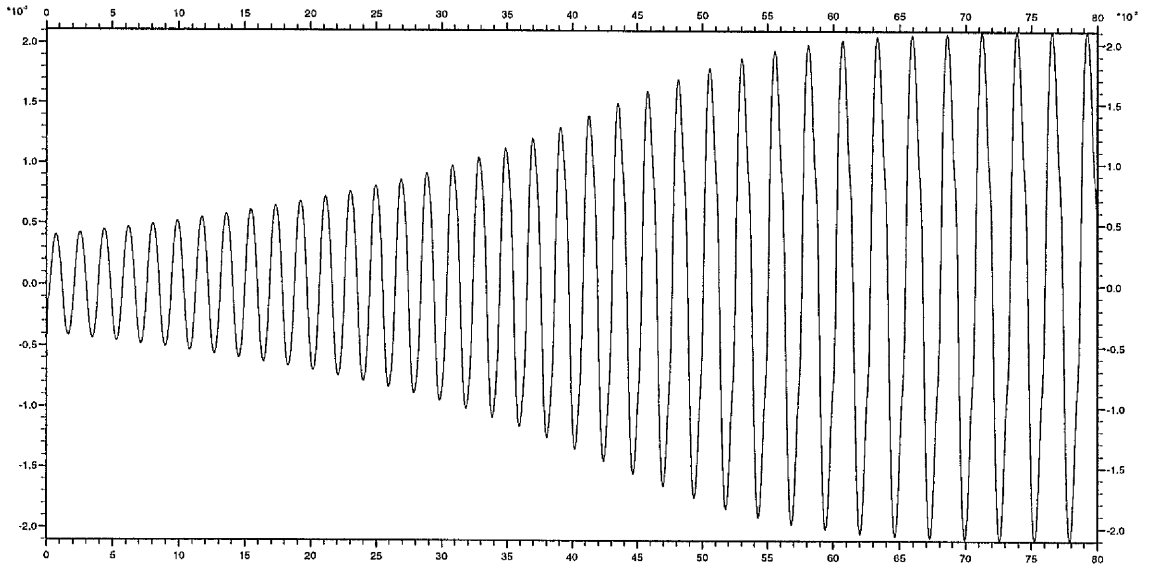

Figure 23 - Amplitude of solution against time. This figure shows the evolution to an Ekman state for parameters $\Lambda = 1$, $m = 2$, $n = 3$, $q = 1$, $s_{ib} = 0$ with insulating sidewall boundaries and axially directed gravity.

radial gravity we can find $Ra_c(R_m = 0) = 29.683$ (c.f. Figure 12). Figure 20 shows the time evolution of the solution amplitude with $Ra = 29.683$. We see that the solution is neither growing or decaying indicating that $Ra = Ra_c$. Figures 21 and 22 show the same for $Ra = 29.0$ and $Ra = 30.0$ which illustrate decay and growth respectively as we would expect, reinforcing the stability of $Ra = Ra_c$ shown in Figure 20.

We now move into the nonlinear regime. Note that from now on all the figures and tables in this chapter we have $\Lambda = 1$, $q = 1$, $m = 2$, $n = 3$, $s_{ib} = 0$, insulating boundaries and axially directed gravity (unless otherwise indicated).

5.2.2 Existence of Ekman States

Initially we wish to be sure that we can find Ekman states. In other words, we wish to ensure that the geostrophic flow is able to equilibrate the solution. Indeed, we find that this can happen and we illustrate for the following parameter

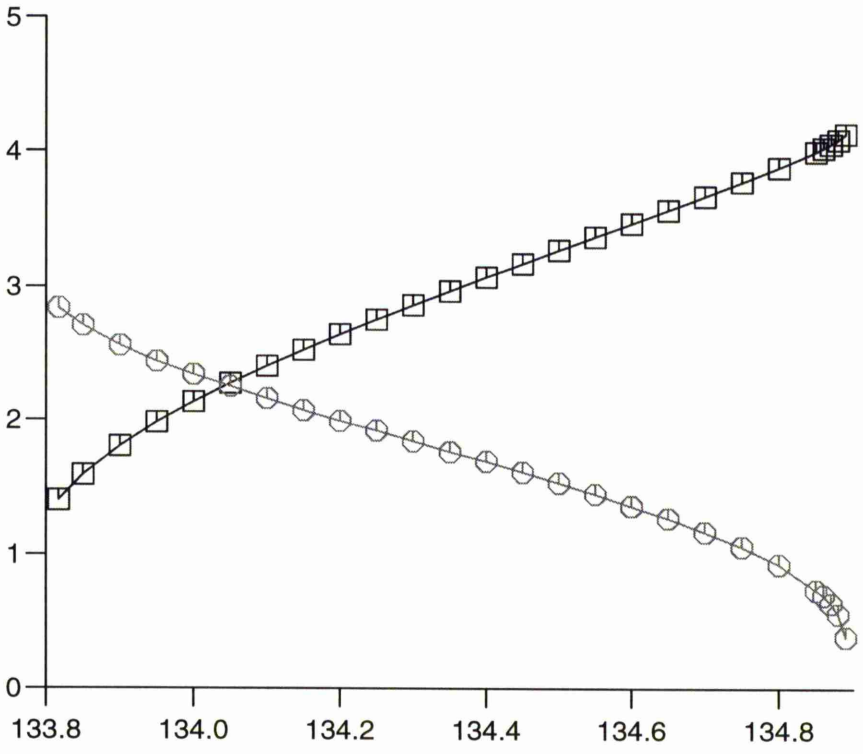

Figure 24 - Graph of equilibrated amplitude, a_E (squares), and equilibrated frequency, ω_E (circles), against Ra for $\Lambda = 1$, $m = 2$, $n = 3$, $q = 1$, $s_{ib} = 0$, $Ra_c = 133.82$, insulating boundaries and axially directed gravity.

values: $\Lambda = 1$, $q = 1$, $m = 2$, $n = 3$ and $s_{ib} = 0$ with axial gravity and insulating sidewall boundaries. Setting $\Omega(s) = 0$ allows us to find the linear critical $Ra_c = 133.82$. We then set $\Omega(s)$ via expression (5.16) and fix $Ra = 134.0$ (knowing from the work reviewed in Chapter 1 that Ra must be sufficiently close to Ra_c in an Ekman state). The result is shown in Figure 23 which graphs the variation of the amplitude of solution with time. As we might expect the solution grows until the geostrophic flow is sufficient to equilibrate it. The equilibrated amplitude, a_E, is proportional to the amplitude of the temperature perturbation θ. The effect of U_G is to modify the effective value of Ra_c as time progresses until it has the same value as the current, fixed value of Ra. Figure 24 shows how the equilibrated amplitude develops with increasing Ra. In this example,

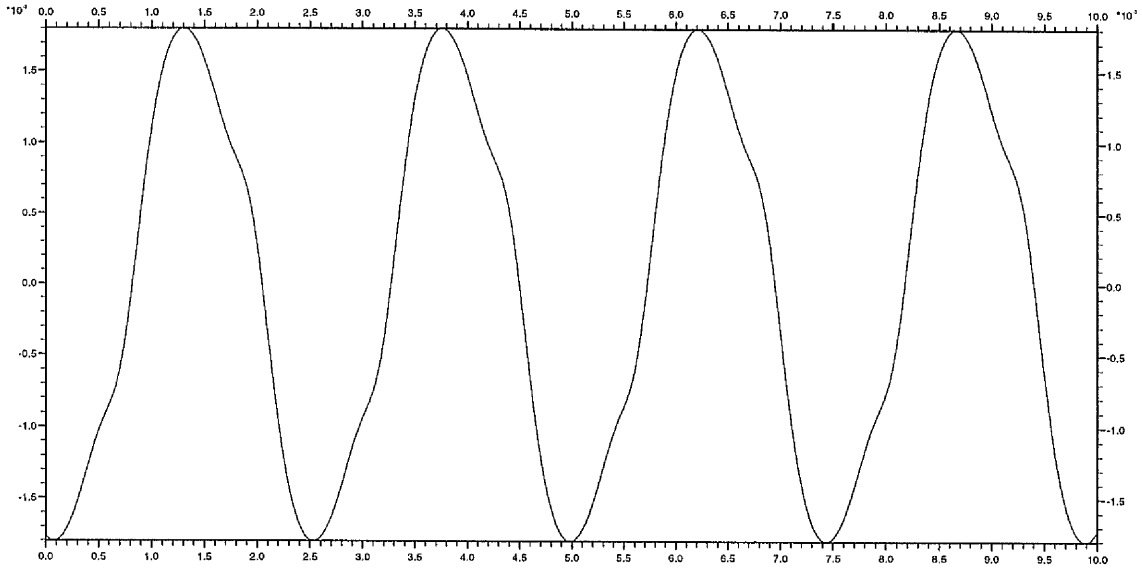

Figure 25 - Amplitude of solution against time for parameters $Ra = 133.9$, $\Lambda = 1$, $m = 2$, $n = 3$, $q = 1$, $s_{ib} = 0$ with insulating sidewall boundaries and axially directed gravity.

it is only over this small region that we find Ekman states.

We shall denote the highest value of Ra at which we can find an Ekman state as Ra_T. In this case $Ra_T = 134.90$. Note the sharp decrease in equilibrated frequency, ω_E, as Ra approaches Ra_T. This has the consequence of making the numerical solution more difficult. As $Ra \to Ra_T$, the decreasing frequency requires progressively more and more timesteps to resolve the equilibrated solution. Also, we are not able to increase the timestep used because the solution incorporates large gradients (see Figure 27). Ultimately, the amount of processor time needed becomes prohibitive. Figures 25 and 26 show the time-dependent behaviour of the equilibrated wave and the equilibrated solutions at $Ra = 133.9$ (i.e. just above Ra_c). Figures 27 and 28 show the same for $Ra = 134.8$ (i.e. just below Ra_T). In these cases we can see that Ω (which is also time dependent) is generally decreasing outwards and has $G_\Omega < 0$. See equation (3.18) for

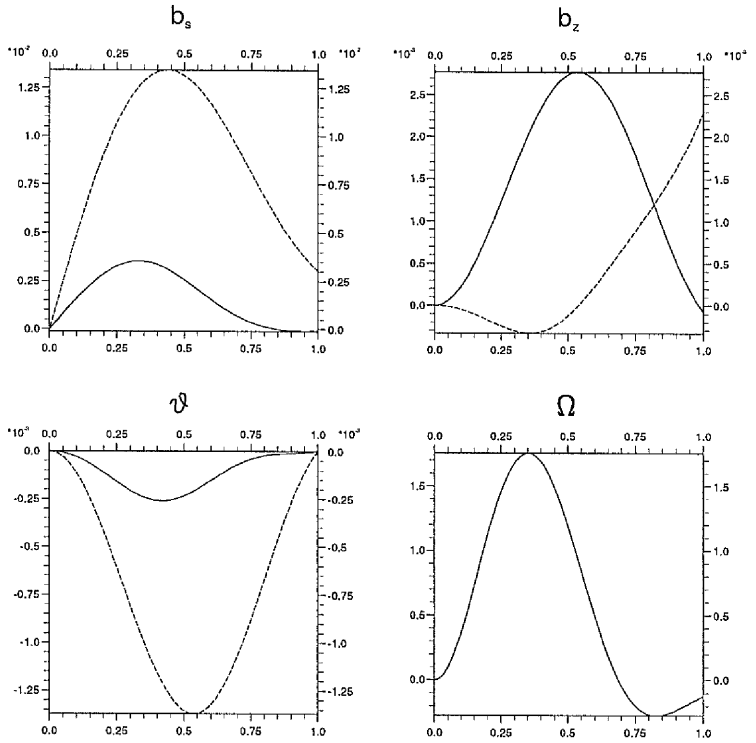

Figure 26 - Solution after equlibration has been reached for parameters $Ra = 133.9$, $\Lambda = 1$, $m = 2$, $n = 3$, $q = 1$, $s_{ib} = 0$ with insulating sidewall boundaries and axially directed gravity. θ, b_s and b_z are time-dependent so they are normalised such that $\max\{b_z\} = \max\{|\mathbf{b}|\}$.

definition of G_Ω. Remember from Chapter 3 that these are the types of flow that have a destabilising effect and can be subcritical. However, the value of G_Ω is only marginally less than zero so we may expect the destabilising influence to be minimal. Figure 24 shows some indication of subcritical solutions, the solution at $Ra = Ra_c$ has a finite amplitude and is not sinusoidal. More obvious subcritical solutions do exist for some configurations of the system (see Section 5.2.4).

5.2.3 Existence of Taylor States

We have seen in Figure 24 that the Ekman region can only be followed up to $Ra = Ra_T$. Figure 29 shows what happens to our numerical solution when $Ra > Ra_T$. The solution is not oscillatory but has increasing growth rate beyond

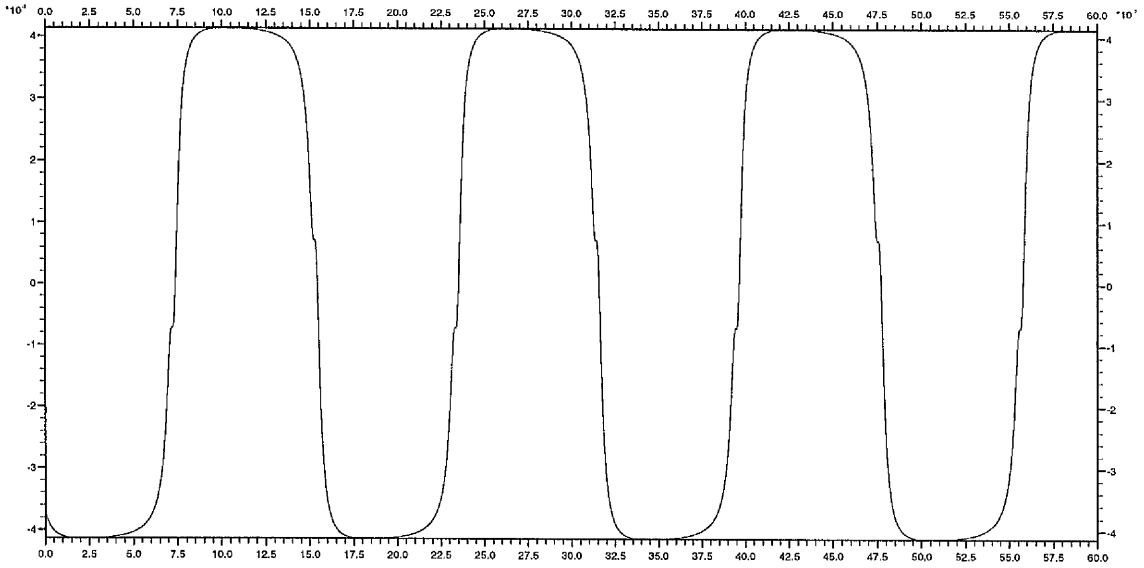

Figure 27 - As Figure 25 but for $Ra = 134.8$.

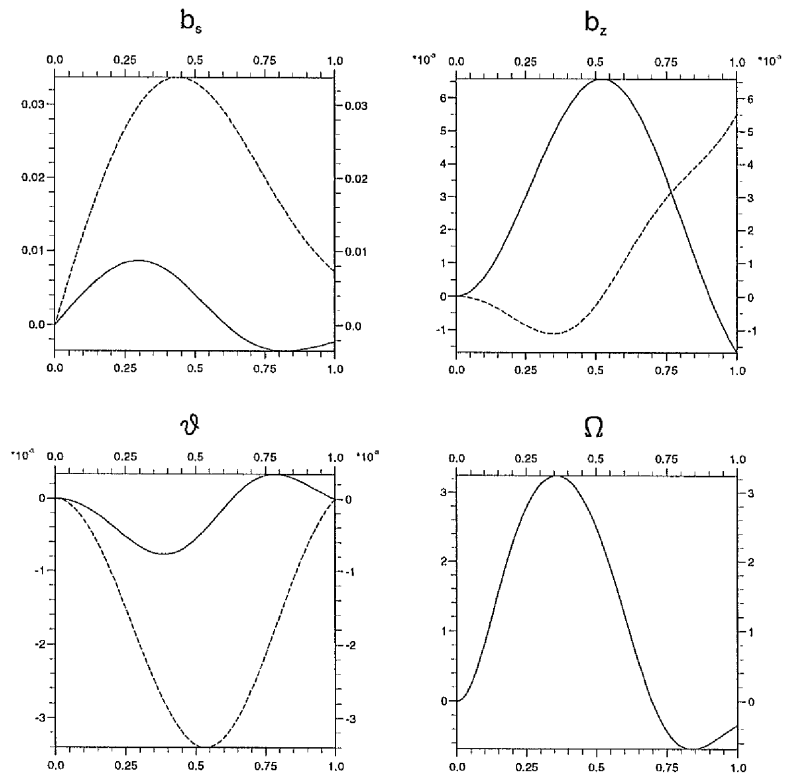

Figure 28 - As Figure 26 but for $Ra = 134.8$.

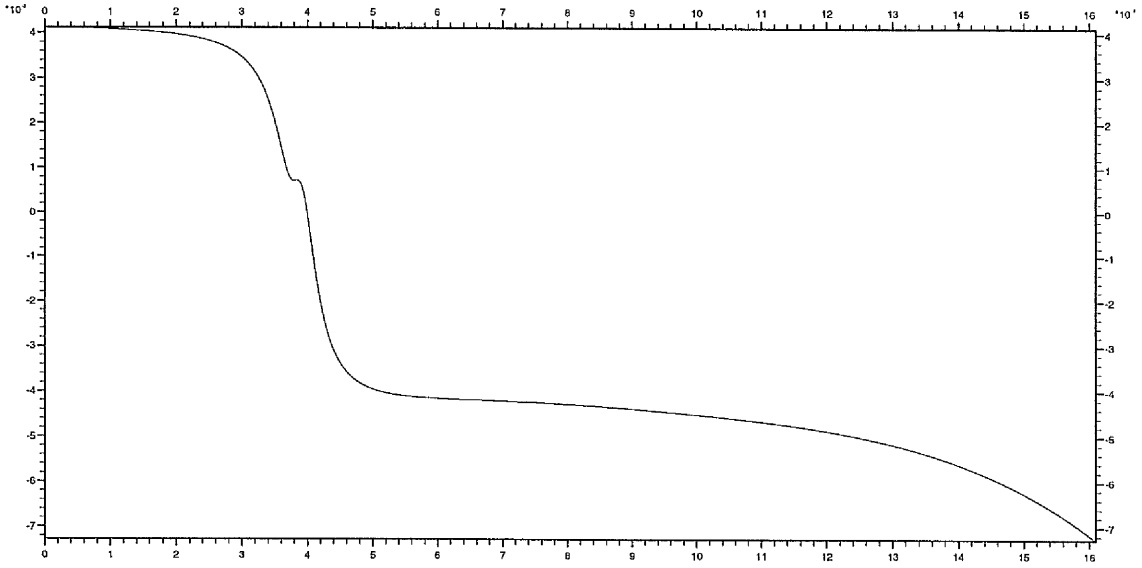

Figure 29 - As Figure 25 but for $Ra = 134.9$.

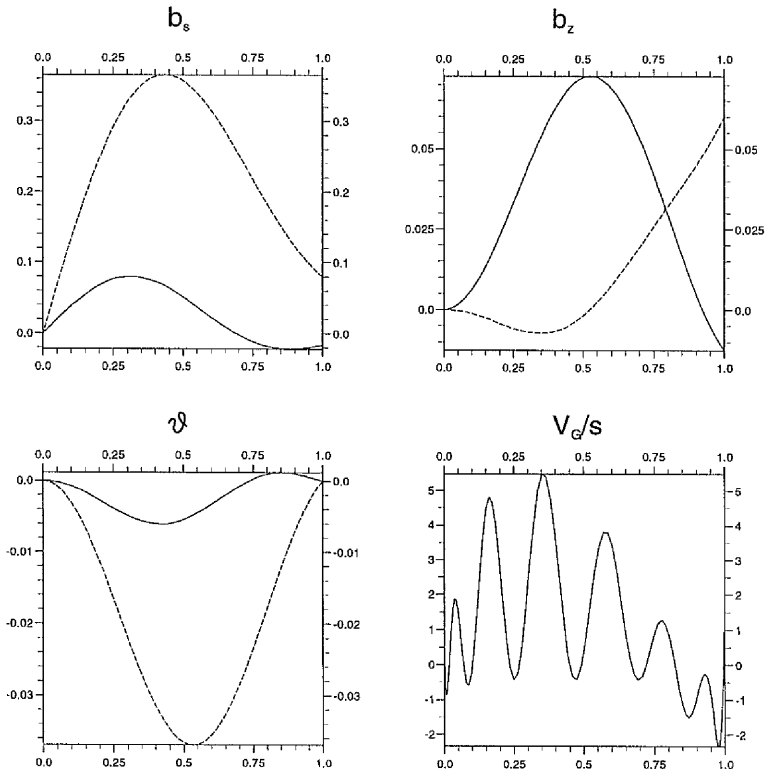

Figure 30 - As Figure 26 but for $Ra = 134.9$ and at $t = 16$ (i.e. just before numerical breakdown).

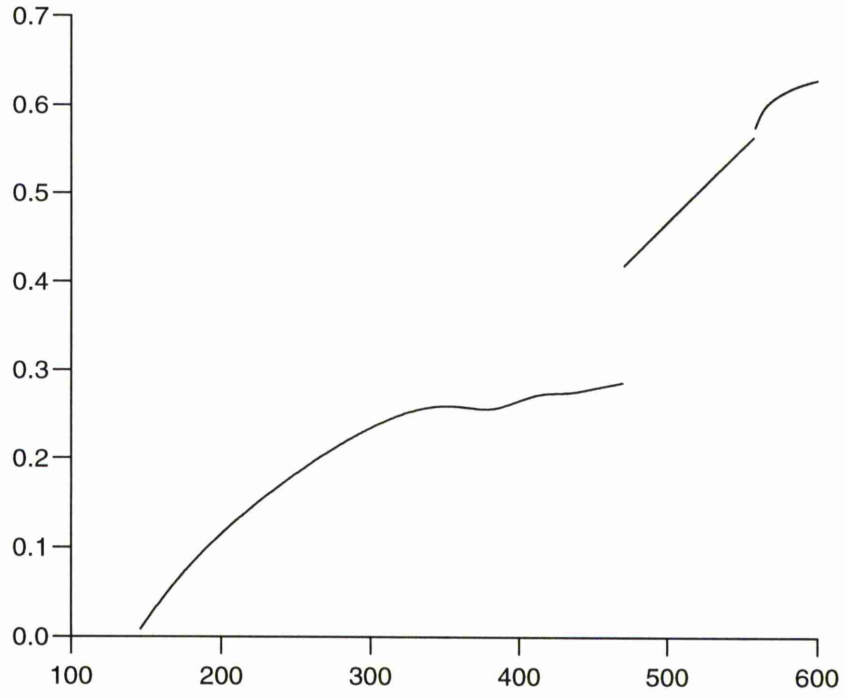

Figure 31 - Graph of a_E against Ra for $\Lambda = 1$, $m = 2$, $n = 3$, $q = 1$, $s_{ib} = 0$, insulating boundaries and radially directed gravity.

time $t = 5$. Just past $t = 16$ the numerical solution breaks down and can no longer be followed. The equilibration mechanism is no longer succeeding and the amplitude of solution grows towards infinity. We have taken this to indicate that we are close to (but not necessarily at) a Taylor state. Hence our value of Ra_T must be interpreted with caution. It is not the same as the Ra_T described in Chapter 1 which indicates the point at which a Taylor state first occurs. Our Ra_T indicates the point beyond which there is no Ekman state. Figure 30 shows the solution just before breakdown and indicates that we are indeed close to a Taylor state. In comparison with Figure 28 we can see an increase in amplitude by a factor of 10 but $|\Omega|$ remains of the same order even though $|\Omega| \propto |\mathbf{b}|^2$. This illustrates the cancellation effect associated with a Taylor state.

The behaviour described in this and the last section is typical of cases we

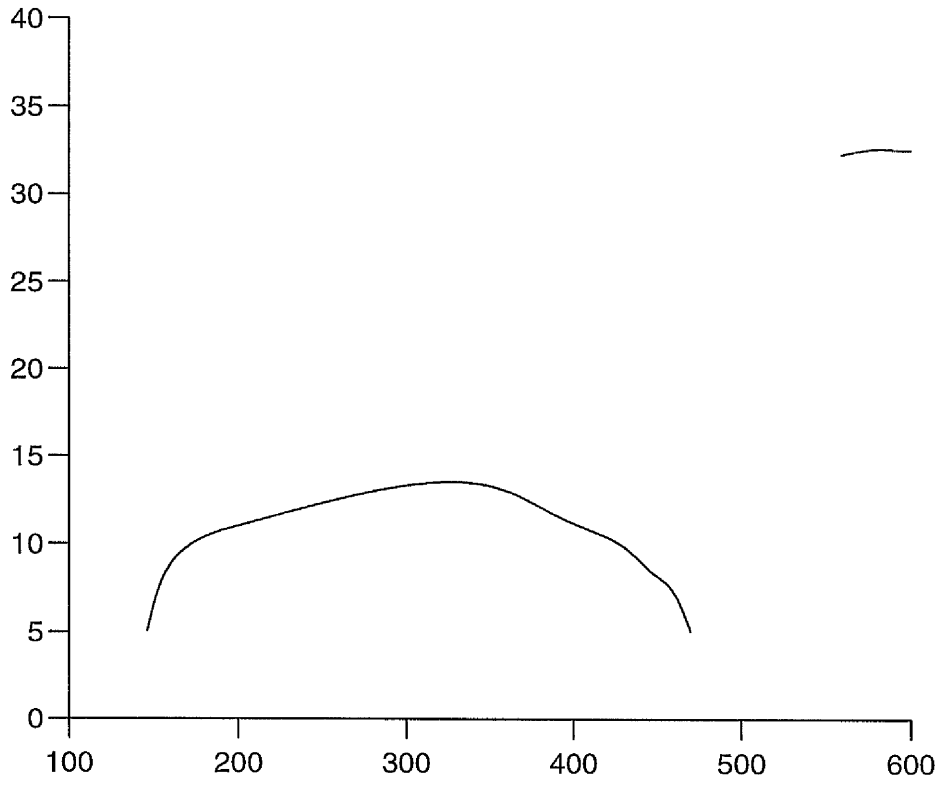

Figure 32 - Graph of ω_E against Ra for $\Lambda = 1$, $m = 2$, $n = 3$, $q = 1$, $s_{ib} = 0$, insulating boundaries and radially directed gravity.

have looked at with $\Lambda = 1$ and axial gravity (see next section for more on this). We always find non-oscillatory solutions just before numerical breakdown and always find cancellation occuring in Ω. We also always find that $\omega \to 0$ at this point but we would hesitate to associate Taylor states with $\omega = 0$ solutions since Skinner and Soward (1990) found oscillatory Taylor solutions. It may be the case that, were we able to avoid numerical breakdown, ω would pass through zero before a Taylor solution was reached.

5.2.4 Non-Existence of Taylor States

In Figure 31 we show the behaviour of the equilibrated amplitude with increasing Ra for the radial gravity case. In comparison with Figure 24 (axial

gravity) we can see that the Ekman region extends much further. In fact we would infer that there is no point at which $Ra = Ra_T$ and the Ekman region extends to $Ra \to \infty$. In one case we looked at ($n = 5$, $m = 2$, $\Lambda = 1$ and $q = 1$) we went as far as $Ra = 25000$ in the Ekman region. In fact in all cases with radial gravity and $\Lambda = 1$ we found no numerical breakdown as described in the previous section. Figure 32 shows how the equilibrated frequency behaves over the same region as Figure 31. Note that for $470 < Ra < 559$, steady solutions ($\omega_E = 0$) were found. Figures 33 to 42 show the different shapes of waves that occur over this region. There is a bifurcation (here the branches overlap) at $Ra \approx 471$ from a wavelike solution to a steady one and a bifurcation at $Ra \approx 559$ from the steady solution to a vacillating wave. In the steady solution region notice that the forms of b_s, b_z and θ are not particularly different from those in the other other regions. Increasing Ra further will likely result in more interesting wave shapes. Note that every form of Ω in these figures has $G_\Omega > 0$.

Gravity	s_{ib}	B.C.	Ra_c	Ra_T	ω_c
Radial	0.35	P.C.	148.84	–	2.91
Radial	0.0	P.C.	122.17	–	3.17
Radial	0.35	Ins.	247.91	–	4.41
Radial	0.0	Ins.	145.22	–	3.57
Axial	0.35	P.C.	134.13	137.42	4.48
Axial	0.0	P.C.	119.13	122.76	4.39
Axial	0.35	Ins.	164.32	$< Ra_c$	3.72 (†)
Axial	0.0	Ins.	133.82	134.90	3.51

Table 3 - Values of Ra_c and Ra_T for $m = 2$, $n = 3$, $\Lambda = 1$ and $q = 1$ with different combinations of gravity, inner boundary radius and sidewall boundary conditions (B.C.) - either perfectly electrically conducting (P.C.) or insulating (Ins.).

In Table 3 we show results for $m = 2$, $n = 3$, $\Lambda = 1$ and $q = 1$. Of specific note is the case with axial gravity, $s_{ib} = 0.35$ and insulating boundaries (†). It

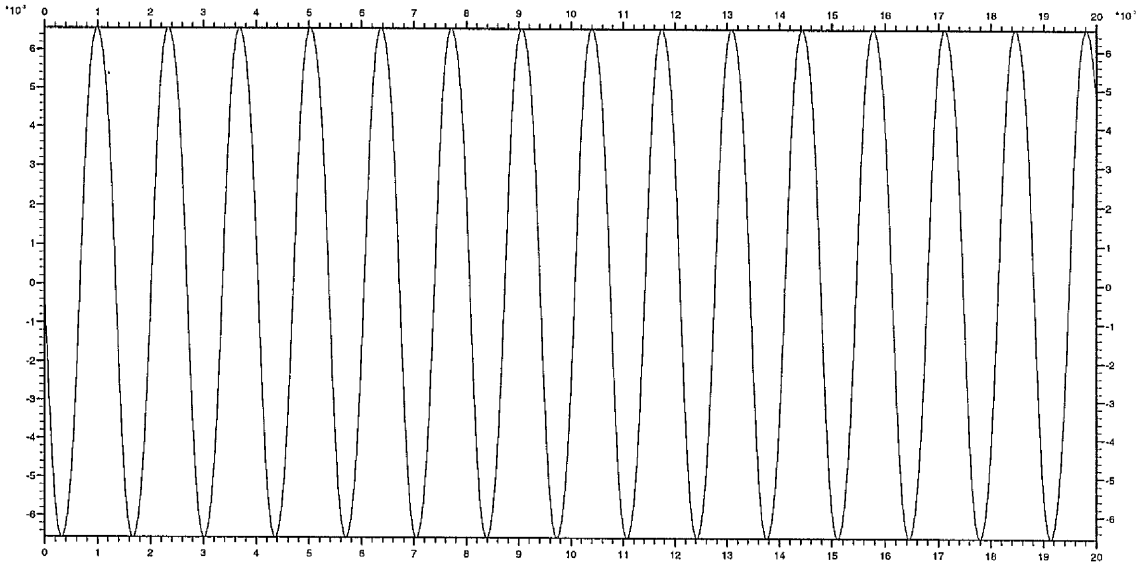

Figure 33 - As Figure 25 but for $Ra = 146.0$ and radially directed gravity.

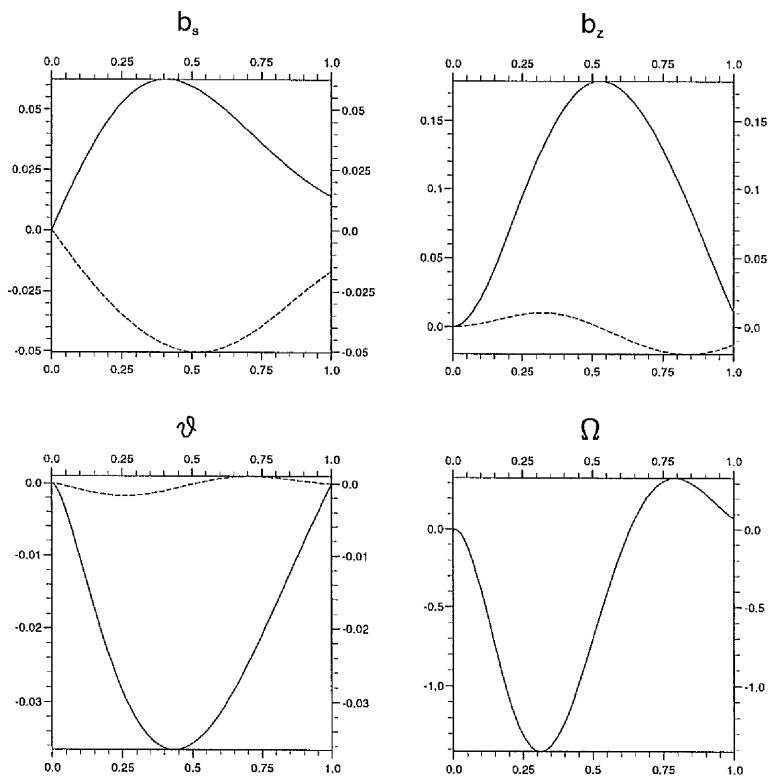

Figure 34 - As Figure 26 but for $Ra = 146.0$ and radially directed gravity.

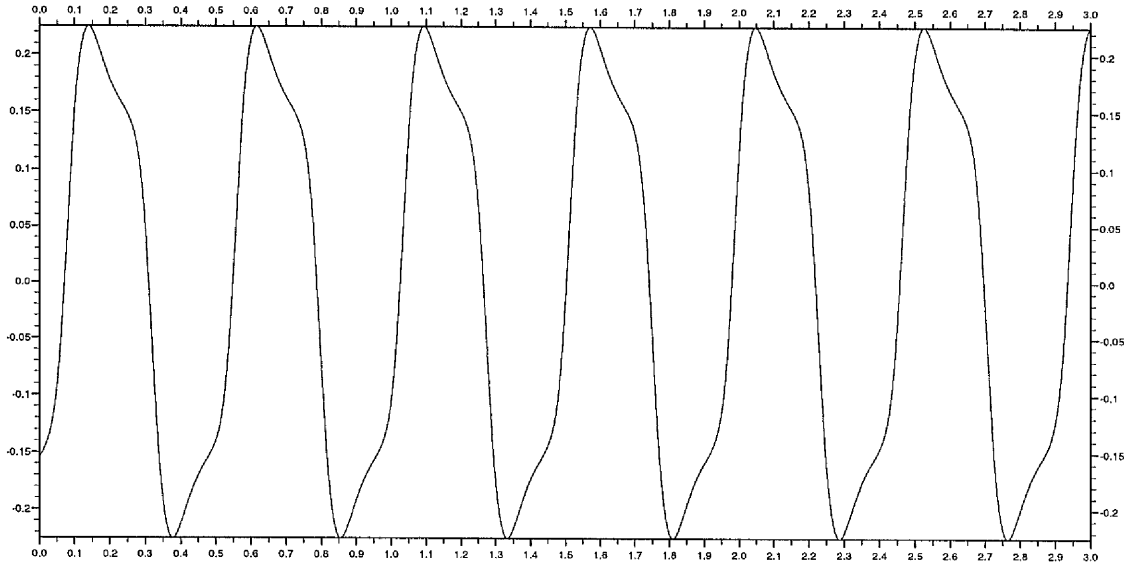

Figure 35 - As Figure 25 but for $Ra = 290.0$ and radially directed gravity.

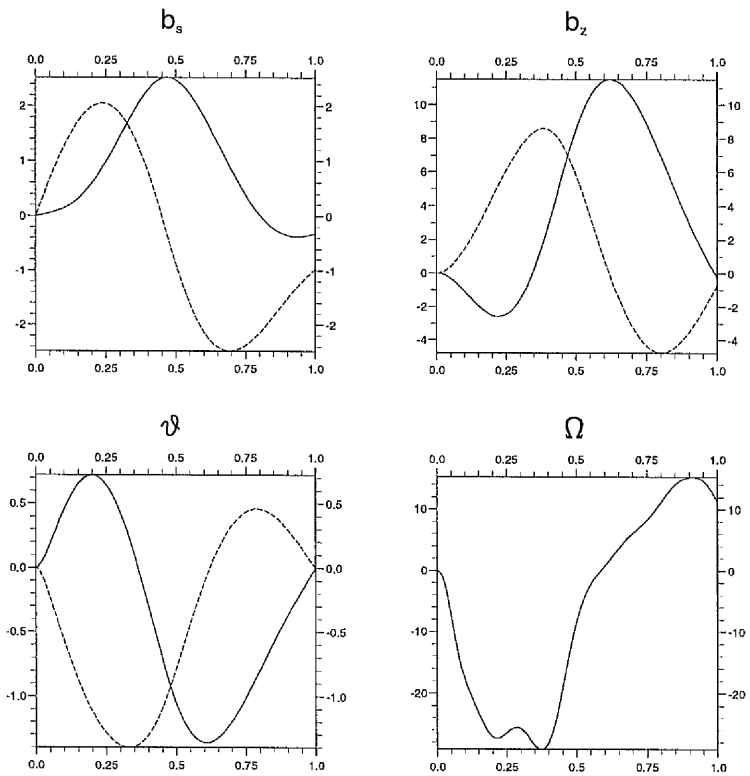

Figure 36 - As Figure 26 but for $Ra = 290.0$ and radially directed gravity.

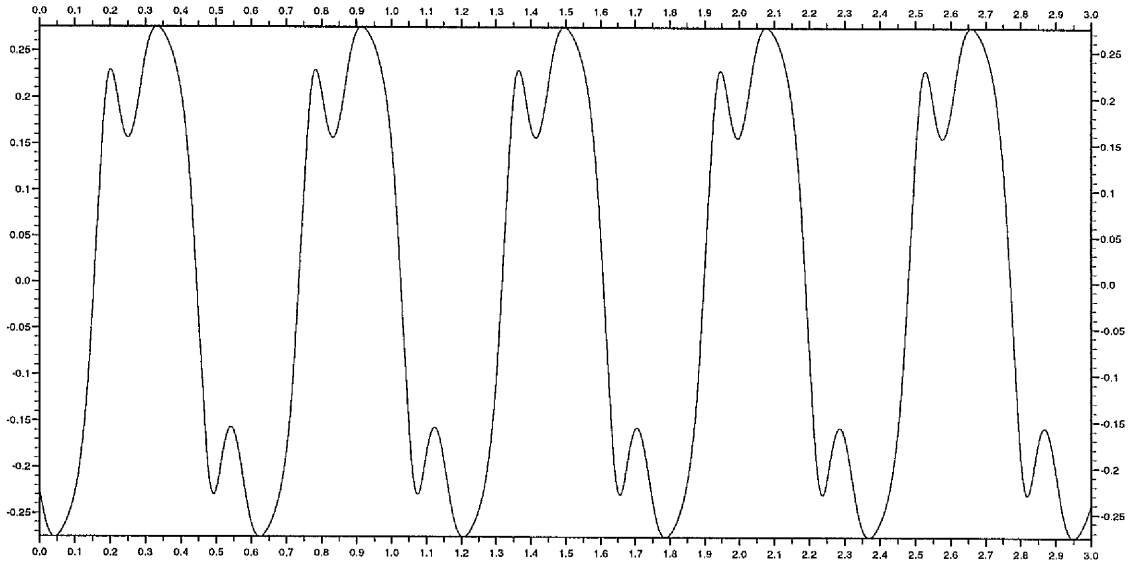

Figure 37 - As Figure 25 but for $Ra = 410.0$ and radially directed gravity.

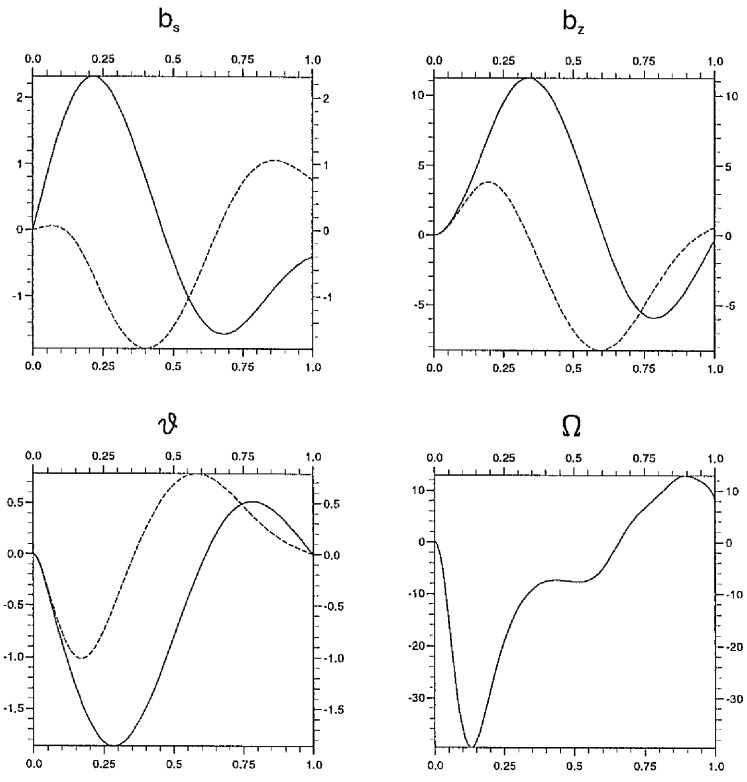

Figure 38 - As Figure 26 but for $Ra = 410.0$ and radially directed gravity.

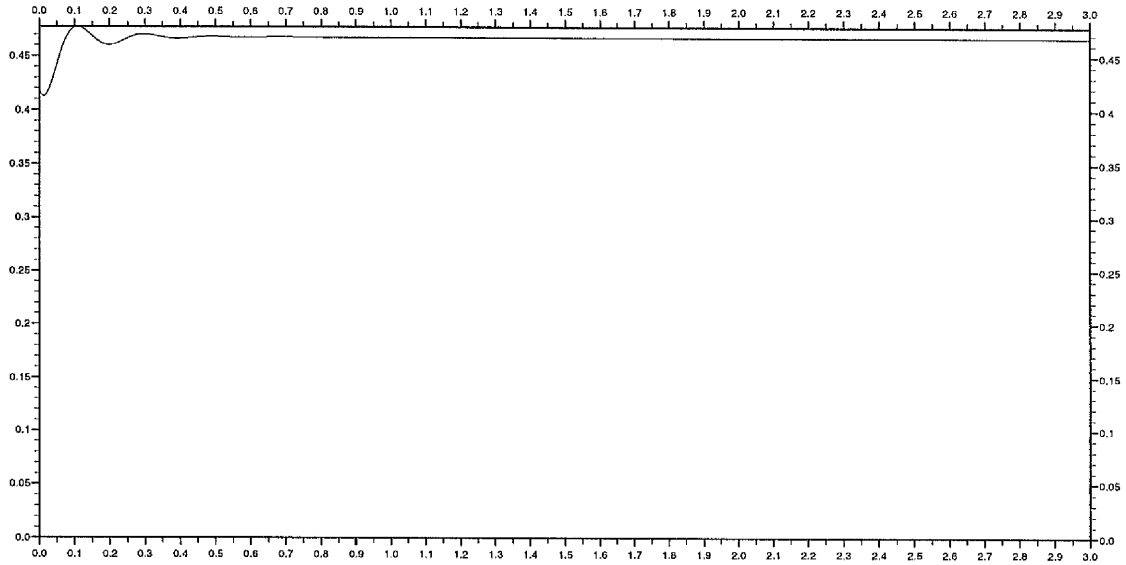

Figure 39 - As Figure 25 but for $Ra = 500.0$ and radially directed gravity.

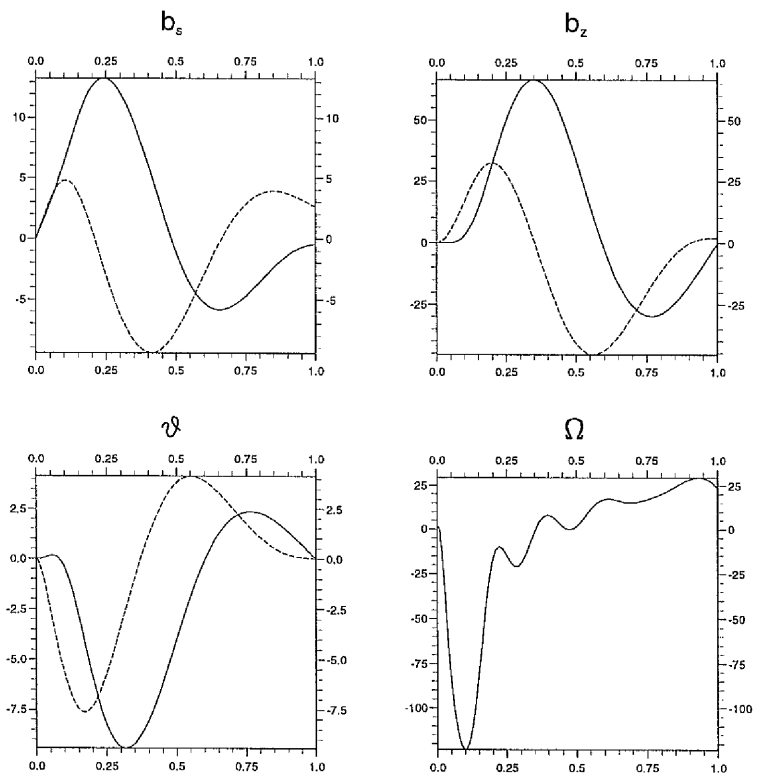

Figure 40 - As Figure 26 but for $Ra = 500.0$ and radially directed gravity.

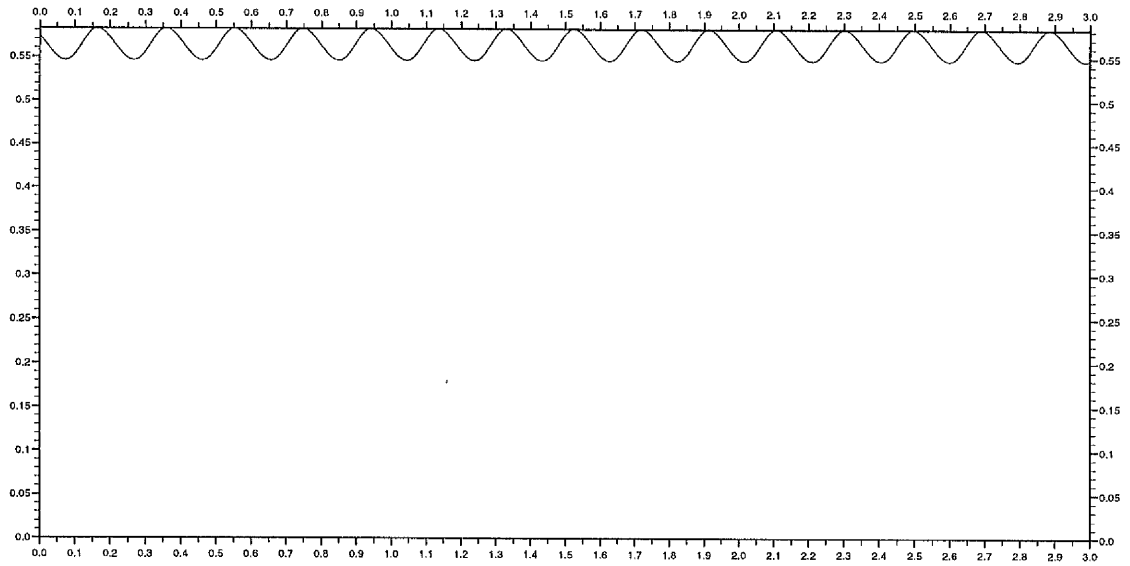

Figure 41 - As Figure 25 but for $Ra = 560.0$ and radially directed gravity.

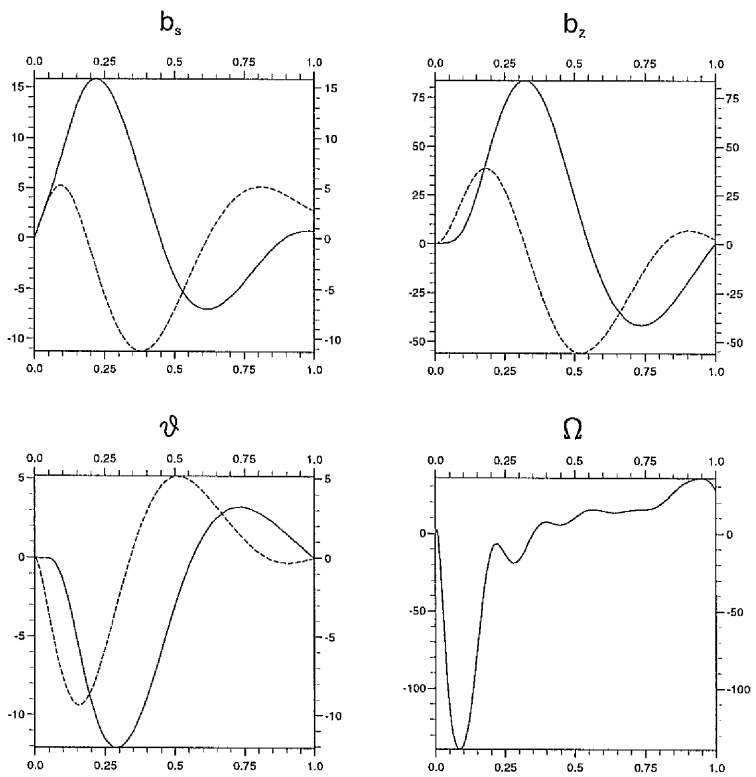

Figure 42 - As Figure 26 but for $Ra = 560.0$ and radially directed gravity.

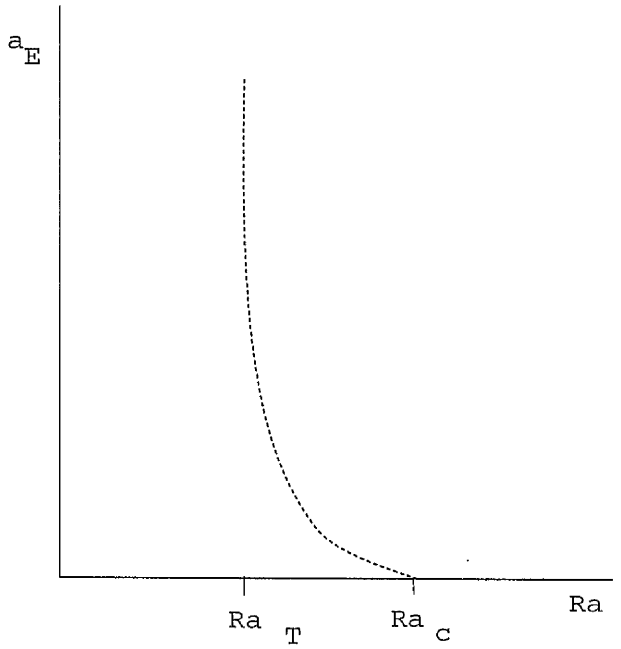

Figure 43 - Sketch of behaviour of equilibrated amplitude, a_E, with Rayleigh number, Ra, when $Ra_T < Ra_c$ and no Ekman states exist.

has $Ra_T < Ra_c$. In this case we could not determine the value of Ra_T since we could not find an Ekman state. Figure 43 illustrates this situation (compare with Figure 24). However, we have found instances with subcritical Ekman states. For example, for the parameters $m = 2$, $n = 1$, $\Lambda = 1$, $q = 1$ and $s_{ib} = 0$ with axial gravity and insulating boundaries we find $Ra_c = 11.7817$, $Ra_T = 11.7453$ and a subcritical $Ra_s = 11.7366$.

If $Ra \leq Ra_s$ the solution decays, there is an Ekman region between Ra_s and Ra_T and numerical breakdown for $Ra > Ra_T$ (see Figure 44). For $Ra < R_c$ it is clear that the ability to find subcritical states is dependent on whether the intial state of the system is stable or unstable. For $G_\Omega > 0$ flows it is always stable but for $G_\Omega < 0$ flows it may be either since the perturbation at $t = 0$ determines the position in the $Ra_c - R_m$ curve. If we begin in a stable state we will not be able to find Ra_T.

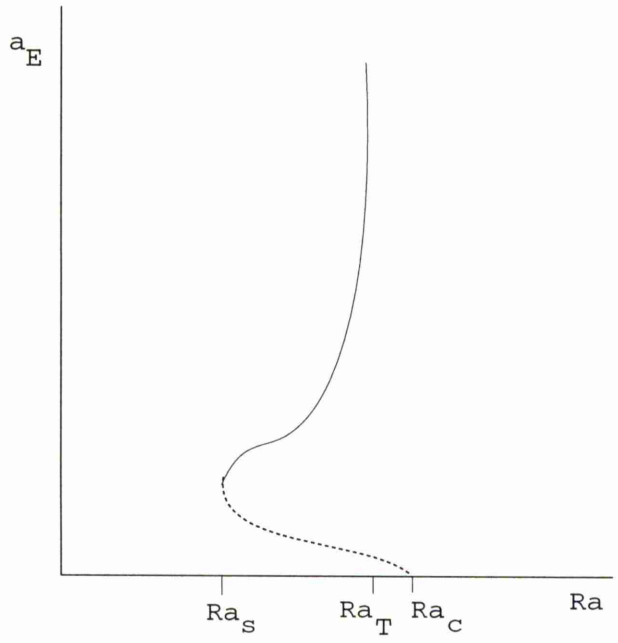

Figure 44 - Sketch of behaviour of equilibrated amplitude, a_E, with Rayleigh number, Ra, when $Ra_T < Ra_c$ and Ekman states do exist.

5.2.5 Effect of Varying Boundary Conditions

In Table 3 the effect of replacing perfectly electrically conducting sidewall boundaries with insulating ones can be seen. The values of Ra_c (and Ra_T where applicable) are larger i.e. insulating boundaries result in a more stable system than perfectly conducting boundaries. The same is also true of including an inner boundary where there was none. We therefore infer that systems using these varying combinations of boundary conditions will behave similarly. The only qualitative difference we encounter is in (†). This shows that some combinations will allow $Ra_T < Ra_c$. We may only assume this for $m \geq 2$. If $m = 1$ we have different boundary conditions at $s = s_{ib} = 0$.

5.2.6 Effect of the Elsasser Number

Figure 45 shows the effect of varying Λ on the values of Ra_c and Ra_T for $m = 2$, $n = 3$, $q = 1$, $s_{ib} = 0$, insulating sidewall boundaries and axially directed

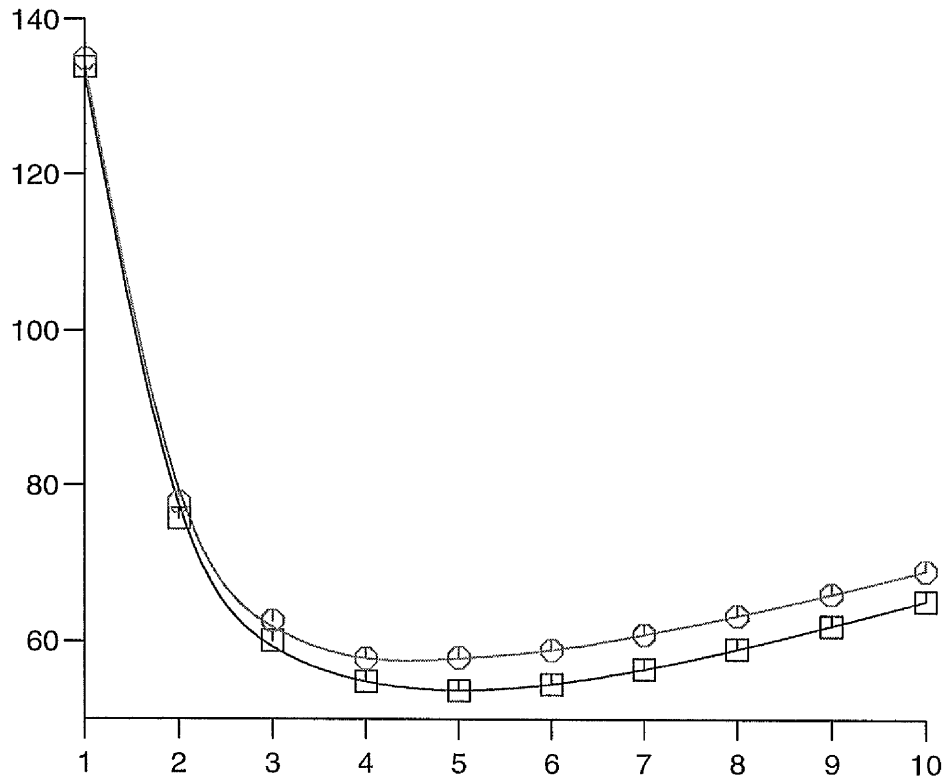

Figure 45 - Graph of Ra_c (squares) and Ra_T (circles) against Λ for $m = 2$, $n = 3$, $q = 1$, $s_{ib} = 0$, insulating sidewall boundaries and axially directed gravity.

gravity. The effect on the critical Rayleigh number is well known. There is a minimum value when $\Lambda = O(1)$. For the stable field $F = 1$ we find the same is true for Ra_T and that the two numbers are always close together throughout the region.

More significantly we have looked at the effect on the radial gravity system of a smaller value of Λ. The "anti-Taylor inequality" of Jones & Roberts described in Chapter 1 suggests that we may be able to find a value of Ra_T if we do this (i.e. Taylor states may exist at smaller values of Λ). From Figure 45 we may reasonably expect $Ra_T \approx Ra_c$. Indeed, at $\Lambda = 0.1$ we find $Ra_c = 1389.79$ and $Ra_T = 1389.81$. Following from Jones and Roberts work we would

therefore expect that there must exist some Λ_0, with $0.1 < \Lambda_0 < 1$ (we have not investigated intermediate values), such that Taylor states exist for $\Lambda < \Lambda_0$. We have also seen some evidence of numerical breakdown at higher value of Λ. However, the time dependent behaviour is very complex at such values and this is probably the source of difficulties rather than any proximity to a Taylor state.

5.2.7 Effect of the Roberts Number

When exploring values of $q << 1$ we found none of the numerical problems suggested by Soward (1986) or Skinner & Soward (1990) which we mentioned in Chapter 1. However, this is likely to be because are not looking at low q in a Taylor state, only in an Ekman state. We found that results were attainable at values as low as $q = 10^{-5}$ with no difficulties other than having to perform more timesteps to resolve the shapes of the waves. We went no lower than this because $q = 10^{-5}$ is the geophysically realistic value based upon molecular diffusivities. Figures 46 to 49 show the time dependent behaviour and equilibrated solutions for $q = 10^{-1}$ and $q = 10^{-5}$. Note that these are for Ra just less than Ra_T (see Table 4). Compare with Figure 27 and we can see that there is no effect of decreasing q other than increasing wavelength and decreasing the amplitude of solution. The behaviour and solution shape is preserved.

q	Ra_c	Ra_T
1	133.82	134.90
0.1	135.90	137.36
10^{-2}	136.51	138.07
10^{-3}	136.58	138.14
10^{-4}	136.59	138.15
10^{-5}	136.59	138.15

Table 4 - Variation of Ra_c and Ra_T with q for $\Lambda = 1$, $m = 2$, $n = 3$, $s_{ib} = 0$ with insulating sidewall boundaries and axially directed gravity.

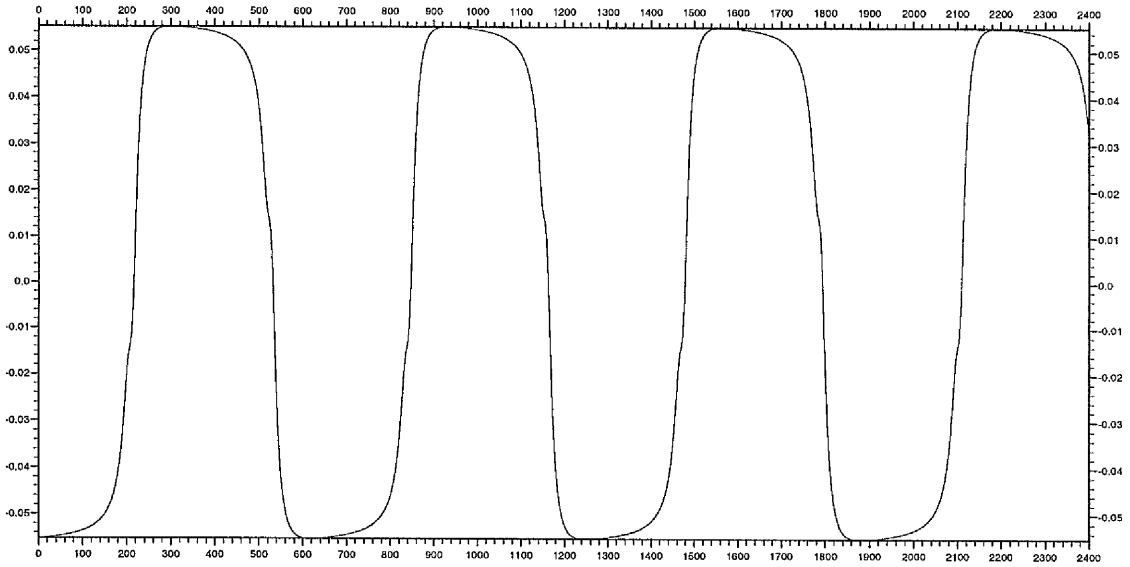

Figure 46 - As Figure 25 but for $Ra = 138.0$ and $q = 10^{-2}$.

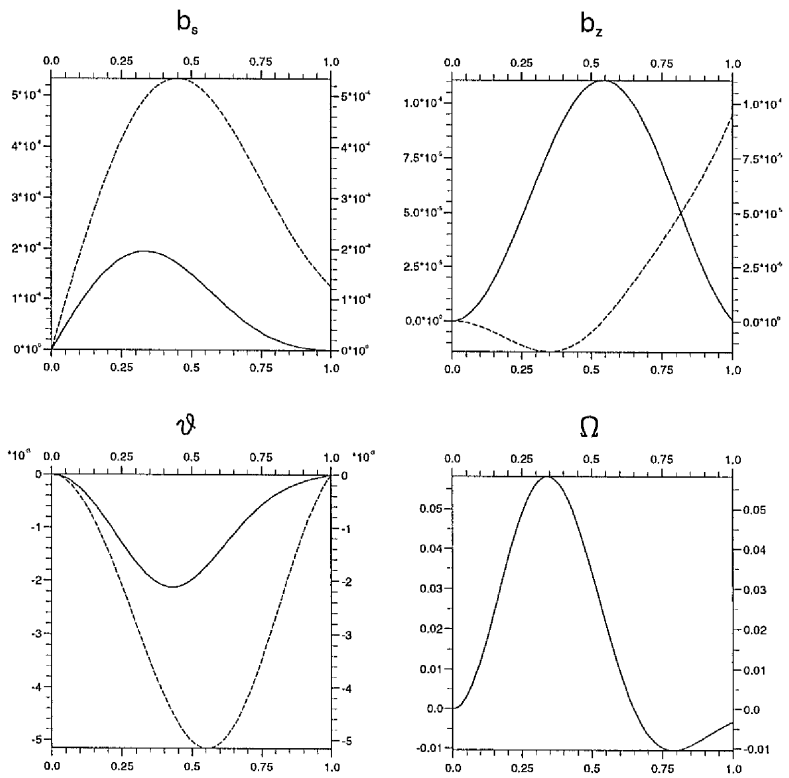

Figure 47 - As Figure 26 but for $Ra = 138.0$ and $q = 10^{-2}$.

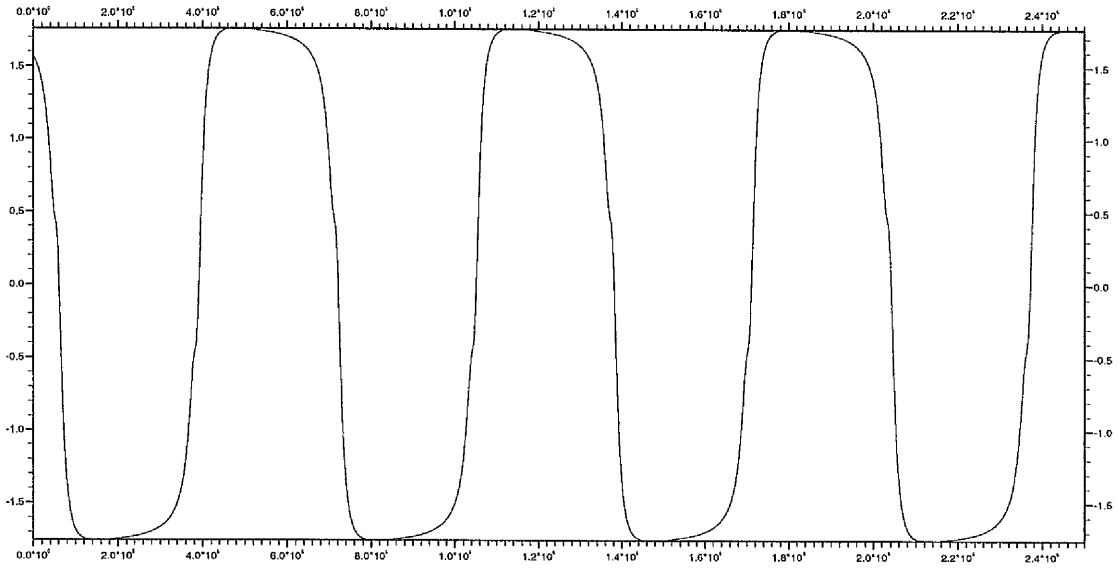

Figure 48 - As Figure 25 but for $Ra = 138.1$ and $q = 10^{-5}$.

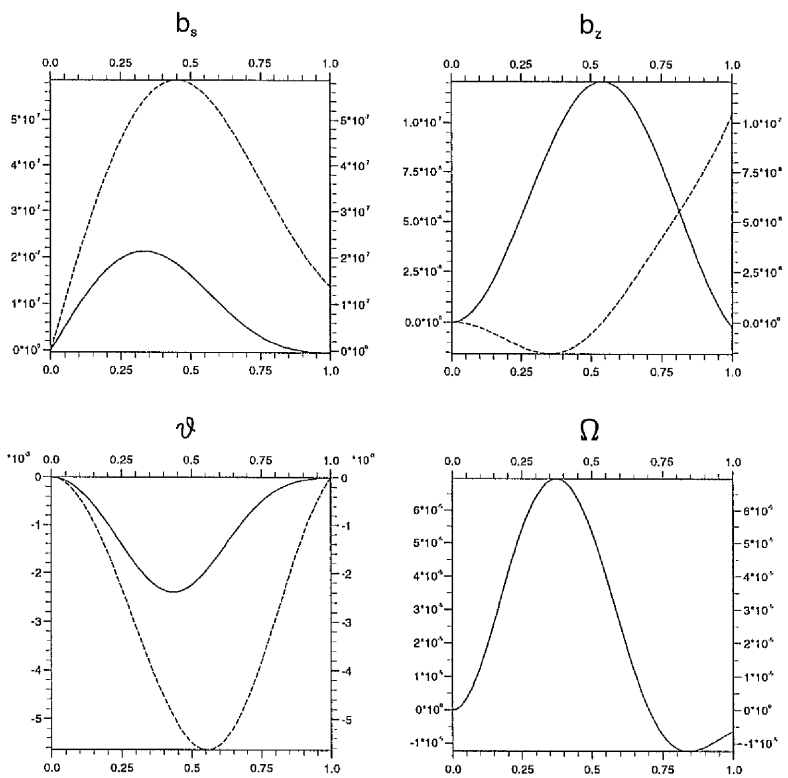

Figure 49 - As Figure 26 but for $Ra = 138.1$ and $q = 10^{-5}$.

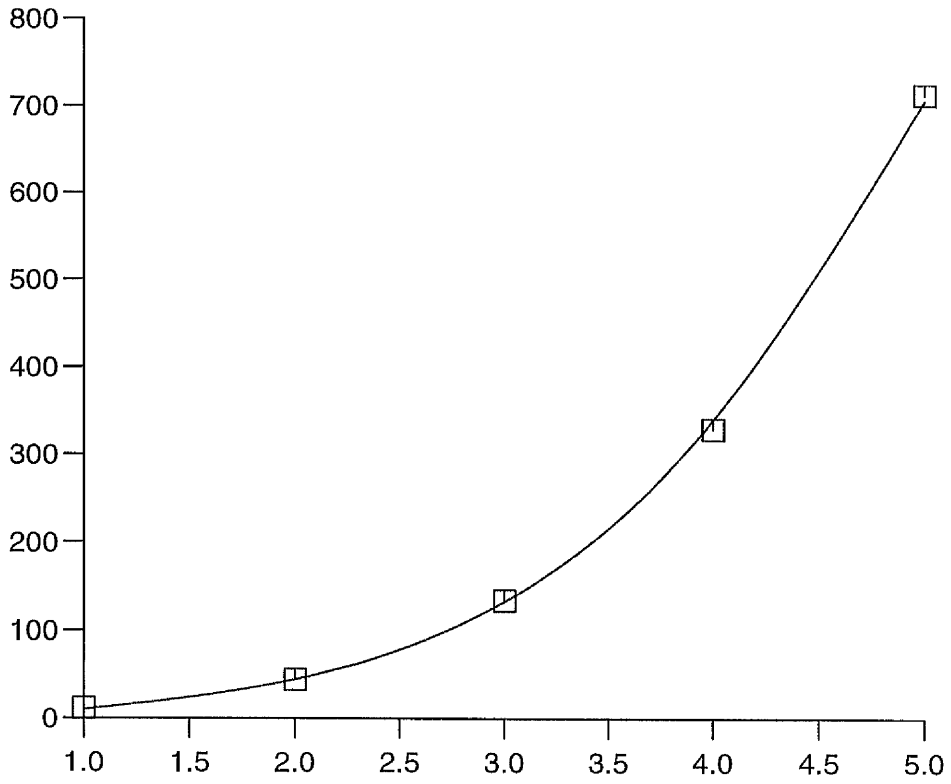

Figure 50 - Variation of Ra_c with n for $\Lambda = 1$, $m = 2$, $q = 1$, $s_{ib} = 0$, insulating sidewall boundaries and axially directed gravity.

5.2.8 Effect of the Axial Wavenumber

We have varied the axial wavenumber, taking values from 1 to 5. Figure 50 shows the effect of this variation on the critical Rayleigh number. We do not show Ra_T because for all values of n it is found to be so close to Ra_c.

n	Ra_c	Ra_T	$Ra_T - Ra_c$
1	11.781	11.745	−0.046
2	45.143	45.221	0.078
3	133.82	133.90	0.08
4	329.65	333.72	4.07
5	713.88	724.64	10.76

Table 5 - Variation of Ra_c and Ra_T with n for $\Lambda = 1$, $m = 2$, $q = 1$, $s_{ib} = 0$ with insulating sidewall boundaries and axially directed gravity.

Table 5 shows the exact values of Ra_c and Ra_T over this region. We can see that the effect of increasing n is to push Ra_T further above Ra_c and at $n = 1$, Ra_T is in fact below Ra_c. This suggests there is some non-integer value of n where $Ra_T = Ra_c$ By varying n we are effectively changing the aspect ratio of the cylinder. Therefore there exists some aspect ratio for which $Ra_T = Ra_c$.

5.3 Comparison with Previous Work

Of work that has been done before, the closest to ours is that of Skinner and Soward (1988, 1990) which we reviewed in Chapter 1. They look at a cylinder of fluid with axial gravity, electrically insulating outer boundary and no inner boundary. They non-dimensionalise using the cylinder length, which means we must transform the values of Ra, Λ and ω to make a comparison. The subscript O denotes our value, the S denotes the Skinner and Soward value.

$$Ra_O = \Delta^2 Ra_S \ , \quad \Lambda_O = \Delta^2 \Lambda_S \ , \quad \omega_O = q\Delta^2 \omega_S \ . \tag{5.17}$$

where $\Delta = 1.6$ is the non-dimensional radius of their cylinder i.e. the ratio of radius to height. We must choose $n_O = \Delta$ since they choose $n_S = 1$. All parameter values from now on in this section will be given in terms of Skinner and Soward's scalings. An exact comparison can be made between the respective linear results; they agree. However, this is not possible for the nonlinear results. Skinner and Soward are able to find a Taylor state whereas our solution breaks down as a Taylor state is approached. A precise comparison is therefore not possible. For example at $m = 1$, $q = 1$ and $\Lambda = 3$ they find $Ra_T = 7.49$ but we find $Ra_T = 7.62$ ($Ra_c = 7.43$). However, we need not regard this as a problem since there are some fundamental differences between the two analyses. We solve for Ekman states with a timestepping method but Skinner

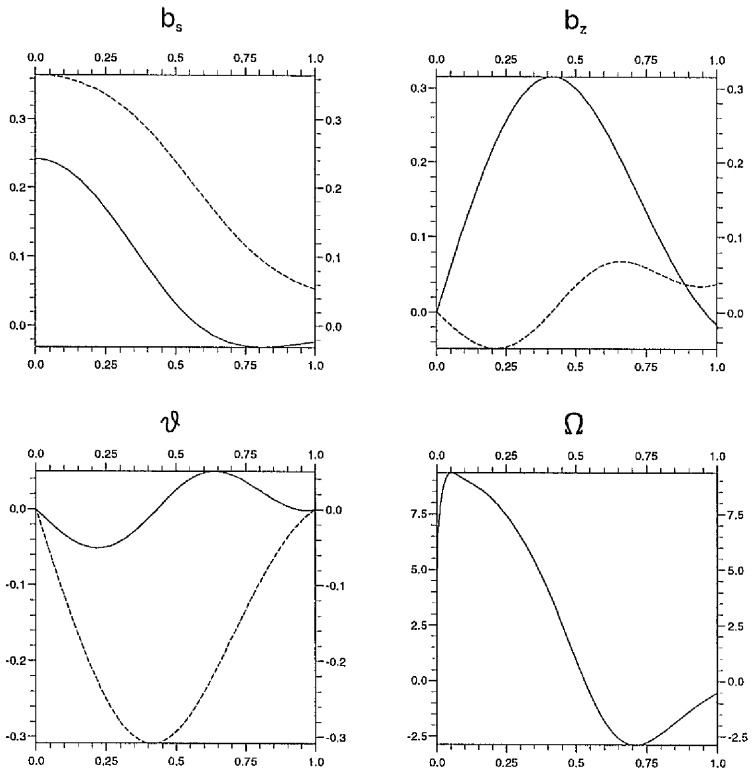

Figure 51 - Equilibrated solutions at $m = 1$, $q = 1$, $\Lambda = 3$ and $Ra = 7.62$ (Skinner and Soward scalings).

and Soward solve a nonlinear eigenvalue problem, finding Taylor states directly. We determine Ω explicitly through (1.14) where E is scaled out of the problem and is therefore finite. Skinner and Soward rely on the implicit modification of $\mathbf{b}$ by Ω in the magnetic induction equation to satisfy (1.4) and they set $E = 0$. Their alternative formulation makes a difference, in particular, in the limit $s \to 0$. They have

$$\Omega = \Omega_0 + \Omega_2 s^2 + \dots \,, \tag{5.18}$$

which implies a small axial boundary layer in which Ω increases rapidly from zero to Ω_0. The boundary conditions at $s = 0$ mean that $\Omega(0) = 0$ i.e. we have no boundary layer. When we compare our solutions, given in Figure 51, with those

in Figure 4 of Skinner and Soward (1990) we see that there are some similarities (taking into account differing normalisations) but that the geostrophic flow is quite different.

5.4 Conclusions

We have looked at the effect of the nonlinear geostrophic flow in the cylindrical geometry with various parameters and boundary conditions. We have seen good evidence of an approach to a Taylor state i.e. the cancellation in Ω such that $|\Omega|$ remains constant while the solution amplitude increases. Our major finding is that the orientation of gravity is very important in determining whether a Taylor state may exist. Our results suggest that axially directed gravity will always allow a Taylor state. For the radial gravity there is a certain range of Λ over which Taylor states cannot exist.

There is also a connection between the direction of gravity and the shape of the geostrophic flow. Radial gravity seems to enforce a form of Ω which has $G_\Omega > 0$ and axial gravity a form with $G_\Omega < 0$ i.e. one which can give rise to subcritical instability. It could be the case that there is a link between the shape of geostrophic flow and the existence of a Taylor state. This may warrant further investigation.

Variation of the parameters Λ, q ,s_{ib} and n or changing the sidewall boundary conditions only seems to affect the value of Ra_T relative to Ra_c. It is possible to find $Ra_T < Ra_c$ but this is depends on the parameters chosen and the initial perturbation given to the system.

An interesting feature worth noting is the behaviour of ω as a Taylor state is approached. In all cases we have investigated $Ra \to Ra_T$ as $\omega \to 0$. The numerical scheme breaks down so we cannot tell if this behaviour is truly associated

with a Taylor state.

Chapter 6

Discussion

We have looked at the effect of differential rotation ($\mathbf{U} = s\Omega\mathbf{1}_\phi$) on thermal and magnetic instability in a rapidly rotating, electrically conducting fluid system. We have examined various configurations including different geometries, boundary conditions, gravity direction and parameter values. Importantly, we have considered a number of fixed forms of Ω (linear problem) and a form dependent on magnetic field perturbation through Taylor's condition (nonlinear problem). The conclusions from the linear work (in Chapter 3) have a significant impact on the nonlinear work (Chapter 5). As we have seen, at $\Lambda = 1$, the forms of Ω which have $G_\Omega > 0$ can be associated with radial gravity systems and these do not exhibit Taylor states. On the other hand, forms of Ω with $G_\Omega < 0$ are associated with axial gravity systems and these do exhibit Taylor states. The stability dip in $G_\Omega < 0$ flows also has an effect on the ability to find subcritical Taylor states.

The work in this thesis has much scope for extension. For example, the inclusion of an inertial term in the modifed Taylor's constraint may improve numerical stability (see Jault 1995) and give oscillatory Taylor states. We have not investigated the effect of varying the azimuthal wavenumber, m. We would expect the variation of m to have a similar effect to varying the other parameters i.e. affecting the relative positions of Ra_T and Ra_c. However, $m = 1$ with $s_{ib} = 0$ may exhibit significantly different behaviour since alternative boundary conditions at $s = 0$ are used [see (5.13)]. Further investigation of how the value

of Λ affects the existence of Taylor states in the radial gravity system would be useful but may require more powerful numerical methods or computers. Finally the top and bottom boundaries of the cylinder could be changed to electrically insulating requiring multiple axial modes to be included in the calculations.

The motivation of this work is of course the real, spherical, geodynamo. The axial gravity case is equivalent to the polar region and the radial gravity case simulates the equatorial region. Obviously there will be some combination of the effects we have described but we cannot say which will dominate. It may be that the behaviour in the polar region is sufficient to allow Taylor states in the geodynamo. But we may expect not to find one if it is the lack of radial gravity effects that allow a Taylor state in the cylinder. Alternatively it may be the shape of the geostrophic flow which is important and the value of G_Ω will determine the existence of Taylor states.

References

Abdel-Aziz, M.M. & Jones, C.A. "$\alpha\omega$-dynamos and Taylor's Constraint," *Geophys. Astrophys. Fluid Dynam.* **44**, 117-139 (1988).

Abramowitz, M., & Stegun, I.A. *Handbook of Mathematical Functions*, Dover, New York (1965).

Acheson, D.J. "On the Hydromagnetic Stability of a Rotating Fluid Annulus," *J. Fluid Mech.* bf 52, 529-541 (1972).

Acheson, D.J. "Hydromagnetic Wavelike Instabilities in a Rapidly Rotating Stratified Fluid," *J. Fluid Mech.* **61**, 609-624 (1973).

Acheson, D.J. "Local Analysis of Thermal and Magnetic Instabilities in a Rapidly Rotating Fluid," *Geophys. Astrophys. Fluid Dynam.* **27**, 123-136 (1983).

Batchelor, G.K. *An Introduction to Fluid Dynamics*, CUP (1967).

Barenghi, C.F. "Nonlinear planetary dynamos in a rotating spherical shell: $\alpha^2\omega$-models and the geodynamo," *Geophys. Astrophys. Fluid Dynam.* **71**, 163-185 (1993).

Braginsky, S.I., "The Nonlinear Dynamo and Model-Z," in *Lectures on Solar and Planetary Dynamos* (ed. M.R.E. Proctor & A.D. Gilbert), CUP, 219-244 (1994).

Bullard, E.C. & Gellman, H., "Homogeneous Dynamos and Terrestrial Magnetism," *Phil. Trans. R. Soc. Lond. A* **247**, 213-278 (1954).

Cheney, W. & Kincaid, D. *Numerical Mathematics and Computing*, Brooks/Cole, California (1985).

Cowling, T.G. "The Magnetic Field of Sunspots," *Mon. Not. R. Astr. Soc.* **94**, 39-48 (1934).

Drew, S.J. "Thermal Convection in a Spherical Shell with a Variable Radius Ratio," *Geophys. Astrophys. Fluid Dynam.* **59**, 165-183 (1991).

Fearn, D.R. "Thermal and magnetic instabilities in a rapidly rotating fluid sphere," *Geophys. Astrophys. Fluid Dyn.* **14**, 103-126 (1979).

Fearn, D.R. "Boundary Conditions for a Rapidly Rotating Hydromagnetic System in a Cylindrical Container," *Geophys. Astrophys. Fluid Dynam.* **25**, 65-75 (1983a).

Fearn, D.R. "Hydromagnetic Waves in a Differentially Rotating Annulus. I. A Test of Local Stability Analysis," *Geophys. Astrophys. Fluid Dyn.* **27**, 137-162 (1983b).

Fearn, D.R. "Hydromagnetic Waves in a Differentially Rotating Annulus. II. A Test of Local Stability Analysis," *Geophys. Astrophys. Fluid Dyn.* **27**, 137-162 (1983b).

Fearn, D.R. "Hydromagnetic Waves in a Differentially Rotating Annulus. IV. Resistive Instabilities," *Geophys. Astrophys. Fluid Dyn.* **30**, 227-239 (1984).

Fearn, D.R. "Differential Rotation and Thermal Convection in a Rapidly Rotating System," *Geophys. Astrophys. Fluid Dyn.* **49**, 173-193 (1989a).

Fearn, D.R. "Compositional Convection and the Earth's Core," in *Geomagnetism and Palaeomagnetism* (ed. F.J. Lowes *et al.*), Kluwer Academic Publishers, 335-346 (1989b).

Fearn, D.R. "Eigensolutions of boundary value problems using inverse iteration," Journal of Compuational and Applied Mathematics **34**, 201-209 (1990).

Fearn, D.R. "Magnetic Instabilities in Rapidly Rotating Systems," in *Solar and Planetary Dynamos* (ed. M.R.E. Proctor, P.C. Matthews & A.M. Rucklidge), CUP, 59-68 (1993).

Fearn, D.R. "Nonlinear Planetary Dynamos," in *Lectures on Solar and Planetary Dynamos* (ed. M.R.E. Proctor & A.D. Gilbert), CUP, 219-244 (1994).

Fearn, D.R. "The Geodynamo," in *Earth's Deep Interior* (ed. D. Crossley), Gordon and Breach, 79-114 (1996).

Fearn, D.R. & Proctor, M.R.E. "Hydromagnetic waves in a differentially rotating sphere," *J. Fluid Mech.* **128**, 1-20 (1983a).

Fearn, D.R. & Proctor, M.R.E. "The stabilizing role of differential rotation on hydromagnetic waves," *J. Fluid Mech.* **128**, 21-36 (1983b).

Fearn, D.R. & Proctor, M.R.E. "Dynamically Consistent Magnetic Fields Produced by Differential Rotation," *J. Fluid Mech.* **178**, 521-534 (1987).

Fearn, D.R., Proctor, M.R.E. & Sellar, C.C. "Nonlinear Magnetoconvection in a Rapidly Rotating Sphere and Taylor's Constraint," *Geophys. Astrophys. Fluid Dyn.* **77**, 111-132 (1994).

Fearn, D.R., Roberts, P.H. & Soward, A.M. "Convection, Stability and the Dynamo," *Energy, Stability and Convection* (ed. G.P Galdi & B. Straughan), Longman Scientific and Technical, 60-324, (1988).

Fearn, D.R. & Weiglhofer, W.S. "Magnetic Instabilities in Rapidly Rotating Spherical Geometries. III. The Effect of Differential Rotation," *Geophys. Astrophys. Fluid Dyn.* **67**, 163-184 (1992).

Fearn, D.R., Lamb, C.J., McLean, D.R. & Ogden, R.R. "The Influence of Differential Rotation on Magnetic Instability, and Nonlinear Magnetic Instability in the Magnetostrophic Limit," *Geophys. Astrophys. Fluid Dyn.* Submitted.

Glatzmaier, G.A. & Roberts, P.H., "A three-dimensional self-consistent computer simulation of a geomagnetic field reversal," *Nature* **377**, 203-209 (1995a).

Glatzmaier, G.A. & Roberts, P.H., "A three-dimensional convective dynamo solution with rotating and finitely conducting inner core and mantle," *Phys. Earth Planet Inter.* **91**, 63-75 (1995b).

Hollerbach, R. & Ierley, G.R. "A modal α^2-dynamo in the limit of asymptotically small viscosity," *Geophys. Astrophys. Fluid Dyn.* **60**, 133-158 (1991).

Hutcheson, K.A. & Fearn, D.R., "The Nonlinear Evolution of Magentic Instabilities in a Rapidly Rotating Annulus," *J. Fluid Mech.* **291**, 343-368 (1995).

Hutcheson, K.A. & Gubbins, D., "Kinematic magnetic-field morphology at the core-mantle boundary," *Geophys. J. Int.* **116**, 304-320 (1994).

Jault, D., "Model Z By Computation and Taylor's Condition," *Geophys. Astrophys. Fluid Dyn.* **79**, 99-124 (1995).

Jones, C.A. "Dynamo Models and Taylor's Constraint," in *Advances in Solar System Magnetohydrodynamics* (ed. E.R. Priest & A.W. Hood), CUP, 25-50 (1991).

Jones, C.A. & Roberts, P.H. "Magnetoconvection in rapidly rotating Boussinesq and compressible fluids," *Geophys. Astrophys. Fluid Dyn.* **55**, 263-303 (1990).

Krause, F. & Rädler, K.-H. *Mean-Field Magnetohydrodynamics and Dynamo Theory*, Pergamon, Oxford (1980).

Kumar, S. & Roberts, P.H. "A three-dimensional kinematic dynamo," *Proc. R. Soc. Lond. A* **314**, 235-258 (1975).

Lorrain, P., Corson, D.P. & Lorrain, F. *Electromagnetic Fields and Waves*, W.H. Freeman and Co., New York (1988).

Malkus, W.V.R. & Proctor, M.R.E. "The macrodynamics of α-effect dynamos in rotating fluids," *J. Fluid Mech.* **67**, 417-443 (1975).

McFadden, P.L. & Merrill, R.T. "Inhibition and Geomagnetic Field Reversals," *J. Geophys. Res.* **98**, 6189-6199 (1993).

Ogden, R.R & Fearn, D.R. "The Destabilising Role of Differential Rotation," *Geophys. Astrophys. Fluid Dyn.* **81**, 215-232 (1995).

Proctor, M.R.E. "Numerical solution of the nonlinear α-effect dynamo equations," *J. Fluid Mech.* **80**, 769-784 (1977).

Roberts, P.H. "Kinematic Dynamo Models," *Phil. Trans. R. Soc. Lond. A* **272**, 663-703 (1972).

Roberts, P.H. "Fundamentals of Dynamo Theory," in *Lectures on Solar and Planetary Dynamos* (ed. M.R.E. Proctor & A.D. Gilbert), CUP, 1-58 (1994).

Roberts, P.H & Stewartson, K. "On Finite Amplitude Convection in a Rotating Magnetic System," *Phil. Trans. A* **277**, 287-315 (1974).

Roberts, P.H & Stewartson, K. "On Double-Roll Convection in a Rotating Magnetic System," *J. Fluid Mech.* **68**, 447-466 (1975).

Roberts, P.H. & Soward, A.M. "Dynamo Theory," *Annu. Rev. Fluid Mech.* **24**, 459-512 (1992).

Skinner, P.H. & Soward, A.M. "Convection in a Rotating Magnetic System and Taylor's Constraint," *Geophys. Astrophys. Fluid Dyn.* **44**, 91-116 (1988).

Skinner, P.H. & Soward, A.M. "Convection in a Rotating Magnetic System and Taylor's Constraint. Part II, Numerical Results," *Geophys. Astrophys. Fluid Dyn.* **60**, 335-356 (1990).

Song, X. and Richards, P.G. "Seismological Evidence for Differential Rotation of the Earth's Inner Core," *Nature* **382** 221-224 (1996).

Soward, A.M. "Non-Linear Marginal Convection in a Rotating Magnetic System," *Geophys. Astrophys. Fluid Dyn.* **35**, 329-371 (1986).

Soward, A.M. "The Earth's Dynamo," *Geophys. Astrophys. Fluid Dyn.* **62**, 191-209 (1991).

Soward, A.M. & Jones, C.A. "α^2-dynamos and Taylor's Constraint," *Geophys. Astrophys. Fluid Dyn.* **27**, 87-122 (1983).

Taylor, J.B. "The Magnetohydrodynamics of a Rotating Fluid and the Earth's Dynamo Problem," *Proc. R. Soc. Lond. A* **274**, 274-283 (1963).

Zhang, K. "Spherical Shell Rotating Convection in the Presence of Toroidal Magnetic Field," *Proc. R. Soc. Lond. A.* **448**, 245-268 (1995).

Appendix

Numerical Method

The linear problems given in Chapters 3 and 4 were solved with an inverse iteration eigenvalue code. The program to accomplish this was originally written by Prof. D.R. Fearn and modified by R.R. Ogden to incorporate a selection of alternative forms of prescribed differential rotation. We shall not detail the numerical method (see Fearn 1990). Here we shall describe the numerical method used to solve the non-linear problem given in Chapter 5. We shall illustrate the procedure with equations (5.5) but it is equally well applicable to equations (5.6). θ, b_s and b_z are complex functions of s and t so (5.5) is a system of 6 equations in 6 variables. We first render the equations in matrix form

$$\frac{\partial \mathbf{v}}{\partial t} = M\mathbf{v} - im\Omega\mathbf{v} \ , \tag{A.1}$$

where

$$\mathbf{v} = \begin{bmatrix} \Re(\theta) \\ \Im(\theta) \\ \Re(b_s) \\ \Im(b_s) \\ \Re(b_z) \\ \Im(b_z) \end{bmatrix} \tag{A.2}$$

and

$$M = \begin{bmatrix} qA_1 & 0 & A_2 & 0 & A_5 & 0 \\ 0 & qA_1 & 0 & A_2 & 0 & A_5 \\ A_4 & 0 & A_3 & -m\Lambda(1-sD) & 2n/s & -A_6 \\ 0 & A_4 & m\Lambda(1-sD) & A_3 & A_6 & 2n/s \\ 0 & 0 & 0 & -mA_2 & A_1 & -mA_5 \\ 0 & 0 & mA_2 & 0 & mA_5 & A_1 \end{bmatrix} \tag{A.3}$$

with

$$
\begin{aligned}
A_1 &= D^2 + s^{-1}D - m^2 s^{-2} - n^2 \,, \\
A_2 &= \Lambda n^{-1} s^{-1}(s^2 D^2 + 3sD - m^2 + 1) \,, \\
A_3 &= D^2 + 3s^{-1}D + s^{-2} - m^2 s^{-2} - n^2 \,, \\
A_4 &= -m^2 qRa/ns \,, \\
A_5 &= \Lambda(4 + sD) \,, \\
A_6 &= m\Lambda(m^2 + n^2 s^2)/ns \,.
\end{aligned}
\tag{A.4}
$$

We use a collocation method with N collocation points. This means we only solve the equations at discrete points s_j $(0 < j < N)$ in the interval $[s_{ib}, 1]$. At $s_0 = s_{ib}$ and $s_N = 1$ we apply boundary conditions. We shall use Chebyshev polynomials as our basis functions meaning that the components of $\mathbf{v}$ are expanded as (note that we use truncation N which, as we shall see, enables us to retain square matrices in the problem)

$$
v_i = \sum_{k=0}^{N} \alpha_{ik}(t) T_k(x) \,. \tag{A.5}
$$

$T_k(x)$ is a Chebyshev polynomial of degree k and $\alpha_{ik}(t)$ is a real function of time. A Chebyshev polynomial is a function of $x \in [-1, 1]$ so we map the interval $[s_{ib}, 1]$ to $[-1, 1]$ with the following change of variables

$$
x = -1 + 2(s - s_{ib})/(1 - s_{ib}) \,. \tag{A.6}
$$

We then define collocation points as follows

$$
x_j = \cos(j\pi/N) \,, \quad j = 0, \ldots, N \,. \tag{A.7}
$$

We will apply the operator D to the components of $\mathbf{v}$ so we need to know that

$$
Dv_i = 2/(1 - s_{ib}) \sum_{k=0}^{N} \alpha_{ik}(t) T_k'(x) \,, \tag{A.8}
$$

and

$$D^2 v_i = 4/(1 - s_{ib})^2 \sum_{k=0}^{N} \alpha_{ik}(t) T_k''(x) \ . \tag{A.9}$$

The values of the Chebyshev polynomials are calculated using the recurrence relation

$$T_k(x) = 2xT_{k-1}(x) - T_{k-2}(x) \ , \tag{A.10}$$

knowing that $T_0(x) = 1$ and $T_1(x) = x$. The derivatives can easily be calculated from $(A.10)$.

$$T_k'(x) = 2T_{k-1}(x) + 2xT_{k-1}'(x) - T_{k-2}'(x) \ , \tag{A.11}$$

and

$$T_k''(x) = 4T_{k-1}'(x) + 2xT_{k-1}''(x) - T_{k-2}''(x) \ . \tag{A.12}$$

To enable coding we convert $(A.1)$ to

$$\frac{d\mathbf{w}(t)}{dt} = P\mathbf{w}(t) - Q(t)\mathbf{w}(t) \ , \tag{A.13}$$

where P and Q are $6(N+1) \times 6(N+1)$ matrices and $\mathbf{w}$ (which replaces $\mathbf{v}$) is

$$\mathbf{w} = \begin{bmatrix} \beta_0 \\ \vdots \\ \beta_i \\ \vdots \\ \beta_{6N+5} \end{bmatrix} \tag{A.14}$$

where $\beta_{iN+k} = \alpha_{ik}$ for $0 \leq i \leq 5$ and $0 \leq k \leq N$. P is composed of 36 $(N+1) \times (N+1)$ blocks each corresponding to an entry in M. We illustrate by taking the first entry of M as an example. Collocation points correspond to the rows of the block so the 0^{th} and N^{th} rows correspond to the boundaries which we shall tackle later. For the j^{th} row (where $0 < j < N$) we will fill the block by applying the operator qA_1 to the correct component of $\mathbf{v}$ (i.e. v_0) and fixing

$x = x_j$. This gives us the following for the $(j,k)^{th}$ entry of the top left block of P

$$4/(1-s_{ib})^2 T_k''(x_j) + 2/(1-s_{ib}) T_k'(x_j) - m^2/s_j^2 + n^2 \ , \qquad (A.15)$$

where $s_j = s_{ib} + (x_j + 1)(1 - s_{ib})/2$. Equation $(A.9)$ is broken up in the following way

$$\left[\mathbf{w}(t+\Delta t) - \mathbf{w}(t)\right]/\Delta t = P\left[\mathbf{w}(t+\Delta t) + \mathbf{w}(t)\right]/2 - Q(t)\mathbf{w}(t) \qquad (A.16)$$

We have replaced the time derivative with $\left[\mathbf{w}(t+\Delta t) - \mathbf{w}(t)\right]/\Delta t$ assuming Δt is small and have averaged $P\mathbf{w}(t)$ and $P\mathbf{w}(t+\Delta t)$. This is normally done with diffusion operators only to make them numerically stable. Our matrix P includes all the diffusion operators and the averaging has been done on the whole of P for simplicity. This procedure, while non-standard, should not have a diverse effect on the results. $(A.16)$ may be rearranged as

$$\left[I - \frac{\Delta t}{2} P\right] \mathbf{w}(t+\Delta t) = \left[I + \frac{\Delta t}{2} P - \Delta t Q(t)\right] \mathbf{w}(t) \ , \qquad (A.17)$$

where I is the identity matrix, which gives us an equation describing the state at time $t + \Delta t$ in terms of the state at time t. It is at this point we fill in the boundary conditions. Rows 0, $N+1$, $2(N+1)$, $3(N+1)$, $4(N+1)$ and $5(N+1)$ are filled with boundary conditions for the inner boundary and rows N, $2N+1$, $3N+2$, $4N+3$, $5N+4$ and $6N+5$ are filled with those for the outer boundary. The required boundary conditions from (5.7)-(5.14) can be expressed in the form

$$\mathbf{c}.\mathbf{w} = 0 \qquad (A.18)$$

where row corresponding to that boundary condition is the vector $\mathbf{c}$. For example, the condition $\Re(\theta) = 0$ at $s = s_{ib}$ (from (5.14)) would be equivalent to

$$v_0 = \sum_{k=0}^{N} \alpha_{0k}(t) T_k(-1) = \sum_{k=0}^{N} \beta_k(t) T_k(-1) = 0 \ , \qquad (A.19)$$

which would correspond to

$$\mathbf{c} = \begin{bmatrix} T_0(-1) \\ \vdots \\ T_N(-1) \end{bmatrix} . \qquad (A.20)$$

The matrix $Q(t)$ is the following

$$Q(t) = \begin{bmatrix} R & 0 & 0 & 0 & 0 & 0 \\ 0 & -R & 0 & 0 & 0 & 0 \\ 0 & 0 & R & 0 & 0 & 0 \\ 0 & 0 & 0 & -R & 0 & 0 \\ 0 & 0 & 0 & 0 & R & 0 \\ 0 & 0 & 0 & 0 & 0 & -R \end{bmatrix} \qquad (A.21)$$

where the $(N+1) \times (N+1)$ sub-matrix R has entries

$$R_{jk} = mR_m\Omega(s_j)T_k(x_j)\Delta t \ , \quad 0 \leq j,k \leq N \ , \qquad (A.22)$$

and $\Omega(s_j)$ is calculated using expression (5.16). From this we can construct a timestepping computer program based around equation $(A.17)$. Before timestepping begins we pre-calculate the matrices $(I - \frac{\Delta t}{2}P)$ and $(I + \frac{\Delta t}{2}P)$ and perform an LU-decomposition on $(I - \frac{\Delta t}{2}P)$. During the timestepping process we can then solve for $\mathbf{w}(t + \Delta t)$ with the minimum of calculation; only $Q(t)$ needs to be worked out for each iteration.

GLASGOW UNIVERSITY LIBRARY